

https://dspace.org/

Investigation of the hydrogen spillover effect in platinum promoted cobalt/hollow carbon spheres

Masilo, Joy

2019
https://hdl.handle.net/10539/28873

Downloaded from a DSpace repository. https://dspace.org/

Investigation of the hydrogen spillover effect in platinum promoted cobalt/hollow carbon spheres

By:

Joy Masilo

Student number: 709195

A dissertation submitted to the Faculty of Science, University of the Witwatersrand, Johannesburg, in fulfilment of the requirements for the degree of Master of Science in Chemistry.

Supervisor: Prof. Neil Coville

Co-supervisor: Dr Roy Forbes

University of the Witwatersrand, Johannesburg. May 2019.

DECLARATION

I declare that this dissertation is my own, unaided work. It is being submitted for the Degree of Master of Science at the University of the Witwatersrand, Johannesburg. It has not been submitted before for any degree or examination at any other University.



WITS
UNIVERSITY



Joy Masilo

On this 28th day of May 2019 in Johannesburg.

ABSTRACT

The hydrogen spillover effect, as a mechanism to explain the promotion effect of noble metals on supported Co Fischer-Tropsch catalysts, has garnered increasing research attention. This is due to the enhanced Co reducibility and activity in Fischer-Tropsch catalysis when noble metals are incorporated. In this project, Pt was used as the noble metal promoter and hollow carbon spheres (HCSs) were used as a support for the encapsulation of the Co catalyst.

A hard-templating approach was used for the synthesis of the HCSs. We explored polystyrene spheres as the template and resorcinol-formaldehyde (RF) as the carbon precursor. Monodisperse polystyrene spheres were synthesized, followed by the addition of RF on the polystyrene spheres. The resulting composite was carbonized at 600 °C and it was during the carbonization of RF that template-removal also occurred. This was because the polystyrene spheres decompose at ~400 °C therefore the extra step of template removal after carbonization was eliminated. The HCSs had a BET surface area of 416 m^2/g, pore volume of 0.39 cm^3/g, and pore size of 3.8 nm.

The HCSs shell thickness was tuned by varying the amount of RF used and changing the alcohol used in the synthesis procedure. HCSs with shell thickness sizes in the range of 30 – 80 nm were confirmed using TEM. In addition, Co was encapsulated in the HCSs using the hard-templating method similar to the method employed in the synthesis of the HCSs. After template-removal and carbonization, Co@HCS and CoPt@HCS catalysts were obtained with nanoparticles that were well-dispersed. In addition, the shell (~30 nm) of the HCSs was used to separate the Co and Pt nanoparticles by encapsulating the Co nanoparticles and loading the Pt nanoparticles outside the HCSs to form the Co@HCS@Pt catalyst. The targeted percentage loading of Co was 10% and that of Pt was 0.5%.

The TPR profiles obtained for the catalysts showed that the presence of Pt indeed enhanced the Co reducibility, in both CoPt@HCS and Co@HCS@Pt catalysts. Evidence of this was seen in the downward shift in the peaks related to Co_3O_4 to Co^0 reduction, *via* the CoO intermediate, to lower temperatures. Primary hydrogen spillover, invoked when Co oxide and Pt are in intimate contact (CoPt@HCS), was more favourable in enhancing the reduction of Co oxide to the catalytically active Co phase, Co (hcp), and this was observed in the *in-situ* XRD data obtained, as it was the dominant phase at 350 °C. The enhancement can be

attributed to the dissociation of hydrogen on Pt and its subsequent spillover to Co oxide occurring more readily due to the intimate contact between Pt and Co in the catalyst. Further, the Co reducibility in Co@HCS@Pt, where secondary hydrogen spillover was invoked due to the separation between Co and Pt, was less pronounced, and the catalytically active Co (hcp) phase was formed in lower amounts. The separation between Pt and Co resulted in a diminished spillover effect.

Preliminary FT studies were undertaken which will be investigated further. The effect of hydrogen spillover was observed in the FT performance of the catalysts. After catalyst activation at 350 °C, the CoPt@HCS catalyst, due to a primary hydrogen spillover, showed the highest CO conversion rate which may be ascribed to the type of Co phase formed during catalyst activation. *In-situ* XRD confirmed that the dominant Co phase was the Co (hcp) phase which is highly catalytically active in the FT reaction. The effect of hydrogen spillover in Co@HCS@Pt was diminished, also in the FT reaction, due to the lack of synergism between Pt and Co, as a result of the distance between them. In addition, the presence of CO in the FT reaction may be detrimental to H_2 dissociation on Pt, leading to a diminished adsorption of hydrogen and its subsequent spillover. This effect of CO is more pronounced when Pt and Co are separated in comparison to when they are in intimate contact. Evidence of hydrogen spillover was also observed in the selectivities of the catalysts when compared at similar levels of CO conversions which moved towards hydrogenated products.

DEDICATION

This dissertation is dedicated to my father Lucas Masilo, my mother Martha Masilo, and my little brother Mpho Masilo, whom I deeply cherish.

ACKNOWLEDGEMENTS

I would like to express my heartfelt gratitude to my supervisor Prof Neil Coville for giving me the opportunity to pursue my MSc studies under his supervision. Your support and guidance is invaluable to me and has been instrumental in unlocking my potential to become a well-rounded researcher.

I would also like to express my appreciation to my co-supervisor Dr Roy Forbes for his support and invaluable insights regarding *in-situ* XRD.

I am indebted to Dr David O. Kumi, Dr Tumelo Phaahlamohlaka, Dr William Dlamini, Dr Lerato Hlekelele, Dr Bridget Mutuma, and Dr Prakash Gangatharan for their patience as they helped me find my way around the lab and for imparting their knowledge with me, with so much humility. I appreciate your contribution to the completion of this research project.

Special thanks go to the Microscopy and Microanalysis Unit for giving me access to their instruments and equipping me with the invaluable skills of operating electron microscopes.

I would like to extend my warmest gratitude to my CATMAT group members for all the smiles you put on my face, for the hearty shared laughter and for your constructive criticism during my presentations. Special mention goes to Thuli Buthelezi for our covalent bond.

I am very grateful to Sasol for the funding. No words can describe the feeling I felt when I was awarded the prestigious Sasol Postgraduate bursary. You have made pursuing my studies so much easier, with no financial stress. I would also like to thank the University of the Witwatersrand for awarding me the Postgraduate Merit Award.

Dr David O. Kumi, I consider myself so blessed to have met you. Each day with you has truly been a God-given gift. Your love, support, patience, guidance, and companionship, I cherish with all my heart. Thank you for being my ‘editor’, pillar of strength and prayer warrior.

To my dearest family; Papa, Mama, and Mpho, thank you for consistently checking up on me, encouraging me and believing in me more than I believe in myself, which has been pivotal in the completion of my studies. I love you so much.

To my Lord and Saviour, Jesus Christ, I bow before Your throne in worship. I give You all the Glory and Praise! Thank You Jesus!

PRESENTATIONS

Joy Masilo, Roy Forbes, Neil Coville. Synthesis of platinum-promoted cobalt on hollow carbon spheres for possible hydrogen spillover investigation (**Poster presentation**). CATSA conference. Pilanesburg, November 2017.

Joy Masilo, Roy Forbes, Neil Coville. Investigation of the hydrogen spillover effect using Pt promoted Co-hollow carbon spheres. (**Poster presentation**). CATSA conference. Polokwane, November 2018.

Joy Masilo, Roy Forbes, Neil Coville. Investigation of the hydrogen spillover effect using Pt promoted Co-hollow carbon spheres. (**Poster presentation**). SANi-NYRS symposium. Johannesburg, November 2018.

Joy Masilo, Roy Forbes, Neil Coville. Hydrogen spillover studies of hollow carbon spheres supported Pt and Co nanoparticles: microscopic analysis. (**2nd Best poster prize**). Microscopy in material science 2018 workshop. University of the Witwatersrand, Johannesburg, December 2018.

TABLE OF CONTENTS

DECLARATION i
ABSTRACT ii
DEDICATION iv
ACKNOWLEDGEMENTS v
PRESENTATIONS vi
LIST OF FIGURES x
LIST OF TABLES xiii
LIST OF ABBREVIATIONS xiv

Chapter 1: Introduction to the study and hypothesis 1
1.1. Introduction 1
1.1.1. Hollow carbon spheres 1
1.1.2. HCSs as a catalyst support in Fischer-Tropsch synthesis 2
1.1.3. Promotion of FT catalysts 3
1.1.4. Hydrogen spillover effect 3
1.2. Aim 4
1.3. Objectives 4
1.4. Problem statement 4
1.5. Outline of dissertation 5
1.6. References 6

Chapter 2: Literature Review 11
2.1. Fischer-Tropsch process background 11
2.1.1. FT mechanisms 14
2.1.2. Co FT Catalysts 15
2.1.3. Supports for Co FT catalysts 15
2.1.4. Incorporation of a promoter 16
2.2. Hydrogen spillover effect 19
2.2.1. Hydrogen spillover on carbon supports 22
2.2.2. Hydrogen spillover in heterogeneous catalysis 23

2.3. Hollow carbon spheres 26
2.3.1. HCS synthesis using the hard-templating method 26
2.3.2. HCS synthesis using the soft-templating method 33
2.3.3. Hollow carbon spheres applications 34
2.4. Conclusion 36
2.5. References 37

Chapter 3: Material Synthesis and Characterization Techniques 46
3.1. Chemicals and gases 46
3.1.1. Synthesis of Polystyrene Spheres (PSs) 46
3.1.2. Loading of Co or CoPt on PS (Co/PS or CoPt/PS) 46
3.1.3. Synthesis of Co or CoPt nanoparticles in HCSs (Co@HCS or CoPt@HCS) 47
3.1.4. Loading of Pt on Co@HCS (Co@HCS@Pt) 47
3.2. Material characterization 48
3.2.1. Scanning electron microscopy (SEM) 48
3.2.2. Transmission electron microscopy (TEM) 49
3.2.3. Nitrogen Physisorption and BET Method 50
3.2.4. Powder X-ray Diffraction (PXRD) 51
3.2.5. Thermogravimetric Analysis (TGA) 53
3.2.6. Raman Spectroscopy 54
3.2.7. Temperature-programmed reduction (TPR) 54
3.3. Catalyst evaluation (Fischer-Tropsch process) 55
3.3.1. Gases 55
3.3.2. FT rig and catalytic reactor setup 56
3.3.3. Experimental setup 56
3.3.4. Calibration of the gas chromatographs and product analysis 57
3.3.5. Data Analysis: Mass balance calculations 60
3.4. References 61

Chapter 4: Synthesis of hollow carbon spheres and the use of their void space for encapsulation of metal nanoparticles 63
4.1. Introduction 63
4.2. Experimental section 67
4.2.1. Sources of chemicals and gases 67

4.2.2. Synthesis of template (polystyrene spheres) 67
4.2.3. Synthesis of HCSs 67
4.2.4. Synthesis of HCSs with different shell thicknesses 68
4.2.5. Synthesis of Co@HCS 69
4.2.6. Results and discussion 70
4.3. Conclusion 84
4.4 References 85

Chapter 5: Hydrogen spillover studies and the effect of spillover on the FT process 91
5.1 Introduction 91
5.2. Experimental 94
5.2.1. Sources of chemicals and gases 94
5.2.2. Polystyrene spheres (PSs) – template synthesis 94
5.2.3. Loading of Co or CoPt on PSs 94
5.2.4. Synthesis of Co and CoPt inside HCSs (Co@HCS and CoPt@HCS) 95
5.2.5. Loading of Pt outside Co@HCS (Co@HCS@Pt) 95
5.3. Results and discussion 96
5.3.1. Catalyst characterization 96
5.3.2. Reducibility of the catalysts 101
5.3.3. Preliminary Fischer-Tropsch (FT) evaluation of the catalysts 105
5.4. Conclusion 107
5.5. References 108

Chapter 6: General conclusions and recommendations 113
6.1. Conclusions 113
6.2. Recommendations 114

LIST OF FIGURES

Chapter 2

Figure 2.1: ASF model for FT product distribution [2]. 13
Figure 2.2: TPR profiles of monometallic Co/Al_2O_3 and Pt-promoted $CoPt/Al_2O_3$ [22, 28]. . 18
Figure 2.3: Schematic representation of spillover (a) when the activator surface is in direct contact with the accepting surface and (b) when the activator surface is separated by some distance from the accepting surface [38]. 20
Figure 2.4: Bucket brigrade mechanism illustrating surface migration of hydrogen through formation of hydroxyl networks with the support [30]. 21
Figure 2.5: Hydrogen spillover mechanism on the aluminosilicate surface [40]. 22
Figure 2.6: Schematic representation of the hydrogen spillover effect [30] 24
Figure 2.7: TPR profiles of the catalysts supported on Al_2O_3 [30]. 25
Figure 2.8: Hard-templating synthesis of mesoporous HCS using mesoporous silica spheres [67]. 27
Figure 2.9: TEM images of N-HCSs obtained using silica spheres that are 1100 nm in size and different CVD times for (a) N-HCS900-1, (b) N-HCS900-2, (c) N-HCS900-3 and (d) N-HCS900-4 [76]. 28
Figure 2.10: a) Synthesis scheme of silica@RF sphere [79] and b) *in-situ* Stöber templating process for HCS synthesis [80]. 30
Figure 2.11: Synthesis procedure of HCPS carbon spheres [86]. 31
Figure 2.12: Synthesis of PNHCS using SPS as a template [87] 32
Figure 2.13: (a) SEM image of SPS template, (b) PNHCS obtained using SPS as a template (c – d) PNHCS at different magnifications [87]. 32
Figure 2.14: Formation of HCSs using trioctylamine droplets in an oil-in-water emulsion and a solution containing Cu–amine complexes and ascorbic acid, by hydrothermal treatment [88]. 33
Figure 2.15: Schematic illustration of the synthesis of (a) HCSs, (b) Pt@HCS and (c) PtCo@HCS [54]. 34

Chapter 3

Figure 3.1: A schematic representation of the synthesis of Co@HCS, CoPt@HCS and Co@HCS@Pt. 48
Figure 3.2: FEI Nova Nanolab 600 scanning electron microscope. 49
Figure 3.3: FEI Tecnai T12 transmission electron microscope. 50
Figure 3.4: Micromeritics Flow Prep 060 unit (left) and Micromeritics TriSta 3000 instrument (right). 51
Figure 3.5: Bruker D2 Phaser powder x-ray diffraction benchtop instrument. 52
Figure 3.6: Bruker D8 Advance diffractometer fitted with an XRK900. 53
Figure 3.7: PerkinElmer STA6000 analyser. 53
Figure 3.8: Bruker Senterra Raman spectrometer. 54
Figure 3.9: Micromeritics AutoChem II instrument. 55
Figure 3.10: Schematic representation of the (a) rig and (b) catalytic reactor. 56
Figure 3.11: TCD-GC trace of syngas. 57
Figure 3.12: FID-GC trace of the calibration gas (six gas mixture). 58

Chapter 4

Figure 4.1: The 3D networks formed from the hydrolysis of silica precursors and RF [22]...64
Figure 4.2: Addition reaction between resorcinol and formaldehyde [19]. 65
Figure 4.3: Condensation reaction to form a crosslinked structure [19]....65
Figure 4.4: Schematic illustration of the synthesis of the HCSs....68
Figure 4.5: a) SEM image b) TEM image and c) particle size distribution for PSs. 71
Figure 4.6: TG/DTG profile for PSs. 71
Figure 4.7: a) SEM image, b) TEM image and c) particle size distribution for HCSs. 74
Figure 4.8: TG curves of PSs and HCSs. 74
Figure 4.9: a) PXRD pattern, and b) Raman spectrum for the HCSs. 75
Figure 4.10: TEM images of (a) HCS-A, (b) HCS-B, and (c) HCS-C. 76
Figure 4.11: (a, b, c) Nitrogen adsorption-desorption isotherms and (d, e, f) pore size distribution graphs of HCS-A, HCS-B, and HCS-C. 77
Figure 4.12: TEM images of (a) HCS – ethanol, (b) HCS – isopropanol, and (c) HCS – 2-butanol....78

Figure 4.13: (a) Sintered Co nanoparticles in Co@HCS, (b) dispersed Co nanoparticles in Co@HCS. 79
Figure 4.14: Particle size distribution for (a) Sintered Co nanoparticles in Co@HCS, (b) dispersed Co nanoparticles in Co@HCS. 79
Figure 4.15: (a) PXRD pattern for Co@HCS and (b) TGA profiles of HCS and Co@HCS. .80
Figure 4.16: (a, b) TEM images at different magnifications, and (c) particle size distribution of Co@HCS-50. 81
Figure 4.17: (a) TEM image and (b) particle size distribution of Co@HCS-80. 82
Figure 4.18: TEM image and particle size distribution graph of (a, c) Co@HCS-EtOH, (b. d) Co@HCS-iPrOH, and (c, e) Co@HCS-2-BuOH, respectively. 83
Figure 4.19: TGA profiles of Co@HCS-EtOH, Co@HCS-iPrOH and Co@HCS-2-BuOH. .84

Chapter 5

Figure 5.1: Hydrogen spillover pathways: primary (left) and secondary (right), where; (a), molecular hydrogen; (b), dissociative adsorbtion onto the noble metal, Pt; (c), spillover of H atoms; (d), surface migration; (e) spillover; and (f) reduction and water removal. Adapted from [19]. 93
Figure 5.2: Schematic representation of the synthetic procedure for the metal-loaded HCSs.96
Figure 5.3: TEM images of (a) Co@HCS, (b) CoPt@HCS, (c) Co@HCS@Pt, and (d) Pt/HCS. 98
Figure 5.4: Particle size distribution of (a) Co@HCS, (b) CoPt@HCS, and (c) Pt/HCS.....99
Figure 5.5: (a) SEM image and (b) EDX spectrum of Co@HCS. 99
Figure 5.6: (a) SEM image and (b) EDX spectrum of CoPt@HCS. 100
Figure 5.7: TGA profiles for the catalysts. 100
Figure 5.8: TPR profiles of the catalysts. 103
Figure 5.9: Diffractograms of (a) Co@HCS, (b) CoPt@HCS , and (c) Co@HCS@Pt. 104
Figure 5.10: CO conversion of the catalysts. 106

LIST OF TABLES

Chapter 3

Table 3.1: A summary of the operating conditions used for the GC's. 59
Table 3.2: Equations used in product analysis. 60
Table 3.3: Descriptions of all the symbols used. 61

Chapter 4

Table 4.1: Synthesis parameters for HCSs with different shell thicknesses. 68
Table 4.2: A summary of the synthesis parameters used for the Co@HCS samples with different shell thicknesses. 70
Table 4.3: Shell thickness and textural properties of the HCSs with different shell thicknesses. 76
Table 4.4: Textural properties of the Co@HCS samples synthesized using different alcohols. 83

Chapter 5

Table 5.1: A summary of the nitrogen physisorption data. 101
Table 5.2: Summary of the FT performance of the catalysts. 106

LIST OF ABBREVIATIONS

Abbreviations	Definition
ASF	Anderson Schulz Flory
BET	Branauer Emmett Teller
CNFs	Carbon Nanofibers
CNTs	Carbon Nanotubes
CVD	Chemical Vapor Deposition
FID	Flame Ionization Detector
FTS	Fischer-Tropsch Synthesis
GC	Gas Chromatography
HCS	Hollow Carbon Spheres
PSs	Polystyrene Spheres
PXRD	Powder X-Ray Diffraction
RF	Resorcinol-Formaldehyde
SEM	Scanning Electron Microscopy
TCD	Thermal Conductivity Detector
TEM	Transmission Electron Microscopy
TGA	Thermo-Gravimetric Analysis
TPR	Temperature Programmed Reduction
WGS	Water Gas Shift

Chapter 1: Introduction to the study and hypothesis

1.1. Introduction

1.1.1. Hollow carbon spheres

The development of carbon materials with characteristics that are well defined, on a nano-scale, have stimulated great research interest [1-3]. It was, in particular, the discovery of novel carbon materials such as fullerenes in the 1980s that led to the studies of carbon nanotubes (CNTs) [4, 5] which resulted in major developments in the science of carbon. The discovery of CNTs was confirmed in 1991 by Ijima [6], and their structures were reported to consist of graphite-layered cylinders closed on both ends. They exist as either single- or multi-walled nanotubes whose diameters were found to be only a few nanometres in size and their lengths, between micrometres and millimetres [7, 8]. Their properties include their uniformity in pore size distribution and a meso/macro-pore structure, which made them attractive as catalyst supports [8, 9]. In addition to CNTs, carbon can take other shapes such as that found in carbon spheres (CSs) [1, 5, 10].

Furthermore, studies have been conducted to revisit the synthesis and properties of CSs which have been in existence for several decades, even before the synthesis of CNTs. The CSs' structure consists of graphitic flakes that are curled randomly and have a size between 1 – 10 nm and they share similar characteristics with CNTs owing to their carbon atoms with sp^2 hybridization [8, 11]. However, CSs are easier to prepare than CNTs and they have no metal impurities, and this has led to an explosive growth in their preparation and use. On the contrary, CSs have a low surface area, and this has led to the research and development of new synthesis methods resulting in a variety of solid, core/shell and hollow CSs with better physical and chemical properties [11].

Hollow carbon spheres (HCSs) in particular have garnered immense research interest owing to their unique properties such as; their hollow core resulting in their encapsulation ability, and their controllable surface properties [12, 13]. Their controllable surface properties include; controllability of their diameter, thickness, and porosity of the carbon shell [12]. These properties resulted in their use in a wide variety of applications such as adsorption,

energy storage and catalysis [14-19]. In the field of catalysis, HCSs are typically utilized as catalyst supports [20], and in this study, they used them as catalyst supports for Fischer-Tropsch synthesis (FTS).

1.1.2. HCSs as a catalyst support in Fischer-Tropsch synthesis

The great research interest in FTS, both industrially and in academia, was fuelled by the inflated price of crude oil, the impact petroleum exploitation has on the environment, and the stringent environmental regulations. FTS is a surface polymerization reaction in which a mixture of H_2 and CO (known as synthesis gas, abbreviated as syngas) derived from coal, natural gas or biomass, is converted into hydrocarbons, catalytically [8, 21, 22]. It is a clean alternative method to make fuels and chemicals [8, 23]. Franz Fischer and Hans Tropsch discovered the FT reaction using Co and Fe catalysts in the 1920s [24]. Since then, other metals were discovered that proved to exhibit FT activity such as Ru, Ni, and Os [21]. However, it was the Co and Fe FTS catalysts that gained popularity on an industrial scale, due to their affordability, activity and selectivity. Co is the FT catalyst of use in this study. Research methods to improve the activity of supported Co catalysts have shown that their FT performance depends on the choice of the support [25].

Conventionally, Co catalysts have been supported on Al_2O_3 or SiO_2 [8, 26-33]. Studies carried out on both supports have shown that metal – support interactions exist between the support and Co [8, 9, 34-36]. The presence of stronger interactions in Co/Al_2O_3 leads to the formation of $CoAl_2O_4$ which results in reduced Co reducibility. A weak interaction exists in Co/SiO_2 but it can still form Co_2SiO_4 which leads to reduced Co activity. Furthermore, the reduced interaction can lead to sintering of Co nanoparticles. Although some interactions should exist between the Co nanoparticles and the support in order to prevent sintering and attrition, it becomes a major challenge when either Co dispersion or Co reducibility is compromised [8]. High dispersion and high reducibility have been reported to be the two important parameters in determining the activity of a catalyst and are dependent on the type of support used [25, 37-39]. Therefore, research has been conducted on materials that will not compromise these parameters as the oxide supports do. As a result, carbon materials have been identified as a replacement owing to the unique properties of carbon such as the relative chemical inertness of carbon which leads to high reducibility of the cobalt oxide, and the carbon pore structure that can be controlled to achieve high Co dispersion [8, 9, 21, 34, 40, 41]. Hence, using carbon materials as a Co support, both high reducibility and high dispersion can be achieved. In addition, the intrinsic properties of the Co particles can be

studied using carbon materials as a support, without the properties of the support itself interfering, as would be the case if oxide supports were employed.

Several carbon supports have been used in FT studies and these include CNTs [9], CSs [11], carbon nanofibers (CNFs) [41], and HCSs. However, in this study HCSs were used as the Co FT catalyst support and their encapsulation ability was exploited by loading the Co nanoparticles inside the HCSs. In addition, a second metal, a noble metal in particular, Pt, was also added which could be separated from Co by the carbon shell. The effect of the promotion ability of Pt on Co and its overall FT performance was then evaluated.

1.1.3. Promotion of FT catalysts

Studies have been undertaken to investigate the effect of adding a noble metal promoter to the catalyst support and they have shown that the addition of a small amount of a promoter during the synthesis of a Co catalyst was found to considerably enhance the reducibility of Co, thus resulting in the enhancement of the catalyst performance [20, 25, 37, 39]. While several noble metals (Ru, Re, Ir, Pt, Pd) were observed to improve the reducibility of Co, it is Ru, Re and Pt (which is relevant to this study) that were observed to be the most efficient as Co reducibility promoters [42].

The promoters were reported as being able to enhance the catalytic performance of the Co catalysts by increasing the CO conversion [20, 42]. Furthermore, by varying the structure of the active site, promoters are able to improve the activity and selectivity of the catalyst. The metal promoter is assumed to be inert with respect to the FT reaction. Even if active (e.g. when Ru is used), only a small amount of the promoter is used and so the effect of the promoter on CO conversion will be small, as was observed by Phahlaamohlaka *et al.* [20]. Moreover, the metal promoter is used because it can be reduced at lower temperatures than cobalt oxide and is able to catalyse the cobalt oxide reduction by a hydrogen spillover effect. This is proposed to occur *via* the surface on which the promoter is deposited [42].

1.1.4. Hydrogen spillover effect

The hydrogen spillover effect is a phenomenon which involves the migration of hydrogen atoms from an activating species, usually a noble metal such as Pt, to an accepting species which could either be the support or a metal oxide [43]. In the case of hydrogen migrating to a metal oxide, reduction of the metal oxide occurs, and the noble metal is said to catalyse the reduction of the metal oxide [44-46]. Hydrogen spillover has been employed in two major

applications; hydrogen storage and catalysis. In the field of catalysis, FT in particular, it is employed as a mechanism to explain the catalysed reduction of metal oxides such as Co oxides whose active phase is the metallic phase and there is a need to achieve this at lower temperatures [47]. A wide variety of literature reports exists on this phenomenon. Four main types of systems can be envisaged and include; (i) the noble metal being supported on the metal oxide to be reduced mimicking a supported metal catalyst, (ii) the noble metal being physically mixed with the metal oxide, (iii) the noble metal is placed on a support such as Al_2O_3, and then physically mixed with the metal oxide and (iv) the noble metal and the metal oxide are separated by the support [43]. In this study the third and fourth of the systems have been studied, with HCSs used as a support, Pt as the promoter/activator and Co oxide as the acceptor.

1.2. Aim

To investigate the hydrogen spillover effect of the Co catalysts using HCSs as the support, and Pt as the promoter, and to also perform Fischer-Tropsch studies.

1.3. Objectives

- To synthesize size controlled HCSs using a polystyrene sphere template.
- To load Co and Pt metals on the HCSs.
- To characterize the materials using SEM, TEM, BET, TGA, Raman, PXRD, TPR, and *in-situ* PXRD.
- To study the hydrogen spillover effect on the Pt-promoted Co catalysts supported on HCSs.
- To evaluate the Fischer-Tropsch performance of the Pt-promoted Co catalysts.

1.4. Problem statement

The enhancement of the reducibility of cobalt has garnered great research interest because of its subsequent effect on the use of cobalt in Fischer-Tropsch (FT) synthesis [8]. The importance of cobalt reducibility emanates from the fact that in order to improve the catalytic activity (the rate at which a catalyst is able to transform reactants into products) of the cobalt FT catalyst, there needs to be an increased number of active cobalt metal sites that are stable under reaction conditions [20, 21, 25, 47, 48]. Since temperatures between 200 – 240 °C are typical reaction temperatures for the cobalt FT catalyst, to enhance the catalytic activity, a

high extent of the cobalt active species must be present at those temperatures [21]. Cobalt is most active in its metallic phase and cobalt FT catalysts require activation in a reducing atmosphere to form the desired metallic phase from the cobalt oxide phase [20, 47]. To enhance the reducibility of cobalt, a noble metal promoter can be introduced which is able to catalyze the reducibility of cobalt oxide by a mechanism called the hydrogen spillover effect [47]. This results in cobalt being reduced at lower temperatures, thereby increasing the amount of the cobalt active species available for the low temperature Co FT catalysis. As a result, its catalytic activity in FT is enhanced. The hydrogen spillover effect has been studied on conventional supports such as alumina or silica which are metal oxide supports having strong metal-support interaction with cobalt which hinder the reducibility of cobalt [20]. Therefore, there has been a growing need for supports that are chemically inert and will exhibit limited metal-support interactions, and carbon materials were found to possess that property. Furthermore, the properties of importance when using carbon as a support are; its hydrophobic character and the inertness of its graphitic surface [8]. Pevzner *et al.* studied the hydrogen spillover mechanism using carbon allotropes [49]. However, not much work has been done on the use of carbon materials as supports and the combined promotion effect of noble metals on cobalt FT catalysts [20]. Studies have been undertaken to investigate the effect of using; i) hollow carbon spheres as a support, ii) Co as a catalyst and iii) Ru as a promoter, both separately and when all three components have been combined, in FTS and hydrogen spillover reaction. However, the effect of Pt as a promoter in the above reaction has not been explored before. Furthermore, the effect of varying the distances of Pt relative to that of cobalt using the carbon shell has not been explored.

1.5. Outline of dissertation

Chapter 1: The chapter gives a brief introduction to the study and the associated aims, objectives, and hypothesis.

Chapter 2: The chapter gives a detailed literature review on the promotion of the cobalt Fischer-Tropsch catalyst using platinum *via* the hydrogen spillover mechanism, and the synthesis of hollow carbon spheres.

Chapter 3: The chapter provides a detailed description of the experimental procedures and characterization techniques involved in the synthesis and analysis of the supported catalysts.

Chapter 4: The chapter reports on the parametric studies undertaken in the synthesis of hollow carbon spheres and the use of hollow carbon spheres as a support for the cobalt catalyst by encapsulating cobalt nanoparticles inside the hollow carbon spheres.

Chapter 5: The chapter reports on the platinum promotion effect on the cobalt catalyst *via* the hydrogen spillover process and the subsequent effect of hydrogen spillover on cobalt Fischer-Tropsch catalysis.

Chapter 6: The chapter provides the overall conclusions of the study and futures recommendations.

1.6. References

[1] A.D. Roberts, X. Li, H. Zhang, Porous carbon spheres and monoliths: morphology control, pore size tuning and their applications as Li-ion battery anode materials, Chemical Society Reviews 43 (2014) 4341-4356.

[2] H. Nishihara, T. Kyotani, Templated nanocarbons for energy storage, Advanced Materials 24 (2012) 4473-4498.

[3] S. Nardecchia, D. Carriazo, M.L. Ferrer, M.C. Gutiérrez, F. del Monte, Three dimensional macroporous architectures and aerogels built of carbon nanotubes and/or graphene: synthesis and applications, Chemical Society Reviews 42 (2013) 794-830.

[4] H.W. Kroto, J.R. Heath, S.C. O'Brien, R.F. Curl, R.E. Smalley, C60: Buckminsterfullerene, Nature 318 (1985) 162.

[5] A.A. Deshmukh, S.D. Mhlanga, N.J. Coville, Carbon spheres, Materials Science and Engineering: R: Reports 70 (2010) 1-28.

[6] S. Iijima, Helical microtubules of graphitic carbon, Nature 354 (1991) 56.

[7] A.L. Dicks, The role of carbon in fuel cells, Journal of Power Sources 156 (2006) 128-141.

[8] T. Fu, Z. Li, Review of recent development in Co-based catalysts supported on carbon materials for Fischer–Tropsch synthesis, Chemical Engineering Science 135 (2015) 3-20.

[9] A. Tavasoli, R.M.M. Abbaslou, M. Trepanier, A.K. Dalai, Fischer–Tropsch synthesis over cobalt catalyst supported on carbon nanotubes in a slurry reactor, Applied Catalysis A: General 345 (2008) 134-142.

[10] D. Ugarte, Curling and closure of graphitic networks under electron-beam irradiation, Nature 359 (1992) 707.

[11] H. Xiong, M.A. Motchelaho, M. Moyo, L.L. Jewell, N.J. Coville, Correlating the preparation and performance of cobalt catalysts supported on carbon nanotubes and carbon spheres in the Fischer–Tropsch synthesis, Journal of catalysis 278 (2011) 26-40.

[12] S. Li, A. Pasc, V. Fierro, A. Celzard, Hollow carbon spheres, synthesis and applications–a review, Journal of Materials Chemistry A 4 (2016) 12686-12713.

[13] F. Su, X. Zhao, Y. Wang, L. Wang, J.Y. Lee, Hollow carbon spheres with a controllable shell structure, Journal of materials chemistry 16 (2006) 4413-4419.

[14] Z. Wen, Q. Wang, Q. Zhang, J. Li, Hollow carbon spheres with wide size distribution as anode catalyst support for direct methanol fuel cells, Electrochemistry Communications 9 (2007) 1867-1872.

[15] Y.-Y. Song, Y. Li, X.-H. Xia, One-step pyrolysis process to synthesize dispersed Pt/carbon hollow nanospheres catalysts for electrocatalysis, Electrochemistry Communications 9 (2007) 201-205.

[16] W.M. Zhang, J.S. Hu, Y.G. Guo, S.F. Zheng, L.S. Zhong, W.G. Song, L.J. Wan, Tin-nanoparticles encapsulated in elastic hollow carbon spheres for high-performance anode material in lithium-Ion batteries, Advanced Materials 20 (2008) 1160-1165.

[17] S. Ikeda, K. Tachi, Y.H. Ng, Y. Ikoma, T. Sakata, H. Mori, T. Harada, M. Matsumura, Selective adsorption of glucose-derived carbon precursor on amino-functionalized porous silica for fabrication of hollow carbon spheres with porous walls, Chemistry of materials 19 (2007) 4335-4340.

[18] F. Xu, Z. Tang, S. Huang, L. Chen, Y. Liang, W. Mai, H. Zhong, R. Fu, D. Wu, Facile synthesis of ultrahigh-surface-area hollow carbon nanospheres for enhanced adsorption and energy storage, Nature communications 6 (2015) 7221.

[19] H. Zhang, M. Yu, H. Song, O. Noonan, J. Zhang, Y. Yang, L. Zhou, C. Yu, Self-organized mesostructured hollow carbon nanoparticles *via* a surfactant-free sequential heterogeneous nucleation pathway, Chemistry of Materials 27 (2015) 6297-6304.

[20] T.N. Phaahlamohlaka, D.O. Kumi, M.W. Dlamini, R. Forbes, L.L. Jewell, D.G. Billing, N.J. Coville, Effects of Co and Ru Intimacy in Fischer–Tropsch Catalysts Using Hollow Carbon Sphere Supports: Assessment of the Hydrogen Spillover Processes, ACS Catalysis 7 (2017) 1568-1578.

[21] H. Jahangiri, J. Bennett, P. Mahjoubi, K. Wilson, S. Gu, A review of advanced catalyst development for Fischer–Tropsch synthesis of hydrocarbons from biomass derived syn-gas, Catalysis Science & Technology 4 (2014) 2210-2229.

[22] G.P. Van Der Laan, A.A.C.M. Beenackers, Kinetics and Selectivity of the Fischer–Tropsch Synthesis: A Literature Review, Catalysis Reviews 41 (1999) 255-318.

[23] Q. Cheng, Y. Tian, S. Lyu, N. Zhao, K. Ma, T. Ding, Z. Jiang, L. Wang, J. Zhang, L. Zheng, Confined small-sized cobalt catalysts stimulate carbon-chain growth reversely by modifying ASF law of Fischer–Tropsch synthesis, Nature communications 9 (2018) 3250.

[24] H. Mahmoudi, M. Mahmoudi, O. Doustdar, H. Jahangiri, A. Tsolakis, S. Gu, M. LechWyszynski, A review of Fischer Tropsch synthesis process, mechanism, surface chemistry and catalyst formulation, Biofuels Engineering 2 (2017) 11-31.

[25] G. Jacobs, T.K. Das, Y. Zhang, J. Li, G. Racoillet, B.H. Davis, Fischer–Tropsch synthesis: support, loading, and promoter effects on the reducibility of cobalt catalysts, Applied Catalysis A: General 233 (2002) 263-281.

[26] H. Xiong, Y. Zhang, S. Wang, J. Li, Fischer–Tropsch synthesis: the effect of Al2O3 porosity on the performance of Co/Al2O3 catalyst, Catalysis Communications 6 (2005) 512-516.

[27] H. Xiong, Y. Zhang, K. Liew, J. Li, Fischer–Tropsch synthesis: The role of pore size for Co/SBA-15 catalysts, Journal of Molecular Catalysis A: Chemical 295 (2008) 68-76.

[28] H. Xiong, Y. Zhang, K. Liew, J. Li, Ruthenium promotion of Co/SBA-15 catalysts with high cobalt loading for Fischer–Tropsch synthesis, Fuel Processing Technology 90 (2009) 237-246.

[29] J. Zhang, J. Chen, J. Ren, Y. Sun, Chemical treatment of γ-Al2O3 and its influence on the properties of Co-based catalysts for Fischer–Tropsch synthesis, Applied Catalysis A: General 243 (2003) 121-133.

[30] N. Fischer, E. van Steen, M. Claeys, Structure sensitivity of the Fischer–Tropsch activity and selectivity on alumina supported cobalt catalysts, Journal of Catalysis 299 (2013) 67-80.

[31] D.I. Enache, M. Roy-Auberger, R. Revel, Differences in the characteristics and catalytic properties of cobalt-based Fischer–Tropsch catalysts supported on zirconia and alumina, Applied Catalysis A: General 268 (2004) 51-60.

[32] G. Espinosa, J.M. Domínguez, P. Morales-Pacheco, A. Tobon, M. Aguilar, J. Benítez, Catalytic behavior of Co/(Nanoβ-Zeolite) bifunctional catalysts for Fischer–Tropsch reactions, Catalysis Today 166 (2011) 47-52.

[33] A. Dinse, M. Aigner, M. Ulbrich, G.R. Johnson, A.T. Bell, Effects of Mn promotion on the activity and selectivity of Co/SiO2 for Fischer–Tropsch Synthesis, Journal of Catalysis 288 (2012) 104-114.

[34] M. Trépanier, A. Tavasoli, A.K. Dalai, N. Abatzoglou, Co, Ru and K loadings effects on the activity and selectivity of carbon nanotubes supported cobalt catalyst in Fischer–Tropsch synthesis, Applied Catalysis A: General 353 (2009) 193-202.

[35] M. Trépanier, A. Tavasoli, A.K. Dalai, N. Abatzoglou, Fischer–Tropsch synthesis over carbon nanotubes supported cobalt catalysts in a fixed bed reactor: Influence of acid treatment, Fuel Processing Technology 90 (2009) 367-374.

[36] A. Tavasoli, K. Sadagiani, F. Khorashe, A.A. Seifkordi, A.A. Rohani, A. Nakhaeipour, Cobalt supported on carbon nanotubes — A promising novel Fischer–Tropsch synthesis catalyst, Fuel Processing Technology 89 (2008) 491-498.

[37] Z.-x. LI, Z.-q. NIE, L. WANG, X.-p. ZHANG, S.-j. ZHANG, Fischer–Tropsch Synthesis over Modified Cobalt Catalysts. 6 (2006).

[38] C.H. Bartholomew, Recent developments in Fischer-Tropsch catalysis, Studies in Surface Science and Catalysis, Elsevier, 1991, pp. 158-224.

[39] K. Okabe, X. Li, M. Wei, H. Arakawa, Fischer–Tropsch synthesis over Co–SiO2 catalysts prepared by the sol–gel method, Catalysis today 89 (2004) 431-438.

[40] M.C. Bahome, L.L. Jewell, K. Padayachy, D. Hildebrandt, D. Glasser, A.K. Datye, N.J. Coville, Fe-Ru small particle bimetallic catalysts supported on carbon nanotubes for use in Fischer–Tröpsch synthesis, Applied Catalysis A: General 328 (2007) 243-251.

[41] G.L. Bezemer, J.H. Bitter, H.P. Kuipers, H. Oosterbeek, J.E. Holewijn, X. Xu, F. Kapteijn, A.J. van Dillen, K.P. de Jong, Cobalt particle size effects in the Fischer−Tropsch reaction studied with carbon nanofiber supported catalysts, Journal of the American Chemical Society 128 (2006) 3956-3964.

[42] F. Diehl, A.Y. Khodakov, Promotion of cobalt Fischer-Tropsch catalysts with noble metals: a review, Oil & Gas Science and Technology-Revue de l'IFP 64 (2009) 11-24.

[43] G.C. Bond, J.B.P. Tripathi, Studies of hydrogen spillover. Part 3.—Catalysis of the reduction of metal oxides by palladium on silica, Journal of the Chemical Society, Faraday Transactions 1: Physical Chemistry in Condensed Phases 72 (1976) 933-941.

[44] G.C. Bond, P.A. Sermon, G. Webb, D.A. Buchanan, P.B. Wells, Hydrogenation over supported gold catalysts, Journal of the Chemical Society, Chemical Communications (1973) 444b-445.

[45] H. Charcosset, R. Frety, A. Soldat, Y. Trambouze, Increase of reducibility of NiO by H2, due to pretreatment with salt solutions, Journal of Catalysis 22 (1971) 204-212.

[46] N.I. Il'chenko, Catalytic oxidation of ammonia, Russian Chemical Reviews 45 (1976) 1119-1134.

[47] D. Nabaho, J.W. Niemantsverdriet, M. Claeys, E. van Steen, Hydrogen spillover in the Fischer–Tropsch synthesis: An analysis of platinum as a promoter for cobalt–alumina catalysts, Catalysis Today 261 (2016) 17-27.

[48] M. Minnermann, B. Neumann, V. Zielasek, M. Bäumer, Alumina-promoted cobalt and iron xerogels as catalyst for the Fischer–Tropsch synthesis, Catalysis Science & Technology 3 (2013) 3256-3267.

[49] S. Pevzner, I. Pri-Bar, I. Lutzky, E. Ben-Yehuda, E. Ruse, O. Regev, Carbon Allotropes Accelerate Hydrogenation *via* Spillover Mechanism, The Journal of Physical Chemistry C 118 (2014) 27164-27169.

Chapter 2: Literature Review

2.1. Fischer-Tropsch process background

The Fischer – Tropsch (FT) process involves the use of a catalyst for the conversion of syngas (carbon monoxide and hydrogen), from a feedstock such as coal, natural gas, and biomass, into various hydrocarbons [1-3]. Useful products such as diesel fuel, gasoline and waxes are produced through this process [4]. The FT process was developed by Franz Fischer and Hans Tropsch in the 1920s at the Kaiser Wilhelm Institute for Coal Research in Mülheim (Ruhr). It was Germany's source of fuel during World War II [1, 5]. By the 1940s, 600 000 tons of transportation fuel was produced from this process per year by means of the gasification of coal. In the 1950s South Africa adopted this process through the operations of Sasol plants to produce fuels and chemicals, due to the abundance of coal reserves in South Africa and to make the country less dependent on petroleum oil imports [6].

The FT process has garnered renewed interest over the years as an alternative to fuels produced from crude oil. The fuels are reported to be of a higher quality and have a very low content of sulphur, low CO and NO_x emissions, and a high cetane number [5]. These properties have made FT-produced fuels more attractive because a low sulphur content promotes less sulphur oxide emissions. The FT process can be shown as the production of hydrocarbon chains from the polymerization reaction equation (1). The water-gas-shift reaction (2) can also play a role in the FT reaction, especially when Fe is used as the FT catalyst.

$$CO + 2H_2 \longrightarrow -(-CH_2-)- + H_2O \qquad (1)$$

$$CO + H_2O \longleftrightarrow H_2 + CO_2 \qquad (2)$$

One of the main products produced from the FT process are alkanes (e.g. paraffins):

$$(2n + 1)\, H_2 + n CO \longrightarrow C_nH_{2n+2} + nH_2O \qquad (3)$$

The other primary products are alkenes (e.g. olefins):

$$2nH_2 + nCO \longrightarrow C_nH_{2n} + nH_2O \qquad (4)$$

Also oxygenates can be produced in the FT reaction:

$$n\mathrm{CO} + 2n\mathrm{H_2} \longrightarrow \mathrm{C}n\mathrm{H_{2n+2}O} + (n-1)\mathrm{H_2O} \qquad (5)$$

The FT reactions are highly exothermic. The weight of the hydrocarbons produced varies from low weight methane to heavy waxes and the products produced are dependent on the type of catalyst employed and the reaction conditions used. The proposed mechanisms of formation of these products, as reported in literature, are many. However, they have been summarized into three main mechanisms [2]. Generally, the steps involved in these mechanisms can be summarized as follows:

i. Adsorption of reactants
ii. Chain initiation
iii. Chain growth
iv. Chain termination
v. Desorption of products
vi. Readsorption and continuation of reaction

The second and fourth steps are usually described according to the statistical distribution model, the Anderson – Schulz – Flory (ASF) [1, 2]. This model is based on the assumption that the FT reaction is a polymerization reaction involving only one growth probability factor, α, that determines the hydrocarbon chain length distribution. This is given by:

$$m_n = (1-\alpha)\alpha^{n-1} \qquad (6)$$

where n – number of carbon atoms

m_n – mole fraction of chain length length *n*

α – chain growth propagation probability

1 – α – probability that the chain terminates

The α value is determined by the catalyst used for the FT process. Generally, group 8 – 10 metals show activity towards the FT process but only Co, Fe, and Ru exhibit enough activity towards CO hydrogenation to be used as FT catalysts [7]. Ru is not commercially used as an FT catalyst due to its limited availability which, consequently, made it exorbitantly priced. Ni can also be used to make hydrocarbons from syngas but is not commercially used because it is not highly active and it mostly produces methane. In addition, Ni tends to form volatile carbonyls (which are toxic) in the usually high pressures used in the FT reaction, and the

active phase of the catalyst is lost in the reactor. Therefore, Co and Fe are the metals commercially used as FT catalysts [8].

Fe catalysts are relatively cheap, which allows for the addition of the fresh catalyst to the fluidised-bed reactors on-line, resulting in longer runs and at higher rates of conversion. In addition, Fe catalysts require a low H_2:CO ratio. As a result, they exhibit a high WGS activity (see equation (2)) such that a lower amount of H_2 is required than shown in equation (1) and O_2 is removed through the emission of CO_2. However, due to stringent environmental regulations with regards to the greenhouse effect, the use of Fe may, in future, be problematic for the production of fuels [5]. Co catalysts, although more expensive than Fe catalysts, are generally preferred for the production of fuels because they mainly catalyse the production of long chain hydrocarbons such as waxes [5, 9]. In addition, Co catalysts are more stable against deactivation by H_2O (which is a by-product in the FT process) than Fe.

Figure 2.1 shows the product distributions proposed by equation (7) for different α values. Ni has the lowest α value and produces mainly CH_4. A fused Fe has α values in the range 0.65 – 0.70, whose optimum is in the gasoline region, while Co gives long hydrocarbons with α values in the range greater than 0.85 [1].

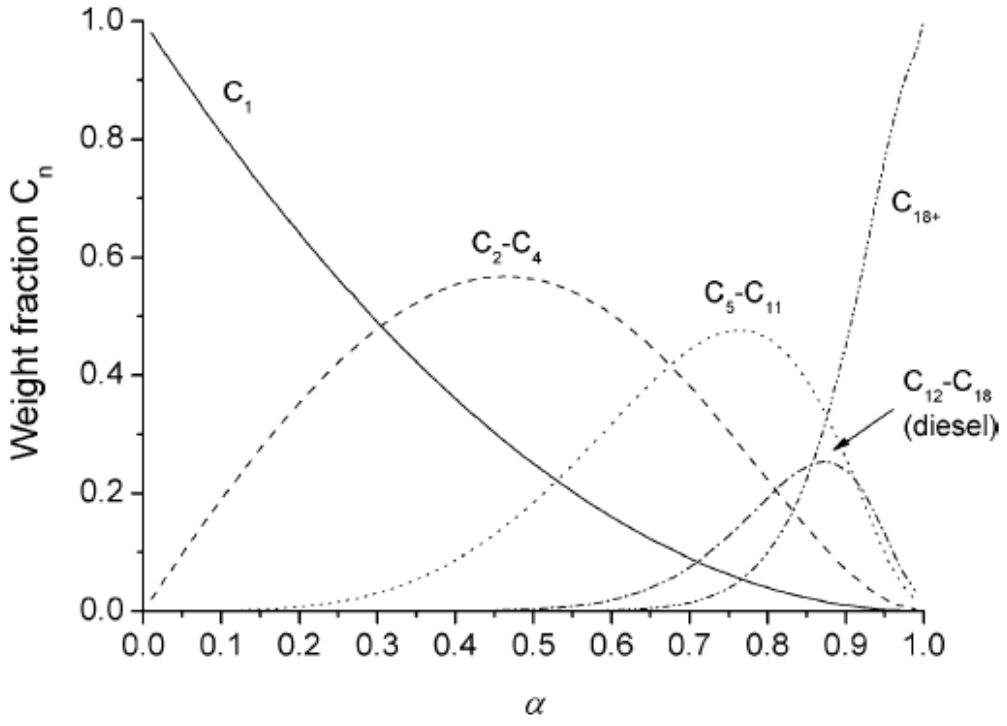


Figure 2.1: ASF model for FT product distribution [2].

2.1.1. FT mechanisms

FT is a polymerization reaction involving chain growth in a step-wise manner. What is unique about the FT polymerization reaction is the conversion of the feed first into the monomer and initiator, then the subsequent polymerization to the final products i.e. the hydrocarbons [10]. The proposed monomers for the FT reaction are [11]: methylene (CH_2) for the *carbide mechanism*, hydroxyl carbine (CHOH) for the *enol mechanism* and CO for the *CO insertion mechanism*. These mechanisms are discussed below:

1. The *carbide mechanism* [2, 10, 12, 13] is one of the oldest and widely accepted FT mechanisms. The monomer involved in this mechanism is CH_2 and it has been proposed that chain growth occurs by the insertion of this species. The dissociative adsorption of CO on the surface of the active phase forms a carbide, and when H_2 dissociatively adsorbs onto the surface the carbide is then reduced to the monomer, CH_2. Chain growth then occurs by the insertion of the CH_2 species in the growing chains. Termination occurs by either addition of hydrogen or CH_3 species to form a paraffin or abstraction of a hydrogen atom to form an olefin.

2. The *enol mechanism* was proposed in the 1950s [2, 12]. In this mechanism, CO adsorption is undissociative and the hydrogen atoms on the surface react with it to form the initiator, the enol group, CHOH. Chain growth occurs by the condensation of the enol groups and the elimination of water. Chain termination occurs by desorption of alkylhydroxycarbene, forming an aldehyde or by the elimination of water to form paraffins.

3. The *CO insertion mechanism* was first proposed in 1958 [2] and has undergone modification through the years. This mechanism involves chain growth by the insertion of CO into a metal – carbon bond. In the initiation step, the insertion of CO can occur into either a metal – H bond or a metal – carbon bond to produce an aldehyde species or an enol species, respectively. Chain growth results from the subsequent hydrogenation of these species. The resulting growing chains can then be hydrogenated to olefins leading to termination.

2.1.2. Co FT Catalysts

A large volume of literature has addressed the use of Ni, Fe, Co and Ru as FT catalysts. However, in the last two decades the Co catalyst has received considerable attention and vast numbers of peer-reviewed papers and patents have been published on improving its activity and selectivity [2, 5]. The performance of Co in the FT reaction is governed by many factors that include:

(i) The support (e.g. Al_2O_3, SiO_2, TiO_2 or carbon materials) on which the Co nanoparticles are dispersed.

(ii) Incorporation of a promoter:

- An oxide promoter such as metal oxides, of Mn, V, Ce, La, Zr, Cr.
- A noble metal promoter such as Ru, Pt, Pd, Re, Rh and Ir.

2.1.3. Supports for Co FT catalysts

The role of the support has been well documented [5, 14, 15]. It provides thermal and mechanical stability, and helps maintain the Co nanoparticles in a highly dispersed state. The choice of support has a huge influence on the Co active metal sites available after activation (i.e. after reducibility of Co oxide to metallic Co^0) [8]. The metallic Co^0 phase, whether it is predominantly face-centred cubic (fcc) Co or hexagonal closed-packed (hcp) Co depends on the temperature of activation used and the atmosphere, i.e. the composition of the gases used for activation. This also has an effect on the overall FT activity of the catalyst [16]. For instance, O'Shea *et al.* [17] observed an enhancement in the FT activity of Co/SiO_2 when the activation atmosphere consisted of a mixture of H_2 and CO (syngas) as opposed to the usual H_2 atmosphere used in Co catalyst activation. They attributed the enhancement to the formation of the highly dispersed hcp Co nanoparticles in the syngas atmosphere while the H_2 atmosphere led to the formation of active fcc Co. This observation was also confirmed by Ducreux *et al.* [18] who observed, after a series of catalytic tests, maintaining the same conditions, that a catalyst consisting of predominantly hcp Co is more catalytically active than fcc Co and that an increase in the amount of fcc Co in a catalyst proved to lower the catalytic activity.

The use of metal oxide supports introduces metal – support interactions, which are particularly strong when using Al_2O_3 or TiO_2 as the support for Co [14]. These strong metal-support interactions favour good dispersion of the Co nanoparticles on the support but hinder

their reducibility, consequently, resulting in fewer Co active sites. However, SiO_2 which exhibits weaker metal-support interactions results in greater Co reducibility but with poorer Co dispersion. This was observed by Jacobs *et al.*, who reported that the effect of the metal support interactions was in the order; $Al_2O_3 > TiO_2 > SiO_2$ [19]. However, to circumvent the issue of either reducibility or dispersion being compromised, which are both significant in the optimal performance of a catalyst in FT, a relatively inert support material may be used such as carbon. As a consequence of the relative inertness of carbon materials, the reducibility of the cobalt oxide may be enhanced because of the absence of hardly reducible compounds formed which inhibit the reducibility of the cobalt oxide. Meanwhile, the surface of carbon materials may be modified by controlling their pore structures or by surface functionalization, to improve the dispersion of the Co nanoparticles supported on them [14, 20]. In terms of the effect of the pore structure on the FT performance, Xie *et al.* [21] used CNTs with different pore sizes from (5 – 17 nm) as cobalt oxide catalyst supports. They observed that the 5 nm CNTs exhibited a high surface area while the cobalt oxide nanoparticles supported on them had a small average particle size (i.e. 4.2 nm). The average particle size of the cobalt oxide nanoparticles was observed to increase with an increase in the pore size of the CNTs. However, the FT activity improved with a decrease in the pore size of the CNTs because the 17 nm CNTs resulted in a faster deactivation of the supported cobalt catalyst.

2.1.4. Incorporation of a promoter

A promoter is a substance usually added in small quantities to catalysts to enhance their catalytic activity, stability and selectivity [1, 5, 15]. The promoter is usually added through co-impregnation or subsequent impregnation. There are two main types of promoters: *structural promoters* and *electronic promoters*. Structural promoters have an influence on the formation and stability of a catalyst, while *electronic promoters* directly affect the electronic structure and also modify the chemisorption properties of the catalyst.

2.1.4.1. Structural promotion effects

Structural promotion leads to increased catalyst activity and stability due to the enhancement in, for instance, Co dispersion which results in an increase in the number of Co metal active sites. Meanwhile, structural promotion has little direct influence on the selectivity of a catalyst because its role is mainly to increase the number of active sites of the catalyst. Furthermore, the increase in the number of active sites of the catalyst is also a result of the ability of the structural promoter to impede the formation of metal-support components. It is also able to prevent agglomeration and sintering of Co under FT reaction conditions [5].

Metal oxides such as La_2O_3, ZrO_2, CeO_2 and MnO have been employed for this function. Noble metals such as Pt, Ru and Re have been used to increase the dispersion of Co catalysts thereby increasing their active sites [22-24]. They have also been reported to improve the reducibility of the Co catalyst.

2.1.4.2. Electronic promotion effects

Electronic promotion effects are less easily detected than structural promotion effects. This promotion can be understood in terms of ligand effects. An electronic promoter is able to modify the surrounding (electronic) environment of a Co active site. This may occur by electron donation or withdrawal which may lead to a change in the product selectivity or an increase in the intrinsic turnover frequency. These ligand effects may also reduce the rate of deactivation of a Co catalyst by modifying adsorption/desorption properties of the reactants on the surface of the Co catalyst. Electronic promotion occurs by an intimate interaction between the promoter and the Co surface [5]. For example, the Co surface can be decorated by the promoter molecules but they must not block the Co active sites. In addition, electronic promoters may cause an increase in the resistance of a Co catalyst to re-oxidation and overall deactivation during an FT reaction.

2.1.4.3. Pt as a promoter of Co catalysts

Pt, like Ru and Re has received considerable research attention as a promoter for Co catalysts and it is of particular interest in this study. Its role as a structural promoter has been well documented and it is frequently reported to enhance the dispersion of supported Co catalysts and its reducibility [5]. The active phase of Pt as a promoter is its metallic phase and it therefore needs to undergo reduction prior to its use. For example, Zsoldos *et al.* [25] reported on the enhancement in the reducibility of Co/Al_2O_3 in the presence of a small amount of Pt. The hardly reducible cobalt aluminates are reduced as a result of the promotion effect of Pt in $Pt–Co/Al_2O_3$. Evidence of the formation of a bimetallic Pt – Co catalyst was found in the XPS data published in their studies [26]. The XPS data showed the catalysts with a high ratio of Pt/Co (atomic fraction of Co = 0.2 – 0.5) had $CoPt_3$ nanoparticles on the surface of the Co nanoparticles. This was also confirmed by Jacobs *et al.* [27] using EXFAS studies on $Co–Pt/Al_2O_3$ using the Pt L-edge from which they observed that Pt – Pt bonds were not formed and isolated Pt atoms formed bonds with Co atoms. Meanwhile, at the Co K-edge the Co cluster size was found to have slightly increased in the presence of Pt, Co reduction was significantly increased and aluminate formation was averted. Chu *et al.* [28] observed an enhanced reducibility of Co in the presence of Pt, in their $15\%Co–0.1\%Pt/Al_2O_3$

catalyst. They used the TPR data shown in (Figure 2.2) to reveal the extent of reducibility when comparing the Co/Al_2O_3 with $CoPt/Al_2O_3$.

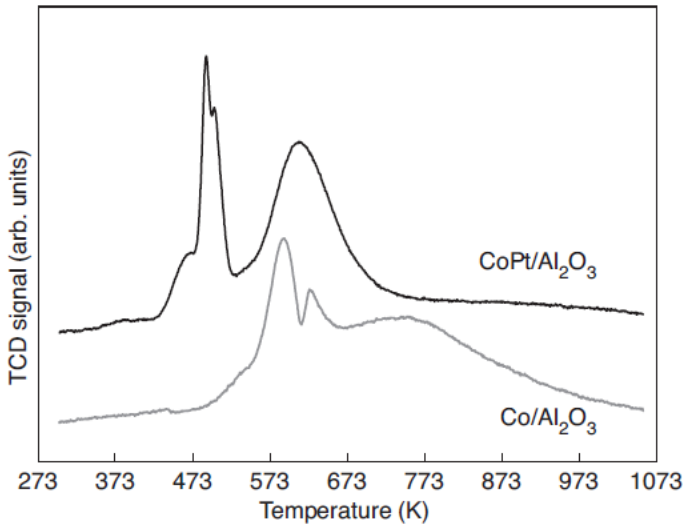


Figure 2.2: TPR profiles of monometallic Co/Al_2O_3 and Pt-promoted $CoPt/Al_2O_3$ [22, 28].

Cobalt in its oxide phased is predominantly found as Co_3O_4. Several reports suggest that the reduction of Co_3O_4 proceeds *via* the CoO intermediate to form the metallic Co^0 phase as follows [22]:

$$Co_3O_4 \longrightarrow CoO \longrightarrow Co^0$$

Figure 2.2 shows that Pt promotion enhanced both steps: $Co_3O_4 \longrightarrow CoO$ and $CoO \longrightarrow Co^0$ as is evident in the low-temperature shifts of the peaks corresponding to both cobalt oxide reduction steps. It has been reported that Pt is amongst the noble metal promoters that are able to enhance both reduction steps. The ease with which cobalt oxide reduction occurs in the presence of a noble metal can be attributed to the hydrogen spillover phenomenon [22]. It involves the noble metal facilitating reduction of a metal oxide through the dissociation of hydrogen on the surface of the noble metal and the subsequent spillover of hydrogen to the metal oxide. Davis *et al.* [29] like Zsoldos *et al.* [26] observed that Pt does not form Pt – Pt bonds when it is on the edge of the cobalt clusters. Therefore, it was suggested that reduction occurs due to the dissociative adsorption of hydrogen on Pt which then spills over to the cobalt oxide and nucleates the cobalt metal sites.

In addition to the enhancement of Co reducibility, Pt is able to enhance the rate of CO hydrogenation of a Co catalyst in the FT reaction. Chu et el. [28], showed that in addition to

the improvement in the Co reducibility due to the promotion by Pt, that a more than 8 times increase in the FT reaction rate and a decrease in the C_{5+} selectivity was observed. Pt, especially at loadings $\geq$ 0.1 % tends to have an effect on the Co catalyst selectivity. This may be due to the high hydrogenation activity of Pt. Co catalysts promoted using Pt tend to exhibit a smaller chain growth probability, higher methane selectivity and a lower C_{5+} selectivity than the monometallic Co catalyst. Nabaho *et al.* [30], observed, as a result of Pt promotion, an enhancement in the turnover frequency (TOF) and an enhanced selectivity towards CH_4 and paraffins for a Pt–Co/Al_2O_3 catalyst. Zhang *et al.* [31] studied the Pt promotion effect of Co supported on carbon nanotubes CNTs. They observed an increase in the CO conversion and cobalt time yield in the presence of Pt, which they found to be greater than when using Ru as a promoter. However, contrary to other reports, they observed a decrease in CH_4 selectivity instead of an increase, as well as an increase in C_{5+} selectivity.

2.2. Hydrogen spillover effect

Hydrogen spillover is a phenomenon that involves migration of hydrogen atoms from a surface on which they are generated or sorbed (activator surface), onto another surface (acceptor surface) that would not otherwise generate or sorb them under the same conditions [32-34]. It has been a research topic of importance according to Conner and Falconer [33], since the possibility of its existence was first discussed by Emmett [35] in 1940. This early study was related to the synthesis and decomposition of NH_3. It was not until almost two decades later that evidence for a spillover effect was reported. In 1957, Kuriacose observed a significant enhancement in the decomposition of GeH_4, generating H_2, in the presence of a Pt wire and Taylor attributed this to the recombination of H atoms to H_2 molecules on Pt [33]. Further experimental results were reported by Khoobiar *et al.* [36] in 1964 when they observed that WO_3 was reduced to WO_{3-x} in the presence of Pt. This observation was ascribed to the dissociative adsorption of H_2 molecules on Pt (activator) which produced H atoms that subsequently migrated to the WO_3 (acceptor) causing its reduction.

To further confirm the hydrogen spillover effect observed in Pt/WO_3, Triwahyono *et al.* [37] used Pt/MoO_3 to observe the kinetics of H_2 on MoO_3 in the presence and absence of Pt. They observed very minimal H_2 generation on just MoO_3 which demonstrated the difficulty of H_2 dissociation on MoO_3. In comparison, H_2 generation was approximately 200 times greater on Pt/MoO_3. This observation confirmed that there was indeed hydrogen spillover from the surface of Pt to that of WO_3.

The occurrence of hydrogen spillover involves several processes such as surface diffusion, reaction on or with the accepting surface, and creation of active sites in catalysis. This makes hydrogen spillover significant as a mechanistic step in heterogeneous catalysis. There are two types of spillover mechanisms that can be envisaged. One is where the activator is in direct contact with the acceptor, known as primary spillover and shown in (Figure 2.3 a) and the other one is where the acceptor is not directly adjacent to the activator, i.e. the activated species first spills over from the activator onto the support and then diffuses to another accepting surface, known as the secondary spillover, and shown in (Figure 2.3 b).

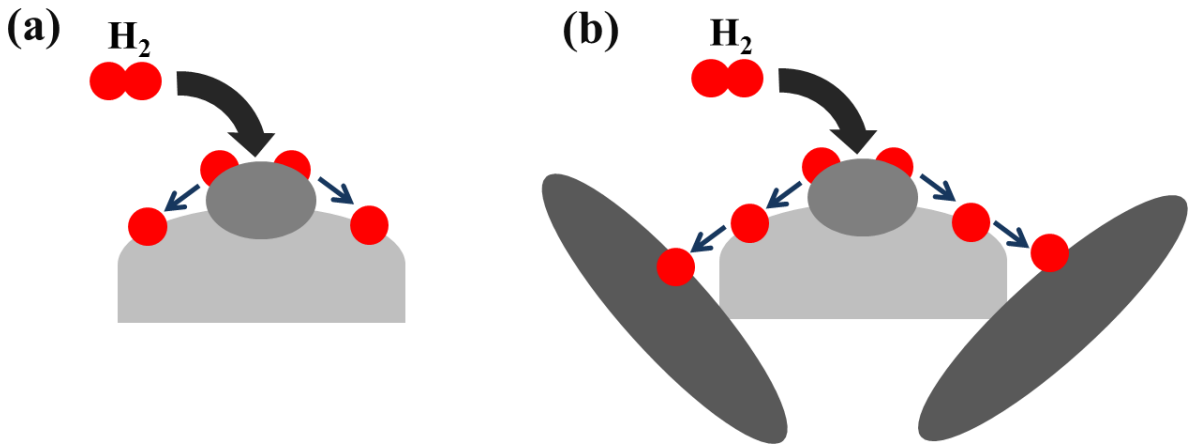


Figure 2.3: Schematic representation of spillover (a) when the activator surface is in direct contact with the accepting surface and (b) when the activator surface is separated by some distance from the accepting surface. Modified from [38].

Conner Jr. and Falconer [33] reported that the surface diffusion/migration of the spiltover species depends on the interaction between the spiltover species and surface on which it migrates. Spillover is reported to occur at the interface of the activator surface and the accepting surface. The interactions may be van der Waals forces or the stronger interactions best represented as activated exchange between adsorption sites that are adjacent to each other. The rate of migration and energy of interaction vary depending on the surface involved. It was observed by Levy and Boudart [39] that alcohol groups or water on the surface may facilitate spillover and surface migration of the spiltover species. From these observations, the diffusion of hydrogen was reported to be assisted by hydroxyl groups on an oxide surface by a "bucket brigade" mechanism [33] which is comparable in certain aspects to the Grotthuss mechanism reported as early as 1806 . The bucket brigade mechanism, shown in (Figure 2.4), shows that the spiltover hydrogen (H_α) from the activator/dissociating

metal (Me^{I}), is passed on to an O atom, and then travels through the secondary surface, an oxide support, by the formation of consecutive OH networks. At the end of the final OH group in the network, another OH group is formed with a species called H_{Ω}. Following this process, H_{Ω} is pushed towards the acceptor/accepting metal (Me^{II}).

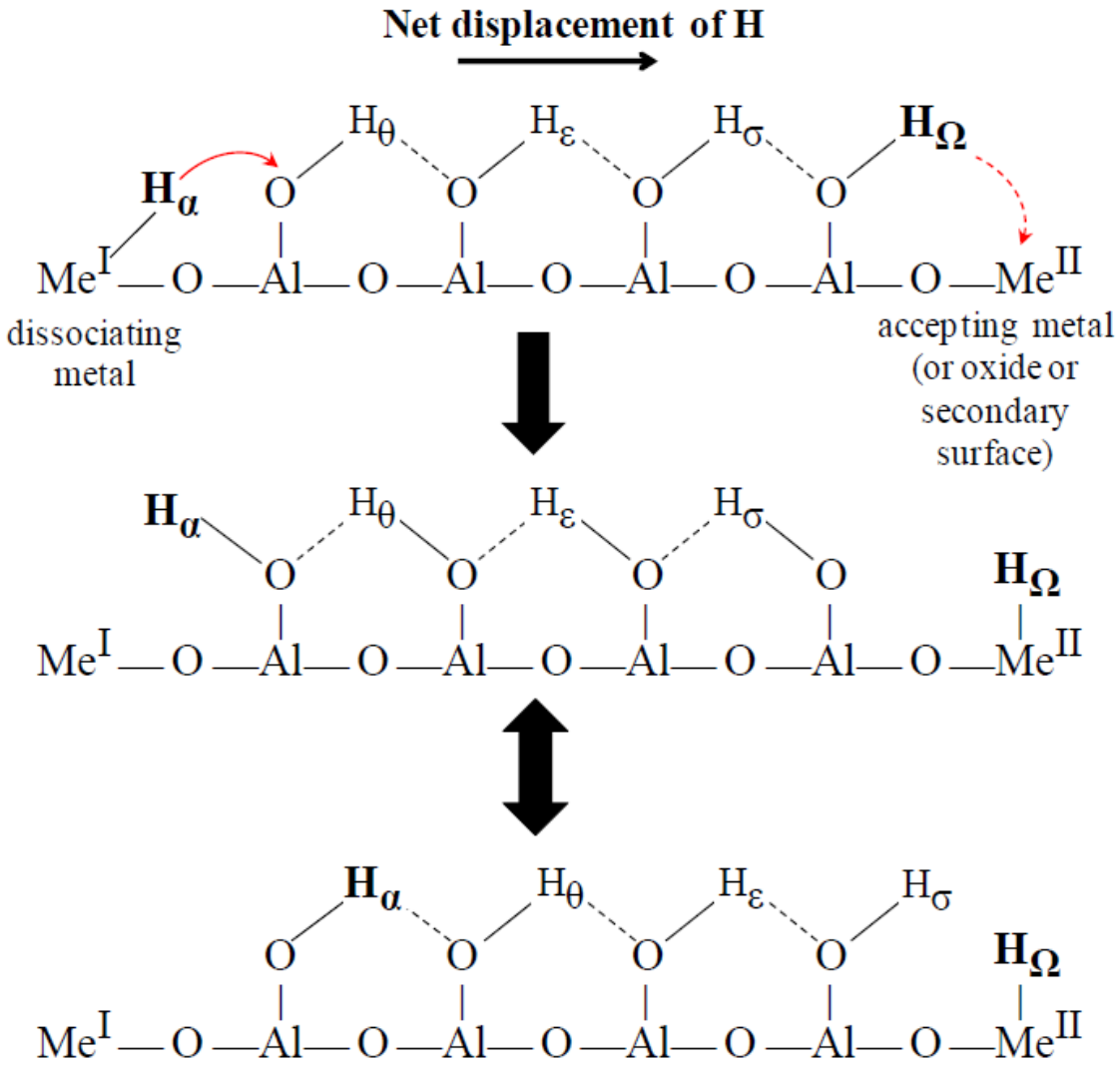


Figure 2.4: Bucket brigrade mechanism illustrating surface migration of hydrogen through formation of hydroxyl networks with the support [30].

Im et el. [40] used Pt encapsulated aluminosilicates to provide direct evidence of the hydrogen spillover phenomenon in the hydrogenation of benzene. They used density functional theory (DFT) to propose a hydrogen spillover mechanism on their catalyst which they attributed to the presence of the surface OH groups (due to Brønsted acid sites) on the aluminosilicates. In the mechanism proposed, (Figure 2.5), defect sites ($[AlO_4H_2]^{+}$ and $[AlO_4]^{-}$) are generated by the movement of protons (H^{+}) from the interior of the framework,

followed by the subsequent movement of these defect sites *via* the movement of the consecutive H^+ species. An H radical (H•) is then added to the $[AlO_4]^-$ defect site resulting in the formation of $[AlO_4]^-$ H *via* formation of a three-centred bond (O-H-O) also regarded as a Brønsted acid site that is distorted by the localised unpaired electron (i.e. polaron). The subsequent migration of this three-centred bond (O-H-O) *via* a polaron conduction mechanism makes way for the cationic defective site to be reached. Therefore, at this defective site an unpaired electron comes into contact with an H^+ which then generates the H• species that is involved in the hydrogenation reaction as the spiltover species. Overall, the mechanism suggests that the hydrogen spillover on to the aluminosilicate, which is non-reducible, is energetically feasible because of the local bond connectivities (O-H and O-H-O bond) and the resulting polaron-type conduction.

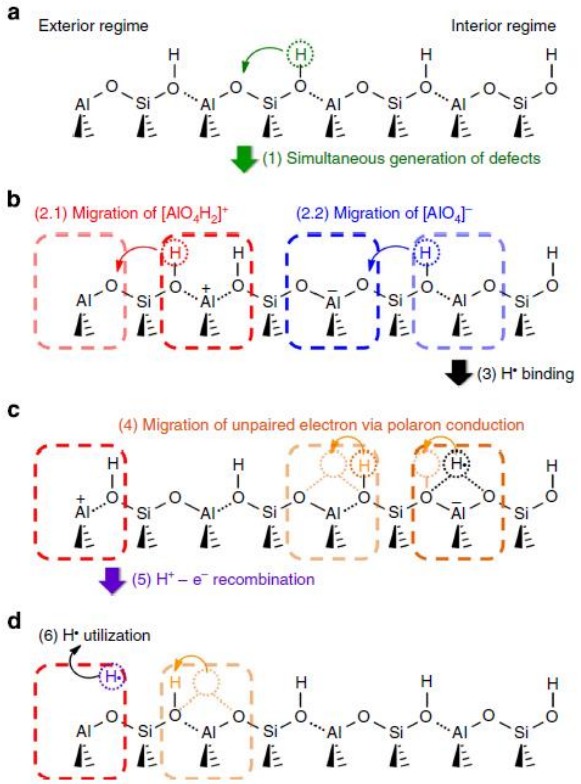


Figure 2.5: Hydrogen spillover mechanism on the aluminosilicate surface [40].

2.2.1. Hydrogen spillover on carbon supports

Large volumes of literature on the mechanistic study of the hydrogen spillover phenomenon have been centred on the use of metal oxide supports. However, it has been shown that carbonaceous supports, particularly graphitic carbon is capable of dissociating hydrogen [41]. This was observed using graphitic carbon nanotubes and carbon nanofibers. The spiltover

hydrogen was reported as being able to intercalate the interlayer spacing in the carbon nanofibers [38, 42]. However, Prins *et al.* [41] reported that hydrogen atoms can also adsorb at defect sites. These defect sites can be generated near the metal particles from the hydrogen reduction of the catalyst which results in methanation of the carbon, catalysed by the metal particles. Meanwhile, C – H bonds are formed which allow hydrogen spillover to the carbon support, from the metal. Evidence of these C – H bonds was observed from the inelastic neutron scattering of hydrogen atoms that were spilled over from Pt and Ru to a carbon black support. The C – H bonds were found to be present at the dangling bonds of the edge sites of carbon [43].

Moreover, it is not only the defect sites on carbon materials that facilitate hydrogen spillover from a metal to the carbon, even oxygen groups can do this. Oxygen functional groups are able to facilitate hydrogen spillover because they are able to serve as direct adsorption sites and facilitate the surface diffusion of hydrogen [44]. For instance, Chung *et al.* [45] supported Pd on oxygenated activated carbon. They observed an enhancement in the hydrogen spillover with an increase in the content of oxygen functionality. Psofogiannakis and Froudakis [46] investigated hydrogen spillover on a graphitic surface with epoxide and hydroxyl groups, and Pt supported on the surface. They observed an easy migration of H atoms on the surface with a low energy barrier and an enhancement in the hydrogen spillover which they attributed to the bridges of carbon containing oxygen functionalities.

2.2.2. Hydrogen spillover in heterogeneous catalysis

Survey of the literature has shown that multi-phase catalysts exhibit an enhanced activity or selectivity. This can be ascribed to hydrogen spillover occurring between the phases. For instance, in a hydrogenation reaction, hydrogen is adsorbed by the supported metal and the support adsorbs the reactant or species to be hydrogenated and the hydrogenation reaction proceeds as a consequence of the hydrogen spillover [47]. Kennedy *et al.* [48] studied the selective hydrogenation of crotonaldehyde. Hydrogenation of crotonaldehyde produces three main products: butyraldehyde, crotyl alcohol, and butanol. The crotyl alcohol is the most desired product due to its role as an intermediate in reactions producing valuable chemicals and fragrances. The catalyst they used was Pt/Co_3O_4. In this reaction, hydrogen was adsorbed or activated on the surface of Pt, and the crotonaldehyde was adsorbed on Co_3O_4. Greater selectivity to the desired crotyl alcohol was due to the reaction between crotonaldehyde and the spiltover hydrogen.

Hydrogen spillover has also been invoked in CO_2 methanation reactions. Schubert *et al.* [49] used Pt-promoted $Co–Al_2O_3$ catalysts. A Pt content of 0.03% was enough to exhibit a dramatic enhancement in the reduction of Co_3O_4 and the subsequent CO_2 hydrogenation reaction, compared to a monometallic $Co–Al_2O_3$ catalyst; this could only be attributed to hydrogen spillover. CO hydrogenation (Fischer-Tropsch synthesis) is also a reaction in which hydrogen spillover may be invoked. It is particularly invoked to explain the role a noble metal plays when it has been incorporated into a Fischer-Tropsch catalyst to activate the catalyst and enhance its reducibility and subsequent catalytic performance. Nabaho *et al.* [30] studied both the primary (using $Pt\text{-}Co/Al_2O_3$) and secondary hydrogen spillover effects (using Pt/Al_2O_3 + Co/Al_2O_3 which is the hybrid Pt-Co catalyst) (Figure 2.6), since the promotion mechanism (hydrogen spillover mechanism) of the supported Co catalyst depends on the location of the promoter.

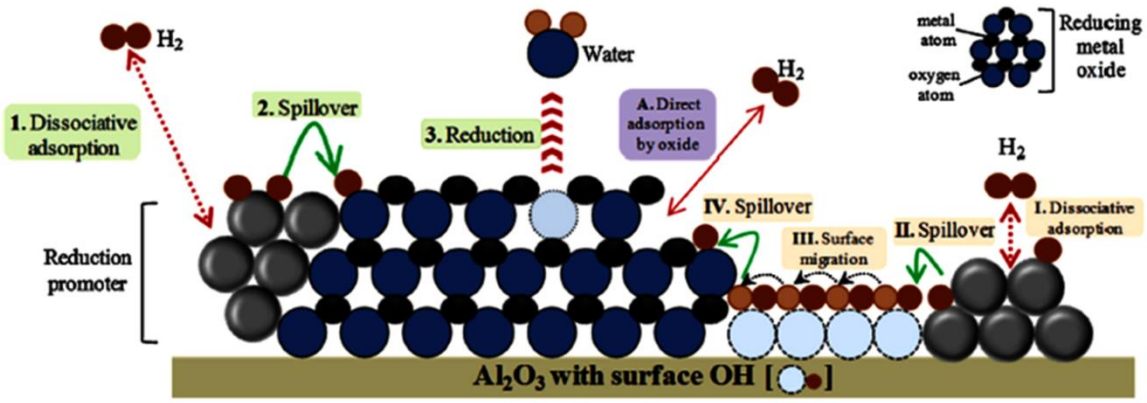


Figure 2.6: Schematic representation of the hydrogen spillover effect [30].

Figure 2.6 illustrates the steps involved in the hydrogen spillover mechanism: (1) hydrogen dissociatively adsorbs on the noble metal reduction promoter (platinum), followed by (2) its subsequent spillover to metal oxide (cobalt oxide) and (3) the reduction of the metal oxide by the reaction between the oxygen on the metal oxide and the hydrogen atoms to produce water and form the metallic phase. Alternatively; (I) hydrogen dissociatively adsorbs on the noble metal reduction promoter (platinum), followed by (II) its subsequent spillover onto the support (alumina) with surface OH groups which facilitate (III) the surface migration of hydrogen, followed by (IV) its spillover onto the metal oxide (cobalt oxide) and finally (3) the reduction of the metal oxide by the reaction between the oxygen on the metal oxide and the hydrogen atoms to produce water and form the metallic phase.

Nabaho *et al.* observed from their TPR data (Figure 2.7) that hydrogen spillover occurred whether or not the promoter (Pt) and the metal oxide (cobalt oxide) were in contact.

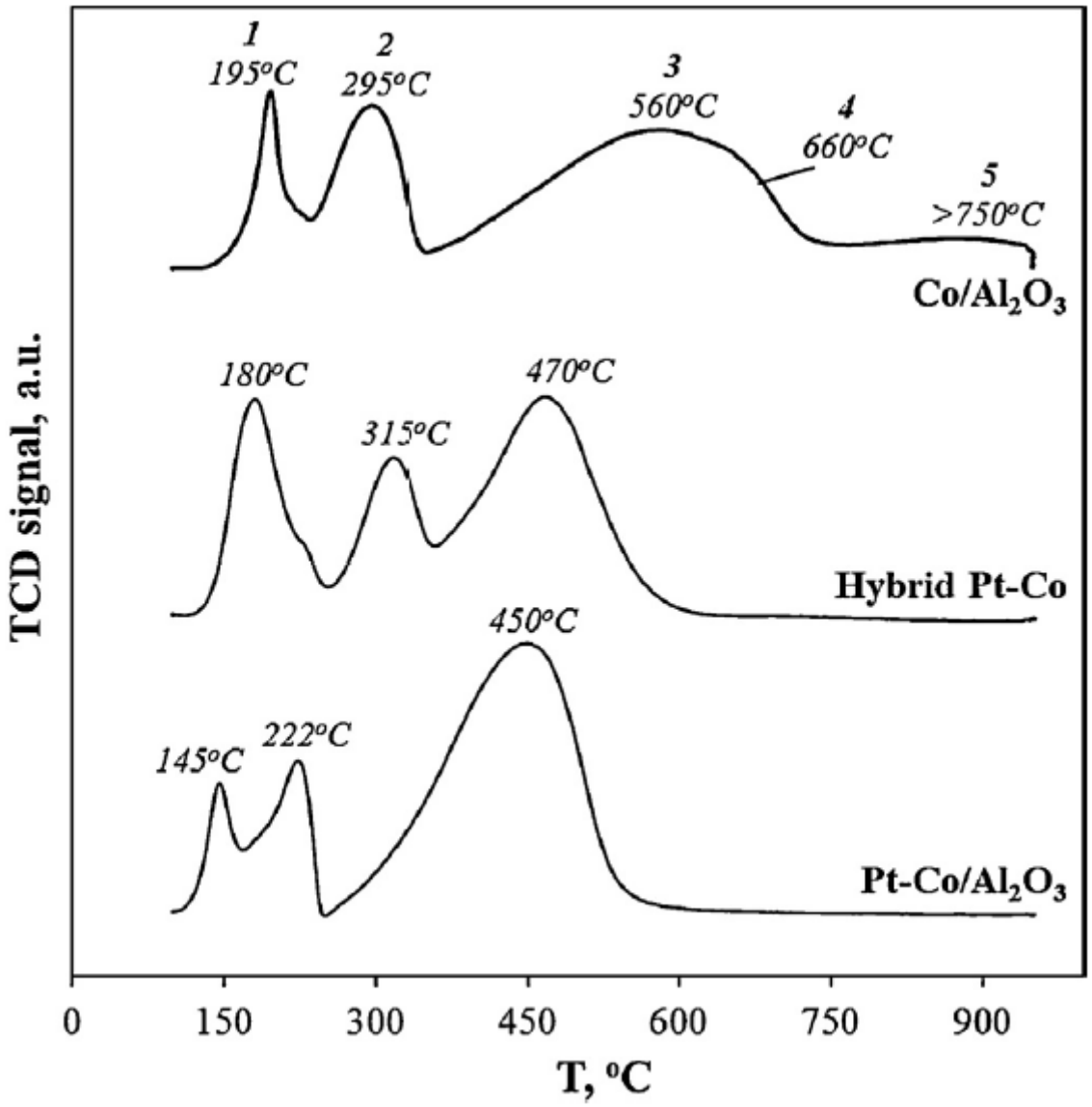


Figure 2.7: TPR profiles of the catalysts supported on Al_2O_3 [30].

Figure 2.7 shows that reducibility increased as follows: Co/Al_2O_3 < hybrid Pt-Co < $Pt-Co/Al_2O_3$. The peak numbers shown represent the following: (1) NO_3^- from the precursor $Co(NO_3)_2$, and probably CoO(OH) [50],(2) Co_3O_4 (3) CoO, (4) CoO interacting with Al_2O_3 (5) strong metal-support interactions resulting in $CoAl_2O_4$. The reduction peaks shifted to lower temperatures with the incorporation of the reduction promoter, Pt. The catalyst in which Pt is in intimate contact with the Co ($Pt-Co/Al_2O_3$) was reported to have exhibited the greatest enhancement in the reducibility of Co and gave a higher TOF in the Fischer-Tropsch reaction due to the synergistic effects between Pt and Co [30]. However, as observed from

their study, the Pt and Co do not need to be in intimate contact for the hydrogen spillover effect to be witnessed.

Phaahlamohlaka et el. [51] also invoked hydrogen spillover in their CO hydrogenation (Fischer-Tropsch synthesis) study. They too showed that the reduction promoter does not have to be in intimate contact with the metal oxide for the hydrogen spillover to occur. They used Ru as the reduction promoter and a Co catalyst supported on mesoporous hollow carbon spheres (MHCSs). To observe the primary hydrogen spillover effect they placed Ru and Co in intimate contact, (Ru-Co/MHCS). To observe the secondary hydrogen spillover effect, they exploited the hollow cavity of the HCSs and the carbon shell thickness to separate Ru and Co. Ru was encapsulated while Co was loaded outside mesoporous HCSs (Co@MHCS@Ru). They too observed enhanced Co reducibility due to the primary hydrogen spillover, when using the Ru-Co/MHCS catalyst, owing to the synergistic effects between Ru and Co.

2.3. Hollow carbon spheres

The name, hollow carbon spheres (HCSs), is based on the morphology of the carbon material. The term 'hollow' refers to an object 'having a hole or an empty space inside' [52]. Hollow carbon spheres are therefore, carbon spheres with a void inside a shell. The hollow cavity in their structures enables them to have a surface area that is significantly larger, a density that is comparably lower, and a higher loading capacity than solid counterparts of the same size. HCSs, thus, owe their vast range of applications, including catalysis [53-55], nanoreactors [56, 57], sensors [58, 59], energy storage [60, 61], to these properties. Hollow carbon spheres (HCS) can be synthesized using two main types of sacrificial templating procedures namely; i) hard-templating and ii) soft-templating methods. In the hard-templating method, solid core particles are utilized as the templates which are then destroyed after carbon deposition on their surfaces to achieve the hollow core structure [53, 56, 62, 63]. The soft-templating method however involves the use of carbon precursors, surfactants, and organic solvents which act as the liquid, "soft" template that will be destroyed during pyrolysis [64-66]. The former method provides better control of the morphology of the hollow structure than the latter method and hence it is the most commonly used method [63].

2.3.1. HCS synthesis using the hard-templating method

Generally, in this method a solid core material, the template, is coated with the desired carbon source. In order to achieve the desired coating, the surface of the templates may be modified

or different methods of carbon deposition may be used [63, 67-69]. Removal of the solid template can be achieved, depending on its chemical composition, by etching [68], or by thermal treatment [70], to obtain the hollow structure of the HCS. The resulting HCSs usually maintain the morphology and size of the template [71]. As a result, the void size of these structures can be tuned to the desired size. There are different types of solid core particles that can be employed, among these are; silica [67], polymers [70] and metallic spheres [72].

2.3.1.1. Silica spheres as templates

A vast amount of literature exists on the use of silica as the sacrificial template for the synthesis of HCSs. Silica gained its popularity due to the ease with which the diameters of silica spheres can be tuned, from nanometer to micrometer sizes, and their porosity, from micro to meso and even macro pores, by simple modification of the synthesis parameters. Typically, they are synthesized following the Stöber method (hence they are also called Stöber spheres) [73] which involves the hydrolysis of alkyl silicates in a mixture of water and ethanol, in the presence of ammonia as a catalyst. However, in order to obtain HCSs, after coverage of the silica with carbon, the silica must be etched out using harsh reagents such as HF [74] or NaOH [75]. Because HCSs fabricated using silica as the template retain the morphology of the silica, it is therefore easy to tune the diameter and porosity of the HCSs. For example, Yoon *et al.* [67], were able to synthesize mesoporous HCSs also referred to as hollow core/mesoporous shell (HCMS) materials, using mesoporous silica also referred to as solid core/mesoporous shell (SCMS) silica structures, as shown in Figure 2.8 below.

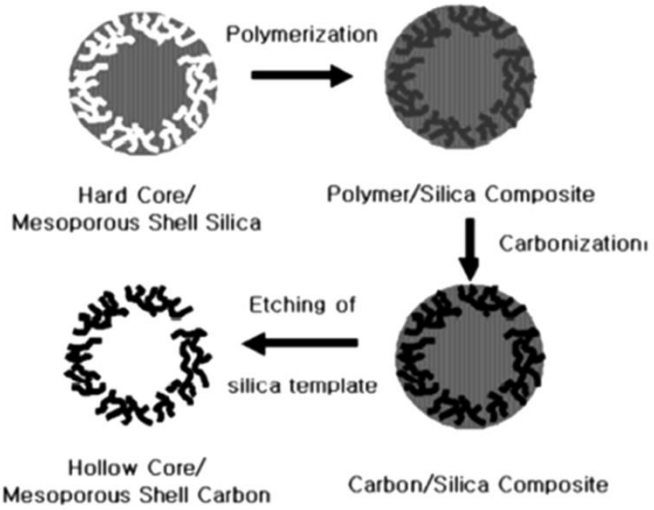


Figure 2.8: Hard-templating synthesis of mesoporous HCS using mesoporous silica spheres [67].

In addition to the template, the reaction conditions such as CVD temperature and time have an effect on the resulting HCSs. Nongwe *et al.* [76], synthesized N-doped HCSs with different shell thicknesses using silica as the template and acetonitrile, as both carbon and nitrogen source, by chemical vapor deposition (CVD). In their synthesis method, it was observed that the morphology of the HCSs depended on the CVD temperature and time. In terms of the CVD temperatures, at higher temperatures; the carbon deposition rate was improved, the HCSs' shell thickness increased and the silica shell thickness shrunk which promoted formation of HCS with a smooth surface. In terms of CVD time, the shell thickness increased with CVD time as shown in the TEM images in Figure 2.9. Similarly, the results of Su *et al.* [68], also showed that in addition to CVD temperature, the morphology of HCS depends on CVD duration and the size of the silica spheres. In terms of CVD duration, a shorter CVD time produces HCSs with a smaller shell thickness resulting in sphere deformity. The silica spheres with a diameter greater than 500 nm were observed to produce HCS with a smooth surface.

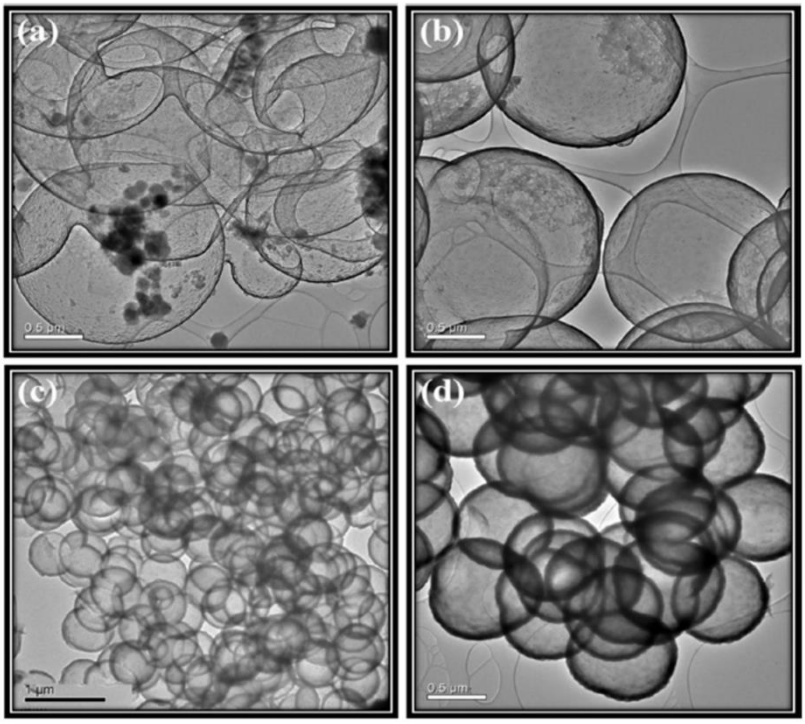


Figure 2.9: TEM images of N-HCSs obtained using silica spheres that are 1100 nm in size and different CVD times for (a) N-HCS900-1, (b) N-HCS900-2, (c) N-HCS900-3 and (d) N-HCS900-4 [76].

Although the CVD method of carbonization has been widely used for the synthesis of HCSs, there are other methods that have been reported which do not involve the infiltration of the

carbon precursor into the pores of the silica spheres. This is not always successful due to the possibility of aggregation of particles leading to the formation of non-uniform porous HCSs [63]. In addition, because the CVD method involves the use of high temperatures for the carbonization step which results in the formation of HCSs with an aromatic surface and hydrophobic character, their widespread use especially in the field of catalysis may be limited. To address this, Valle-Vigón *et al.* [77], reported a simple method for fabricating HCSs with uniform pores which involved use of the solid core-mesoporous shell (SCMS) silica spheres functionalized with the organic composite (-$(CH_2)_{17}$-CH_3) which acts both as a carbon precursor and a porogen. Sulphuric acid was used to convert the composite into carbon. This was achieved following dehydration and sulphonation reactions, the latter reaction being responsible for the aromatization and crosslinking. After pyrolysis, the HCSs obtained had a uniform morphology with a surface area of 1620 m^2 g^{-1}, a pore volume of 2.3 cm^3 g^{-1} and a porosity consisting of mesopore sizes equal to 4.3 nm.

Another approach, which was inspired by the Stöber method, involves the polymerization of resorcinol-formaldehyde (RF) resins (as the carbon source) on silica [78], a method that was reported by Fuertes *et al.* [79], who deposited a layer of RF carbon source on silica to form silica@RF spheres in a one-pot synthesis procedure. They outlined the mechanism through which its formation occurs and this is illustrated in (Figure 2.10 a). The first step involves the rapid generation of the classic Stöber spheres on which the NH_4^+ ions are formed, which are attracted to the negative surface of the silica spheres, resulting in a stable colloidal suspension. Parallel to the reaction occurring in the first step is the slower reaction between resorcinol and formaldehyde catalyzed by OH^- and resulting in the formation of hydroxymethyl-substituted species. The hydroxymethyl-substituted species then diffuses to the surface of the silica spheres due to the electrostatic attraction between them and the NH_4^+ ions, and condensation then occurs on the surface of the silica spheres resulting in the formation of the RF polymer around the silica spheres, to produce the silica@RF composite.

The composite was then carbonized and the silica etched out to produce HCSs (Figure 2.10 b) that can have a wide range of diameters from 20 to 450 nm. Zhang *et al.* [80] were able to further develop the method to produce bi- and tri-layered HCSs by repeatedly adding the silica and RF precursors at different time intervals, resulting in HCSs with a diameter, shell thickness, and interlayer spacing of 450 nm, 12 nm and 20 nm, respectively. Pyrolysis is usually undertaken in a horizontal tube furnace under an inert gas flow such as nitrogen, argon, or helium at temperatures between 600 °C and 2100 °C [81]. The effect of the

pyrolysis temperature on the RF resins has been studied and it was discovered that higher pyrolysis temperatures lead to RF carbon aerogels with smaller surface areas, and smaller pore volumes and pore sizes [81-83].

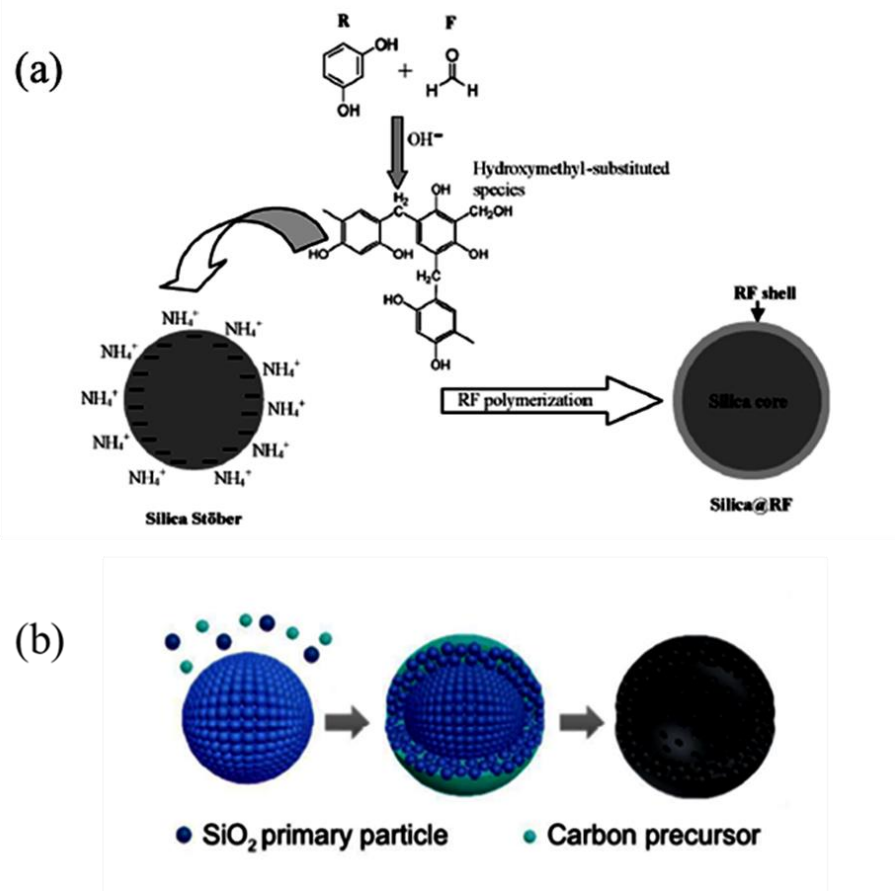


Figure 2.10: a) Synthesis scheme of silica@RF sphere [79] and b) *in-situ* Stöber templating process for HCS synthesis [80].

Furthermore Lui *et al.*[53], used dopamine as the carbon source to synthesize HCSs that were doped with nitrogen exploiting the ability of dopamine to produce a high carbonization yield as a result of its characteristics that are similar to those of phenolic resins. Similar to RF resins coated on silica, dopamine was used in a one-pot assembly of the carbon source on the template that was achieved by polymerization of dopamine on to the silica spheres to form the polymer/silica composite. The composite then underwent pyrolysis in nitrogen to convert the dopamine into a carbon layer.

2.3.1.2. Polymer spheres as templates

Polymer nanoparticles can also be used as templates, polystyrene (PS) and its derivatives being the most commonly used. Polystyrene spheres can be easily synthesized and easily

removed to produce the hollow core of the HCSs, by thermal decomposition or by dissolving them in N,N-dimethylformamide (DMF). Several methods have been reported on the synthesis of HCSs using PS. For instance, Hu *et al.* [84] used PS as a template and glucose as a carbon source. They employed the microwave-assisted synthesis of the HCSs, with both the template removal and the carbonization steps taking place, simultaneously.

In addition, Arif *et al.* [85], in a similar manner, synthesized N-doped HCSs using 3-aminophenol as the carbon source, and also as the nitrogen source. A facile method was reported by Fu *et al.* [86], involving the pyrolysis of PS spheres coated with poly(cyclotriphosphazene-*co*-4,4′-sulfonyldiphenol) (PZS) to synthesize HCSs, which they referred to as hollow core porous shell (HCPS) carbon spheres. The synthesis route is illustrated in Figure 2.11. The PZS was used as the carbon precursor and showed some favourable properties such as being easily coated onto the PS spheres at room temperature, without the need for surfactants and the ease with which its thickness can be controlled, by varying the ratio of amount of the co-monomer to that of the PS.

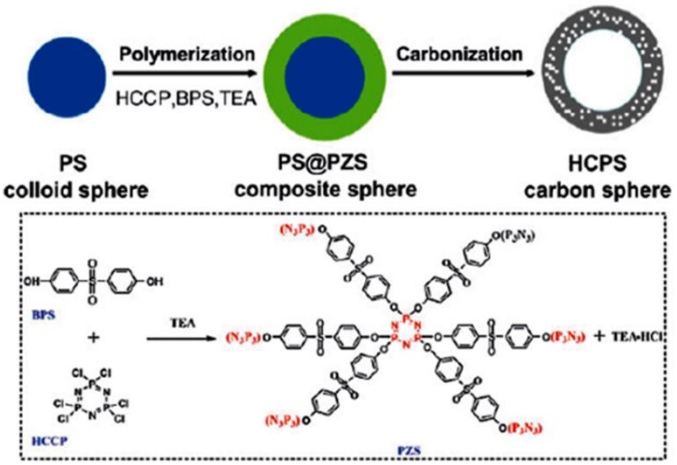


Figure 2.11: Synthesis procedure of HCPS carbon spheres [86].

In a slightly different approach, Han *et al.* [87], functionalized PS spheres by adding sulfonic acid groups that strongly bound to the polyaniline (PANI), used as the carbon and nitrogen source, to synthesize porous N-doped HCSs (PNHCSs), shown in Figure 2.12. The sulfonated PS (SPS) spheres formed a SPS@PANI composite after they were coated with PANI. The SPS was then removed by dissolving the composite in DMF, resulting in hollow polyaniline spheres (HPSs) which were then carbonized under a flow of nitrogen to give the desired PNHCSs (Figure 2.13).

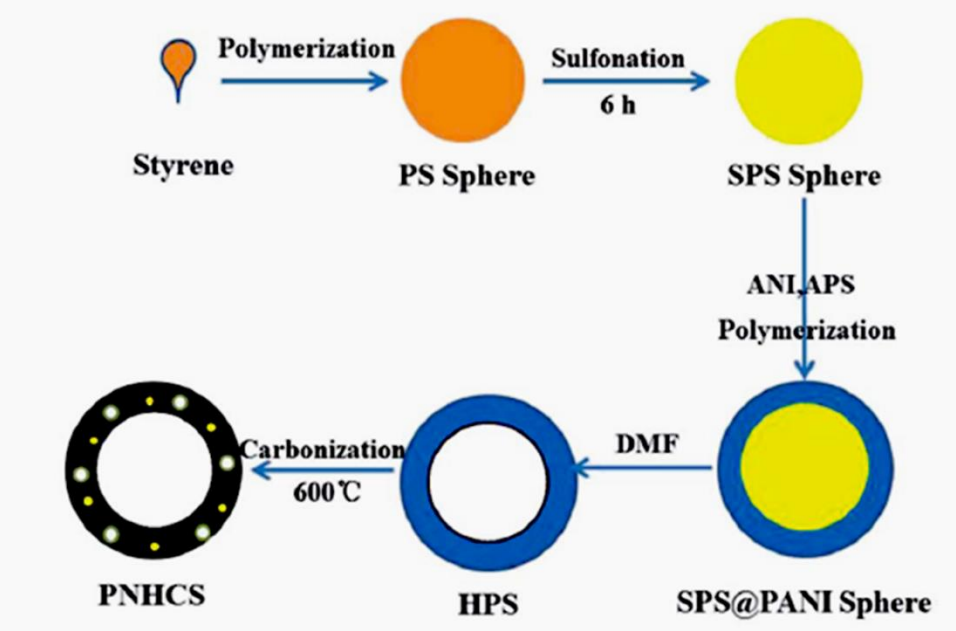


Figure 2.12: Synthesis of PNHCS using SPS as a template [87].

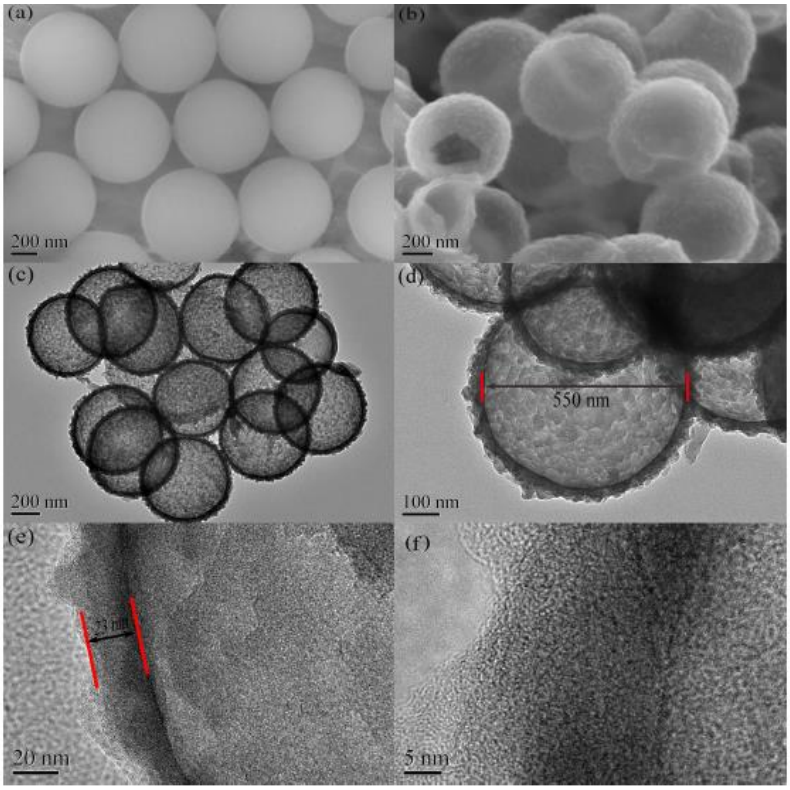


Figure 2.13: (a) SEM image of SPS template, (b) PNHCS obtained using SPS as a template (c – d) PNHCS at different magnifications [87].

2.3.2. HCS synthesis using the soft-templating method

The soft-templating method generally does not involve the synthesis and removal of a hard template. This method involves use of easily removable soft templates such as emulsion droplets, micelles/vesicles, or gas bubbles as the template. However, it is challenging to obtain monodisperse, spherical HCSs using these templates due to their polydispersity and the general nature of the soft templates [63]. Jia and co-workers [88] synthesized HCSs with Cu particles embedded in the carbon shell using the soft-templating approach. Trioctylamine droplets in an oil-in-water emulsion were used as the soft template. Hydrothermal conditions were used for the bonding of these emulsion droplets with Cu^{2+} particles and ascorbic acid to reduce the Cu^{2+} particles due to the ascorbic acid. In the process the ascorbic acid was converted into hydrothermal carbon (Figure 2.14).

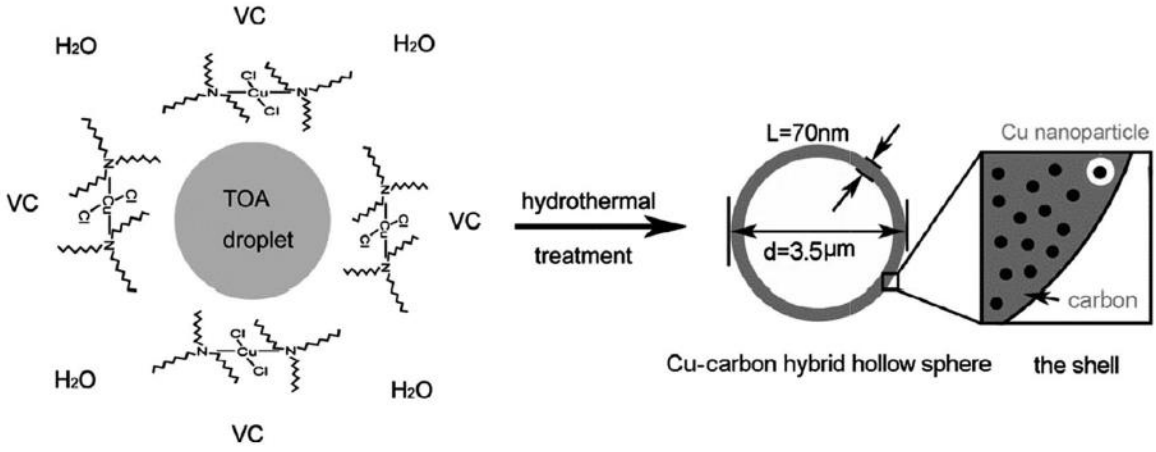


Figure 2.14: Formation of HCSs using trioctylamine droplets in an oil-in-water emulsion and a solution containing Cu–amine complexes and ascorbic acid, by hydrothermal treatment [88].

Wang *et al.* [54] used the soft-templating approach to synthesize Pt-Co encapsulated HCSs. They used a tri-block copolymer (P_{123}) and sodium oleate. The P_{123} is known to have a strong interaction with ionic surfactants, forming micelles. The micelles were then mixed with an acidic solution to form emulsion droplets, which make up the soft template. These were used to make hollow polymer spheres (HPSs) which were converted into HCSs by pyrolysis (Figure 2.15).

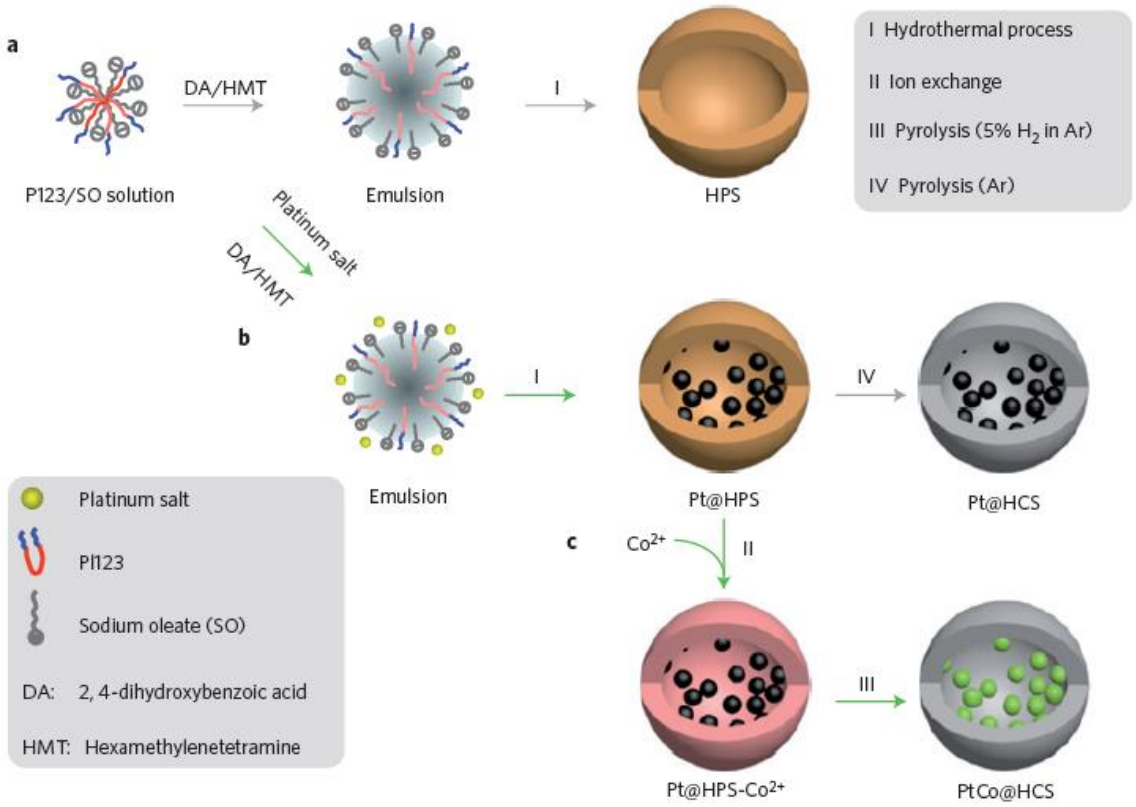


Figure 2.15: Schematic illustration of the synthesis of (a) HCSs, (b) Pt@HCS and (c) PtCo@HCS [54].

2.3.3. Hollow carbon spheres applications

HCSs have garnered great research attention due to their desirable properties. These properties include; high specific surface area, low density, tunable pore volume, great mechanical stability, chemical inertness and their inner void. As a result of their properties, they have found use in energy storage and more especially in catalysis, as a support for transition metals that are usually active as catalysts. Certainly, because of their inner void, they can act as nanoreactors and encapsulate the catalytically active species, and because of their tunable pore sizes, they can allow reactant species to diffuse through the carbon shell to the catalytically active species and the resulting products can also diffuse out of the void through the pores.

2.3.3.1. Energy storage

HCSs play a pivotal role in energy storage and conversion technologies with regards to the cutting edge innovations therein. At a time when there is an increasing demand for energy, these materials are showing great potential in contributing towards achieving cleaner,

efficient, and cost-effective devices to meet the growing need for energy. They have been successfully used as efficient electrodes in supercapacitors and as supports in fuel cells.

- **Supercapacitors**

The study of HCSs has become an important research area in energy storage applications as electrode materials for supercapacitors. They have superseded other carbon forms such as graphene, activated carbon, carbon nanotubes, and carbon spheres because of their properties which include; a high surface area, inner void and tunable pores that facilitate reduced mass/charge transport length and resistance, resulting in rapid mass/charge transport and higher capacitance. For instance, Bhattacharjya *et al.* [89] used HCSs with meso/micropores as an electrode material, comparing its performance with that of activated carbon. They reported a high capacitance of 162 F g^{-1} which is more than twice that achieved using activated carbon. Zhao *et al.* [90] fabricated HCSs with a surface area and pore volume equal to 2239 m^2 g^{-1} and 3.56 cm^3 g^{-1}, respectively, and they reported a capacitance of 268 F g^{-1} which they found to be significantly higher than results obtained when using conventional carbon forms. Moreover, recent studies have shown that modifying HCSs by adding dopants such as N or O or varying their architecture from single shell to double shell can improve the specific capacitance of the supercapacitors. For instance, Liu *et al.* [91] synthesized N-doped HCSs with a single and also with a double shell architecture. They reported that the single shell N-doped HCS exhibited a capacitance of 280 F g^{-1} while the N-doped HCSs exhibited that of 381 F g^{-1} which showed improved capacitance with N-doping and an excellent improvement when using the double shell architecture. Zhao *et al.* [90] modified the surface of their HCSs by adding a layer of poly aniline (PANI) onto a HCS, resulting in a greatly enhanced capacitance equal to 525 F g^{-1}.

- **Fuel cells**

Conventionally, noble metals such as Pt and Ru are used as the catalyst material in the fabrication of an electrode for a fuel cell. However, these metals are very expensive making it difficult to commercialize fuel cells. Therefore, in order to reduce the amount of these metals used, researchers have resolved to develop high surface area support materials, and obtain fuel cells that are cost-effective and still efficient. For instance, Wen *et al.* [92] synthesized HCSs upon which they deposited Pt to obtain a Pt/HCS electrode, for use in the direct methanol fuel cell (DMFC). They observed that the methanol oxidation and the overall catalytic activity was greatly enhanced in comparison to when Pt was deposited on conventional carbon supports such as carbon black powder, Vulcan XC-72, and carbon

microspheres, CMS. They attributed the performance of Pt/HCS to the good dispersion of Pt achieved on the HCSs.

2.3.3.2. HCS in catalysis

A vast amount of material properties must be taken into consideration when designing a catalyst. Among these is the catalyst support, since supported catalysts represent a large portion of the economically important catalysts that are used in industry. Therefore, fabricating novel catalyst supports that will greatly improve the performance of a catalyst continues to garner increasing research interest. Among the catalyst supports that have become important are HCSs. This is due to their properties that can be used to enhance their role in many applications, with specific attention given to their use as catalyst supports in hydrogenation reactions.

- **Hydrogenation reactions**

HCSs have been used in a wide range of hydrogenation reactions. For instance, Lui *et al.* [53] used HCSs to encapsulate Au nanoparticles in the synthesis of a catalyst for the reduction of 4-nitrophenol to 4-aminophenol by $NaBH_4$. They observed that this catalyst exhibited greater stability and resulted in an accelerated rate of reaction and enhanced activity in comparison to Au nanoparticles encapsulated in SiO_2 and polymer structures. Ng *et al.* [93] used HCSs to encapsulate Pt nanoparticles for use as a catalyst in the hydrogenation of primary, secondary and cyclic olefins. Their results showed 99% conversions of the 1-hexene and 2-hexene, and 98% conversion of the cyclohexene, which is significantly greater than when using Pt supported on activated carbon.

2.4. Conclusion

This chapter included a brief background on the Fischer-Tropsch (FT) process. Although there are several FT catalysts that exist, as mentioned in the chapter, particular attention was given to the cobalt FT catalyst due to its relevance to this study. Optimization of the cobalt catalyst's FT performance was reported. This involved, among others, the enhancement of its reducibility such that its active phase is present at lower temperatures, owing to the typical use of a cobalt catalyst in the low temperature FT reaction. Incorporation of noble metal promoters proved to be efficient in facilitating this, as discussed in the chapter. The mechanism through which these promoters facilitate the enhancement in the cobalt reducibility, which is the hydrogen spillover effect, was discussed. It was also shown that

indeed platinum is one of the efficient noble metal promoters in that it can enhance the reducibility of the cobalt FT catalyst and improve its FT activity.

Furthermore, cobalt FT catalysts are often supported on a catalyst support and the drawbacks such as metal-support interactions and of using conventional metal oxide supports such as alumina, silica, and titania, were discussed. Cobalt supported on carbon supports, due to its relative chemical inertness, was also discussed. A comprehensive review on the synthesis of hollow carbon spheres (HCSs) was included in the chapter due to our interest in using them as a support for the cobalt FT catalyst. Particular attention was given to the hard templating method of synthesizing the HCSs due to its advantages over the soft-templating method. The different types of hard templates, carbon precursors, and conditions that can be used to synthesize these HCSs were described in detail. Finally, the different applications where these HCSs have been used, were reported.

2.5. References

[1] I. Chorkendorff, J.W. Niemantsverdriet, Concepts of modern catalysis and kinetics, John Wiley & Sons, 2017.

[2] E. de Smit, B.M. Weckhuysen, The renaissance of iron-based Fischer–Tropsch synthesis: on the multifaceted catalyst deactivation behaviour, Chemical Society Reviews 37 (2008) 2758-2781.

[3] G. Ertl, H. Knözinger, J. Weitkamp, Handbook of heterogeneous catalysis, (1997).

[4] H. Schulz, Short history and present trends of Fischer–Tropsch synthesis, Applied Catalysis A: General 186 (1999) 3-12.

[5] F. Morales, B.M. Weckhuysen, Promotion effects in Co-based Fischer-Tropsch catalysis, Catalysis 19 (2006).

[6] M. Dry, J. Hoogendoorn, Technology of the Fischer-Tropsch process, Catalysis Reviews—Science and Engineering 23 (1981) 265-278.

[7] M.E. Dry, High quality diesel *via* the Fischer–Tropsch process–a review, Journal of Chemical Technology & Biotechnology: International Research in Process, Environmental & Clean Technology 77 (2002) 43-50.

[8] M.K. Gnanamani, G. Jacobs, W.D. Shafer, B.H. Davis, Fischer–Tropsch synthesis: Activity of metallic phases of cobalt supported on silica, Catalysis today 215 (2013) 13-17.

[9] Y. Traa, Is a renaissance of coal imminent?—challenges for catalysis, Chemical Communications 46 (2010) 2175-2187.

[10] S. Mousavi, A. Zamaniyan, M. Irani, M. Rashidzadeh, Generalized kinetic model for iron and cobalt based Fischer–Tropsch synthesis catalysts: review and model evaluation, Applied Catalysis A: General 506 (2015) 57-66.

[11] P. Biloen, W. Sachtler, Mechanism of hydrocarbon synthesis over Fischer-Tropsch catalysts, Adv. Catal 30 (1981) 165-216.

[12] B.H. Davis, Fischer–Tropsch synthesis: current mechanism and futuristic needs, Fuel Processing Technology 71 (2001) 157-166.

[13] G.P. Van Der Laan, A. Beenackers, Kinetics and selectivity of the Fischer–Tropsch synthesis: a literature review, Catalysis Reviews 41 (1999) 255-318.

[14] T. Fu, Z. Li, Review of recent development in Co-based catalysts supported on carbon materials for Fischer–Tropsch synthesis, Chemical Engineering Science 135 (2015) 3-20.

[15] A.Y. Khodakov, Fischer-Tropsch synthesis: Relations between structure of cobalt catalysts and their catalytic performance, Catalysis Today 144 (2009) 251-257.

[16] R. Zhang, H. Liu, Q. Li, B. Wang, L. Ling, D. Li, Insight into the role of the promoters Pt, Ru and B in inhibiting the deactivation of Co catalysts in Fischer-Tropsch synthesis, Applied Surface Science 453 (2018) 309-319.

[17] V. De la Peña O'Shea, N. Homs, J. Fierro, P.R. de la Piscina, Structural changes and activation treatment in a Co/SiO2 catalyst for Fischer–Tropsch synthesis, Catalysis today 114 (2006) 422-427.

[18] O. Ducreux, B. Rebours, J. Lynch, M. Roy-Auberger, D. Bazin, Microstructure of supported cobalt Fischer-Tropsch catalysts, Oil & Gas Science and Technology-Revue de l'IFP 64 (2009) 49-62.

[19] G. Jacobs, T.K. Das, Y. Zhang, J. Li, G. Racoillet, B.H. Davis, Fischer–Tropsch synthesis: support, loading, and promoter effects on the reducibility of cobalt catalysts, Applied Catalysis A: General 233 (2002) 263-281.

[20] O. Akbarzadeh, N. Mohd Zabidi, Y. Abdul Wahab, N. Hamizi, Z. Chowdhury, Z. Merican Aljunid Merican, M. Ab Rahman, S. Akhter, E. Rasouli, M. Johan, Effect of Cobalt Catalyst Confinement in Carbon Nanotubes Support on Fischer-Tropsch Synthesis Performance, Symmetry 10 (2018) 572.

[21] W. Xie, Y. Zhang, K. Liew, J. Li, Effect of catalyst confinement and pore size on Fischer-Tropsch synthesis over cobalt supported on carbon nanotubes, Science China Chemistry 55 (2012) 1811-1818.

[22] F. Diehl, A.Y. Khodakov, Promotion of cobalt Fischer-Tropsch catalysts with noble metals: a review, Oil & Gas Science and Technology-Revue de l'IFP 64 (2009) 11-24.

[23] S.K. Beaumont, S. Alayoglu, C. Specht, N. Kruse, G.A. Somorjai, A nanoscale demonstration of hydrogen atom spillover and surface diffusion across silica using the kinetics of CO2 methanation catalyzed on spatially separate Pt and Co nanoparticles, Nano letters 14 (2014) 4792-4796.

[24] J.-S. Girardon, E. Quinet, A. Griboval-Constant, P. Chernavskii, L. Gengembre, A. Khodakov, Cobalt dispersion, reducibility, and surface sites in promoted silica-supported Fischer–Tropsch catalysts, Journal of Catalysis 248 (2007) 143-157.

[25] Z. Zsoldos, T. Hoffer, L. Guczi, Structure and catalytic activity of alumina-supported platinum-cobalt bimetallic catalysts. 1. Characterization by x-ray photoelectron spectroscopy, The Journal of Physical Chemistry 95 (1991) 798-801.

[26] Z. Zsoldos, L. Guczi, Structure and catalytic activity of alumina supported platinum-cobalt bimetallic catalysts. 3. Effect of treatment on the interface layer, The Journal of Physical Chemistry 96 (1992) 9393-9400.

[27] G. Jacobs, T.K. Das, P.M. Patterson, J. Li, L. Sanchez, B.H. Davis, Fischer–Tropsch synthesis XAFS: XAFS studies of the effect of water on a Pt-promoted Co/Al2O3 catalyst, Applied Catalysis A: General 247 (2003) 335-343.

[28] W. Chu, P.A. Chernavskii, L. Gengembre, G.A. Pankina, P. Fongarland, A.Y. Khodakov, Cobalt species in promoted cobalt alumina-supported Fischer–Tropsch catalysts, Journal of Catalysis 252 (2007) 215-230.

[29] G. Jacobs, J.A. Chaney, P.M. Patterson, T.K. Das, J.C. Maillot, B.H. Davis, Fischer-Tropsch synthesis: Study of the promotion of Pt on the reduction property of Co/Al2O3 catalysts by in situ EXAFS of Co K and Pt LIII edges and XPS, Journal of synchrotron radiation 11 (2004) 414-422.

[30] D. Nabaho, J.H. Niemantsverdriet, M. Claeys, E. van Steen, Hydrogen spillover in the Fischer–Tropsch synthesis: an analysis of platinum as a promoter for cobalt–alumina catalysts, Catalysis Today 261 (2016) 17-27.

[31] H. Zhang, W. Chu, C. Zou, Z. Huang, Z. Ye, L. Zhu, Promotion effects of platinum and ruthenium on carbon nanotube supported cobalt catalysts for Fischer–Tropsch synthesis, Catalysis letters 141 (2011) 438-444.

[32] W. Karim, C. Spreafico, A. Kleibert, J. Gobrecht, J. VandeVondele, Y. Ekinci, J.A. van Bokhoven, Catalyst support effects on hydrogen spillover, Nature 541 (2017) 68.

[33] W.C. Conner Jr, J.L. Falconer, Spillover in heterogeneous catalysis, Chemical reviews 95 (1995) 759-788.

[34] G. Gardes, G. Pajonk, S. Teichner, Catalytic demonstration of hydrogen spillover from nickel-alumina catalyst to alumina, Journal of Catalysis 33 (1974) 145-148.

[35] P. Emmett, Physical adsorption in the study of the catalyst surface, Reports of the Committee on Contact Catalysis, Division of Chemistry and Chemical Technology... (1940) 53.

[36] S. Khoobiar, Particle to particle migration of hydrogen atoms on platinum—alumina catalysts from particle to neighboring particles, The Journal of Physical Chemistry 68 (1964) 411-412.

[37] S. Triwahyono, A.A. Jalil, S.N. Timmiati, N.N. Ruslan, H. Hattori, Kinetics study of hydrogen adsorption over Pt/MoO3, Applied Catalysis A: General 372 (2010) 103-107.

[38] A.D. Lueking, R.T. Yang, Hydrogen spillover to enhance hydrogen storage—study of the effect of carbon physicochemical properties, Applied Catalysis A: General 265 (2004) 259-268.

[39] R. Levy, M. Boudart, The kinetics and mechanism of spillover, Journal of Catalysis 32 (1974) 304-314.

[40] J. Im, H. Shin, H. Jang, H. Kim, M. Choi, Maximizing the catalytic function of hydrogen spillover in platinum-encapsulated aluminosilicates with controlled nanostructures, Nature communications 5 (2014) 3370.

[41] R. Prins, Hydrogen spillover. Facts and fiction, Chemical reviews 112 (2012) 2714-2738.

[42] D.J. Browning, M.L. Gerrard, J.B. Lakeman, I.M. Mellor, R.J. Mortimer, M.C. Turpin, Studies into the storage of hydrogen in carbon nanofibers: proposal of a possible reaction mechanism, Nano Letters 2 (2002) 201-205.

[43] P.C. Mitchell, A.J. Ramirez-Cuesta, S.F. Parker, J. Tomkinson, D. Thompsett, Hydrogen spillover on carbon-supported metal catalysts studied by inelastic neutron scattering. Surface vibrational states and hydrogen riding modes, The Journal of Physical Chemistry B 107 (2003) 6838-6845.

[44] G.M. Psofogiannakis, G.E. Froudakis, Fundamental studies and perceptions on the spillover mechanism for hydrogen storage, Chemical Communications 47 (2011) 7933-7943.

[45] T.-Y. Chung, C.-S. Tsao, H.-P. Tseng, C.-H. Chen, M.-S. Yu, Effects of oxygen functional groups on the enhancement of the hydrogen spillover of Pd-doped activated carbon, Journal of colloid and interface science 441 (2015) 98-105.

[46] G.M. Psofogiannakis, G.E. Froudakis, DFT study of hydrogen storage by spillover on graphite with oxygen surface groups, Journal of the American Chemical Society 131 (2009) 15133-15135.

[47] V.V.e. Rozanov, O.V. Krylov, Hydrogen spillover in heterogeneous catalysis, Russian chemical reviews 66 (1997) 107-119.

[48] G. Kennedy, G.r.m. Melaet, H.-L. Han, W.T. Ralston, G.A. Somorjai, In Situ Spectroscopic Investigation into the Active Sites for Crotonaldehyde Hydrogenation at the Pt Nanoparticle–Co3O4 Interface, ACS Catalysis 6 (2016) 7140-7147.

[49] M. Schubert, S. Pokhrel, A. Thomé, V. Zielasek, T.M. Gesing, F. Roessner, L. Mädler, M. Bäumer, Highly active Co–Al 2 O 3-based catalysts for CO 2 methanation with very low platinum promotion prepared by double flame spray pyrolysis, Catalysis Science & Technology 6 (2016) 7449-7460.

[50] J. Van de Loosdrecht, S. Barradas, E. Caricato, N. Ngwenya, P. Nkwanyana, M. Rawat, B. Sigwebela, P. Van Berge, J. Visagie, Calcination of Co-based Fischer–Tropsch synthesis catalysts, Topics in catalysis 26 (2003) 121-127.

[51] T.N. Phaahlamohlaka, D.O. Kumi, M.W. Dlamini, R. Forbes, L.L. Jewell, D.G. Billing, N.J. Coville, Effects of Co and Ru Intimacy in Fischer–Tropsch Catalysts Using Hollow Carbon Sphere Supports: Assessment of the Hydrogen Spillover Processes, ACS Catalysis 7 (2017) 1568-1578.

[52] X. Wang, J. Feng, Y. Bai, Q. Zhang, Y. Yin, Synthesis, properties, and applications of hollow micro-/nanostructures, Chemical reviews 116 (2016) 10983-11060.

[53] R. Liu, S.M. Mahurin, C. Li, R.R. Unocic, J.C. Idrobo, H. Gao, S.J. Pennycook, S. Dai, Dopamine as a carbon source: the controlled synthesis of hollow carbon spheres and yolk-structured carbon nanocomposites, Angewandte Chemie International Edition 50 (2011) 6799-6802.

[54] G.-H. Wang, J. Hilgert, F.H. Richter, F. Wang, H.-J. Bongard, B. Spliethoff, C. Weidenthaler, F. Schüth, Platinum–cobalt bimetallic nanoparticles in hollow carbon

nanospheres for hydrogenolysis of 5-hydroxymethylfurfural, Nature materials 13 (2014) 293.

[55] Z. Zhang, F. Xiao, J. Xi, T. Sun, S. Xiao, H. Wang, S. Wang, Y. Liu, Encapsulating Pd nanoparticles in double-shelled graphene@ carbon hollow spheres for excellent chemical catalytic property, Scientific reports 4 (2014) 4053.

[56] X. Fang, J. Zang, X. Wang, M.-S. Zheng, N. Zheng, A multiple coating route to hollow carbon spheres with foam-like shells and their applications in supercapacitor and confined catalysis, Journal of Materials Chemistry A 2 (2014) 6191-6197.

[57] G.-H. Wang, J. Hilgert, F.H. Richter, F. Wang, H.-J. Bongard, B. Spliethoff, C. Weidenthaler, F. Schüth, Platinum–cobalt bimetallic nanoparticles in hollow carbon nanospheres for hydrogenolysis of 5-hydroxymethylfurfural, Nature Materials 13 (2014) 293.

[58] B.K. Mutuma, R. Rodrigues, K. Ranganathan, B. Matsoso, D. Wamwangi, I.A. Hümmelgen, N.J. Coville, Hollow carbon spheres and a hollow carbon sphere/polyvinylpyrrolidone composite as ammonia sensors, Journal of Materials Chemistry A 5 (2017) 2539-2549.

[59] C. Zhang, R. Zhang, X. Gao, C. Cheng, L. Hou, X. Li, W. Chen, Small Naked Pt Nanoparticles Confined in Mesoporous Shell of Hollow Carbon Spheres for High-Performance Nonenzymatic Sensing of H2O2 and Glucose, ACS Omega 3 (2018) 96-105.

[60] Z. Chen, S. Ye, S.D. Evans, Y. Ge, Z. Zhu, Y. Tu, X. Yang, Energy Storage: Confined Assembly of Hollow Carbon Spheres in Carbonaceous Nanotube: A Spheres-in-Tube Carbon Nanostructure with Hierarchical Porosity for High-Performance Supercapacitor (Small 19/2018), Small 14 (2018) 1870089.

[61] F. Xu, Z. Tang, S. Huang, L. Chen, Y. Liang, W. Mai, H. Zhong, R. Fu, D. Wu, Facile synthesis of ultrahigh-surface-area hollow carbon nanospheres for enhanced adsorption and energy storage, Nature Communications 6 (2015) 7221.

[62] R.J. White, K. Tauer, M. Antonietti, M.-M. Titirici, Functional Hollow Carbon Nanospheres by Latex Templating, Journal of the American Chemical Society 132 (2010) 17360-17363.

[63] S. Li, A. Pasc, V. Fierro, A. Celzard, Hollow carbon spheres, synthesis and applications–a review, Journal of Materials Chemistry A 4 (2016) 12686-12713.

[64] J. Liu, T. Yang, D.-W. Wang, G.Q. Lu, D. Zhao, S.Z. Qiao, A facile soft-template synthesis of mesoporous polymeric and carbonaceous nanospheres, Nature Communications 4 (2013) 2798.

[65] C. Liang, Z. Li, S. Dai, Mesoporous Carbon Materials: Synthesis and Modification, Angewandte Chemie International Edition 47 (2008) 3696-3717.

[66] Y. Meng, D. Gu, F. Zhang, Y. Shi, L. Cheng, D. Feng, Z. Wu, Z. Chen, Y. Wan, A. Stein, A family of highly ordered mesoporous polymer resin and carbon structures from organic− organic self-assembly, Chemistry of materials 18 (2006) 4447-4464.

[67] S.B. Yoon, K. Sohn, J.Y. Kim, C.-H. Shin, J.-S. Yu, T. Hyeon, Fabrication of Carbon Capsules with Hollow Macroporous Core/Mesoporous Shell Structures, Advanced Materials 14 (2002) 19-21.

[68] F. Su, X.S. Zhao, Y. Wang, L. Wang, J.Y. Lee, Hollow carbon spheres with a controllable shell structure, Journal of Materials Chemistry 16 (2006) 4413-4419.

[69] X. Chen, K. Kierzek, Z. Jiang, H. Chen, T. Tang, M. Wojtoniszak, R.J. Kalenczuk, P.K. Chu, E. Borowiak-Palen, Synthesis, Growth Mechanism, and Electrochemical Properties of Hollow Mesoporous Carbon Spheres with Controlled Diameter, The Journal of Physical Chemistry C 115 (2011) 17717-17724.

[70] X.-y. Dai, X. Zhang, Y.-f. Meng, P.-k. Shen, Preparation of hollow carbon spheres by carbonization of polystyrene/polyaniline core-shell polymer particles, New Carbon Materials 26 (2011) 389-395.

[71] S. Kubo, R. Demir-Cakan, L. Zhao, R.J. White, M.M. Titirici, Porous Carbohydrate-Based Materials *via* Hard Templating, ChemSusChem: Chemistry & Sustainability Energy & Materials 3 (2010) 188-194.

[72] F.-L. Wang, L.-L. Pang, Y.-Y. Jiang, B. Chen, D. Lin, N. Lun, H.-L. Zhu, R. Liu, X.-L. Meng, Y. Wang, Simple synthesis of hollow carbon spheres from glucose, Materials Letters 63 (2009) 2564-2566.

[73] W. Stöber, A. Fink, E. Bohn, Controlled growth of monodisperse silica spheres in the micron size range, Journal of Colloid and Interface Science 26 (1968) 62-69.

[74] J.B. Joo, P. Kim, W. Kim, J. Kim, N.D. Kim, J. Yi, Simple preparation of hollow carbon sphere *via* templating method, Current Applied Physics 8 (2008) 814-817.

[75] B. Fang, J.H. Kim, M.-S. Kim, A. Bonakdarpour, A. Lam, D.P. Wilkinson, J.-S. Yu, Fabrication of hollow core carbon spheres with hierarchical nanoarchitecture for ultrahigh electrical charge storage, Journal of Materials Chemistry 22 (2012) 19031-19038.

[76] I. Nongwe, V. Ravat, R. Meijboom, N.J. Coville, Pt supported nitrogen doped hollow carbon spheres for the catalysed reduction of cinnamaldehyde, Applied Catalysis A: General 517 (2016) 30-38.

[77] P. Valle-Vigón, M. Sevilla, A.B. Fuertes, Synthesis of Uniform Mesoporous Carbon Capsules by Carbonization of Organosilica Nanospheres, Chemistry of Materials 22 (2010) 2526-2533.

[78] A.-H. Lu, G.-P. Hao, Q. Sun, Can Carbon Spheres Be Created through the Stöber Method?, Angewandte Chemie International Edition 50 (2011) 9023-9025.

[79] A.B. Fuertes, P. Valle-Vigón, M. Sevilla, One-step synthesis of silica@resorcinol–formaldehyde spheres and their application for the fabrication of polymer and carbon capsules, Chemical Communications 48 (2012) 6124-6126.

[80] H. Zhang, M. Yu, H. Song, O. Noonan, J. Zhang, Y. Yang, L. Zhou, C. Yu, Self-organized mesostructured hollow carbon nanoparticles *via* a surfactant-free sequential heterogeneous nucleation pathway, Chemistry of Materials 27 (2015) 6297-6304.

[81] S.A. Al-Muhtaseb, J.A. Ritter, Preparation and properties of resorcinol–formaldehyde organic and carbon gels, Advanced materials 15 (2003) 101-114.

[82] E.J. Zanto, S.A. Al-Muhtaseb, J.A. Ritter, Sol− gel-derived carbon aerogels and xerogels: Design of experiments approach to materials synthesis, Industrial & engineering chemistry research 41 (2002) 3151-3162.

[83] R.W. Pekala, C.T. Alviso, F.M. Kong, S.S. Hulsey, Aerogels derived from multifunctional organic monomers, Journal of Non-Crystalline Solids 145 (1992) 90-98.

[84] F.P. Hu, Z. Wang, Y. Li, C. Li, X. Zhang, P.K. Shen, Improved performance of Pd electrocatalyst supported on ultrahigh surface area hollow carbon spheres for direct alcohol fuel cells, Journal of Power Sources 177 (2008) 61-66.

[85] A.F. Arif, Y. Kobayashi, R. Balgis, T. Ogi, H. Iwasaki, K. Okuyama, Rapid microwave-assisted synthesis of nitrogen-functionalized hollow carbon spheres with high monodispersity, Carbon 107 (2016) 11-19.

[86] J. Fu, Q. Xu, J. Chen, Z. Chen, X. Huang, X. Tang, Controlled fabrication of uniform hollow core porous shell carbon spheres by the pyrolysis of core/shell polystyrene/cross-linked polyphosphazene composites, Chemical Communications 46 (2010) 6563-6565.

[87] J. Han, G. Xu, B. Ding, J. Pan, H. Dou, D.R. MacFarlane, Porous nitrogen-doped hollow carbon spheres derived from polyaniline for high performance supercapacitors, Journal of Materials Chemistry A 2 (2014) 5352-5357.

[88] B. Jia, M. Qin, Z. Zhang, A. Chu, L. Zhang, Y. Liu, H. Lu, X. Qu, One-pot synthesis of Cu–carbon hybrid hollow spheres, Carbon 62 (2013) 472-480.

[89] D. Bhattacharjya, M.-S. Kim, T.-S. Bae, J.-S. Yu, High performance supercapacitor prepared from hollow mesoporous carbon capsules with hierarchical nanoarchitecture, Journal of Power Sources 244 (2013) 799-805.

[90] Z. Lei, Z. Chen, X. Zhao, Growth of polyaniline on hollow carbon spheres for enhancing electrocapacitance, The Journal of Physical Chemistry C 114 (2010) 19867-19874.

[91] C. Liu, J. Wang, J. Li, R. Luo, J. Shen, X. Sun, W. Han, L. Wang, Controllable synthesis of functional hollow carbon nanostructures with dopamine as precursor for supercapacitors, ACS applied materials & interfaces 7 (2015) 18609-18617.

[92] Z. Wen, Q. Wang, Q. Zhang, J. Li, Hollow carbon spheres with wide size distribution as anode catalyst support for direct methanol fuel cells, Electrochemistry communications 9 (2007) 1867-1872.

[93] Y.H. Ng, S. Ikeda, T. Harada, S. Higashida, T. Sakata, H. Mori, M. Matsumura, Fabrication of hollow carbon nanospheres encapsulating platinum nanoparticles using a photocatalytic reaction, Advanced Materials 19 (2007) 597-601.

Chapter 3: Material Synthesis and Characterization Techniques

This chapter includes a description of the various synthesis techniques used to prepare the support, hollow carbon spheres (HCSs), and HCSs containing metal nanoparticles inside and outside the HCSs. Described, also in this chapter, are the various characterization techniques used to evaluate the physico-chemical properties of the materials synthesized and the method used to test the materials in the FT reaction.

3.1. Chemicals and gases

All chemicals used were of analytical grade. Styrene (Aldrich), polyvinylpyrollidone (PVP, MW 40 000, Aldrich), cobalt nitrate hexahydrate (Aldrich), ethylene glycol (Aldrich), ammonia solution (25%; Fluka), potassium persulfate (KPS, Eimer and Amend), hexadecyltrimethylammonium bromide (CTAB; Aldrich), chloroplatinic acid hydrate (Aldrich), hydrazine (50%, Aldrich), ethanol (99%; Merck), 2 – butanol (99%. Merck), isopropanol (99%, Merck). Ultra high purity (UHP) Nitrogen (Afrox). They were all used as purchased.

3.1.1. Synthesis of Polystyrene Spheres (PSs)

Ethanol (50 ml) and water (200 ml) were added into a 500 ml round-bottom flask fitted with a condenser and a magnetic stirrer placed inside it, and the solution was allowed to stir for 5 min. A styrene monomer (16 ml) and 0.2 g of PVP were then added into the flask and the mixture was allowed to stir for 10 min. To the resulting solution, 0.3 g of KPS (which was dissolved in 20 ml of water) was then added and the solution was stirred for another 10 min. The mixture was then heated to 80 °C and kept at that temperature for 24 h. The resulting product was then obtained by centrifugation at 18000 rpm for 15 min, washed with ethanol and then dried at 40 °C in the oven for 12 h. Once dry, the product was allowed to cool to room temperature and then ground to a fine powder for use as the template.

3.1.2. Loading of Co or CoPt on PS (Co/PS or CoPt/PS)

PSs (3 g) were dispersed by sonication for 30 min in 100 ml water – ethanol solution (75 and 25 ml, respectively). To this solution, $Co(NO_3)_2.6H_2O$ (0.445 g) was added while stirring until it completely dissolved. Deposition of Co nanoparticles was performed by slow addition

of a solution of hydrazine (10 ml, 2 M). The solution was then left to stir at room temperature for 12 h to ensure complete deposition of the Co nanoparticles. The resulting Co/PSs composite was placed in an oven for 12 h to dry at 40 °C. The bimetallic CoPt/PS composite was synthesized similarly, by mixing $Co(NO_3)_2 \cdot 6H_2O$ (0.445 g) with $H_2PtCl_6 \cdot 6H_2O$ (1.54 ml, 0.05 M) before nanoparticle precipitation. The cobalt and platinum loading was 10% and 0.5% respectively.

3.1.3. Synthesis of Co or CoPt nanoparticles in HCSs (Co@HCS or CoPt@HCS)

A mixture of Co/PS or CoPt/PS (3 g) and ammonia solution (25%, 2 ml) were dispersed by sonication for 30 min in 200 ml of ethanol – water solution (150 ml ethanol and 50 ml water). A mixture of resorcinol (1.13 g), formaldehyde solution (37%, 2 ml) and CTAB (1.5 g) and ethanol (50 ml), was then added to the Co/PS or CoPt/PS. The mixture was then left to stir at room temperature for 20 h and then heated to 80 °C to fully polymerize the resorcinol-formaldehyde (RF) polymer around the Co/PS or CoPt/PS. The resulting composite, Co/PS@RF, or CoPt/PS@RF, was then filtered and washed repeatedly with water followed by drying at 80 °C for 12 h. The removal of the PS template and carbonization were performed by a one-step procedure inside a horizontal tube furnace. The Co/PS@RF or CoPt/PS@RF was heated inside the horizontal tube furnace under a N_2 flow (50 ml/min) at a heating rate of 5 °C/min at 350 °C for 1 h to remove the polystyrene template by thermal decomposition. It was then further heated to 600 °C for 2 h to carbonize the composite. This resulted in the formation of Co@HCS, or CoPt@HCS.

3.1.4. Loading of Pt on Co@HCS (Co@HCS@Pt)

Co@HCS (0.2 g) was dispersed in 40 ml of ethylene glycol by ultrasonication. $H_2PtCl_6 \cdot H_2O$ (0.05 M, 1.54 ml) and ascorbic acid (50 mg) were then added to the mixture, and the mixture was sonicated for 15 min. The mixture was then heated for 4 h at 70 °C. The resulting Co@HCS@Pt sample was collected by vacuum filtration, washed several times with ethanol and water, and dried at 120 °C overnight.

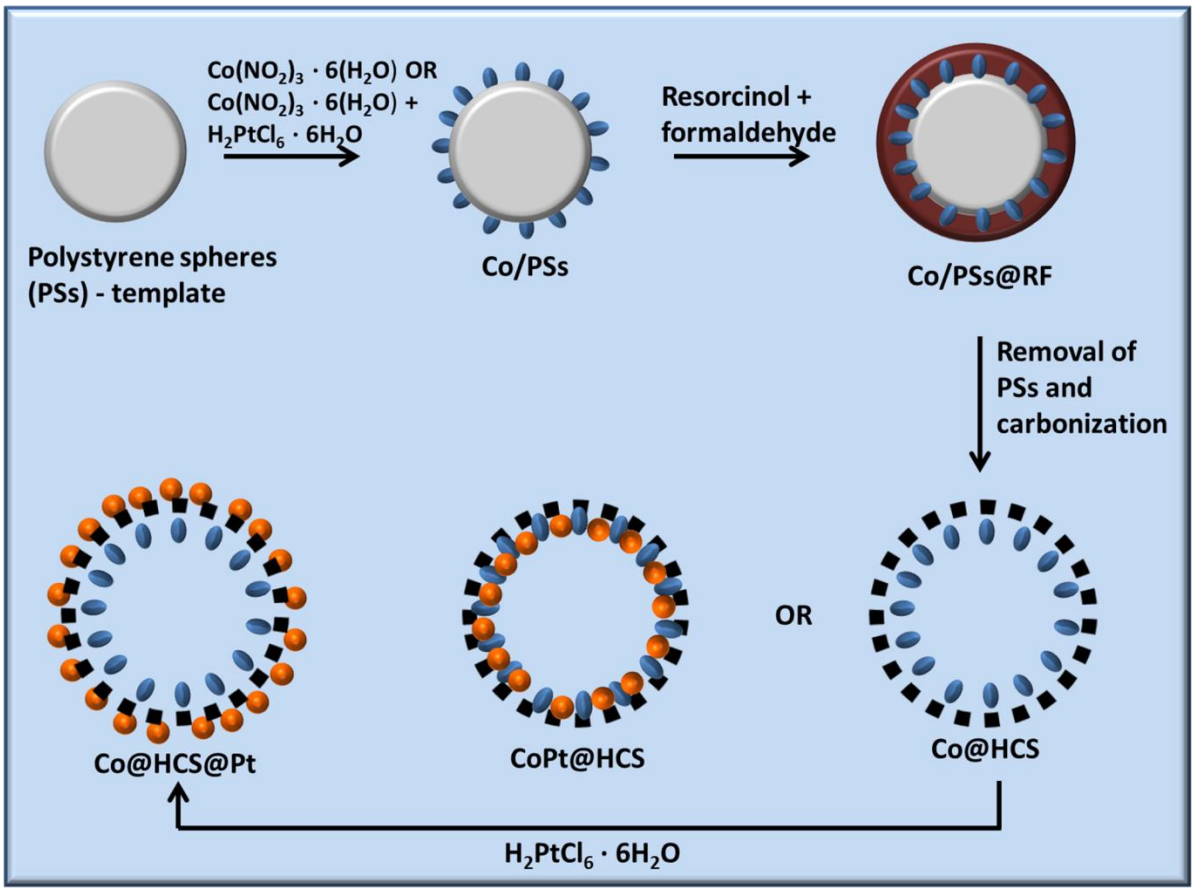


Figure 3.1: A schematic representation of the synthesis of Co@HCS, CoPt@HCS and Co@HCS@Pt.

3.2. Material characterization

3.2.1. Scanning electron microscopy (SEM)

Scanning Electron Microscopy (SEM) analysis was carried out to study the surface morphologies of the samples. The preparation of the specimen for SEM analysis was carried out by applying a thin layer of the samples to be analysed on a conductive carbon tape using a sputter coater which was then stuck on a stub. SEM analysis of the samples was performed using an FEI Nova Nanolab 600 scanning electron microscope (Figure 3.2) operated at 30 kV and 0.63 nA.

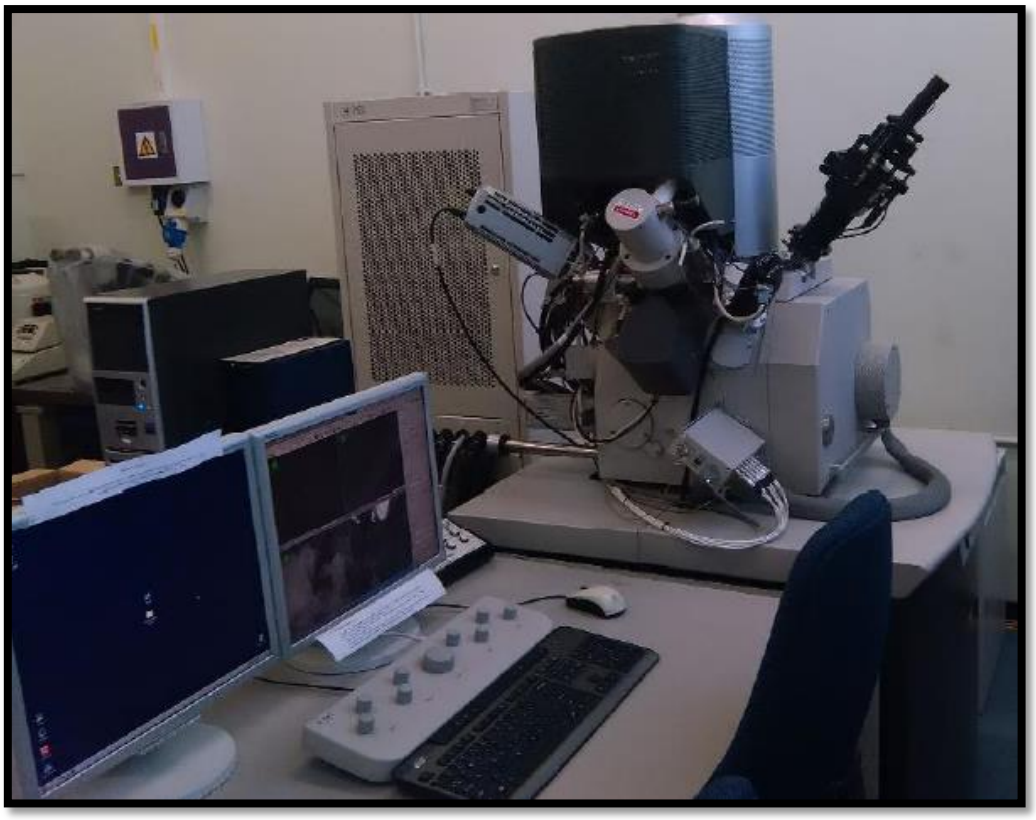


Figure 3.2: FEI Nova Nanolab 600 scanning electron microscope.

3.2.2. Transmission electron microscopy (TEM)

TEM analysis of the samples was carried out to study the morphology and sizes of the support materials and the catalyst particles synthesized. The preparation of the samples for TEM analysis involved dispersing the samples by ultrasonication, in ethanol, and then transferring a drop of the resulting suspension onto a carbon-coated copper grid and leaving it to dry. The analysis was then carried out using an FEI Tecnai T12 transmission electron microscope (Figure 3.3) operating at 120 kV.

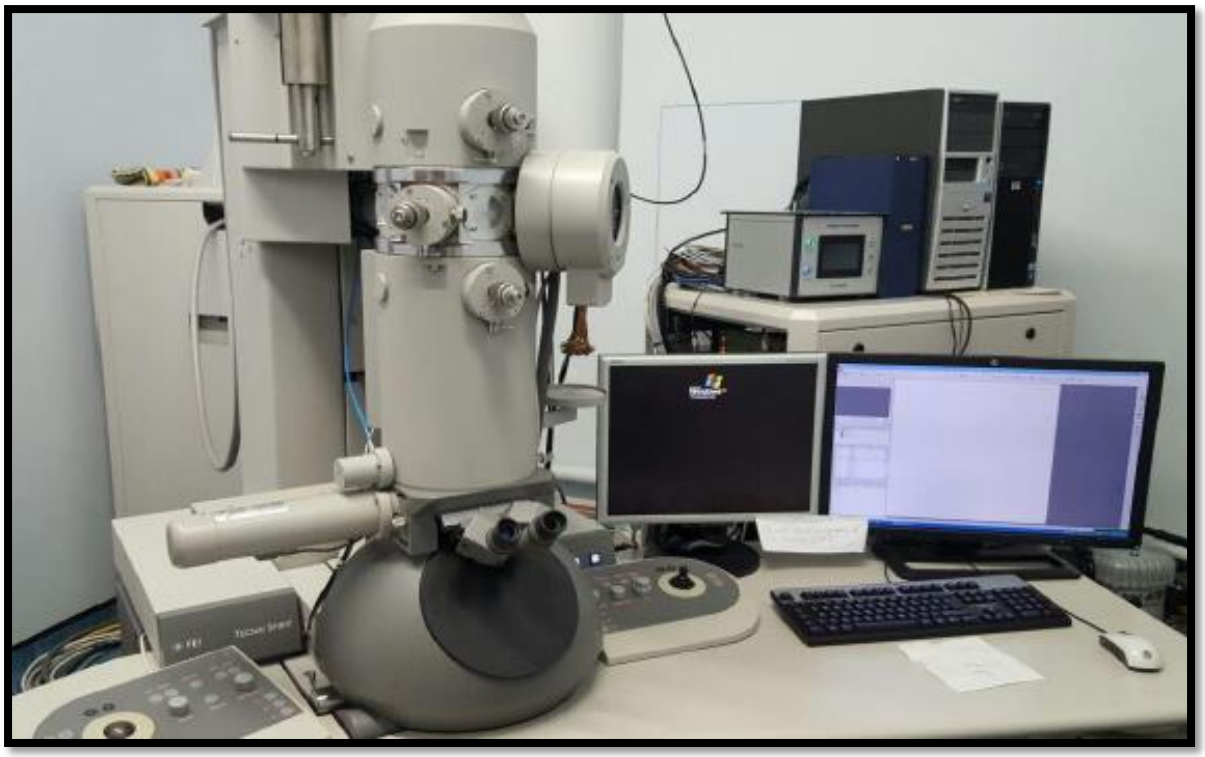


Figure 3.3: FEI Tecnai T12 transmission electron microscope.

3.2.3. Nitrogen Physisorption and BET Method

The determination of the porosity and surface area of the samples was carried out by conducting N_2 physisorption experiments using the Brunauer–Emmett–Teller (BET) method. The sample preparation involved degassing the samples of mass 0.2 g using a Micromeritics Flow Prep 060 unit (Figure 3.4, left) at 120 °C, for 4 h under a N_2 flow. The Micromeritics TriSta 3000 instrument (Figure 3.4, right) was then used for the porosity and surface analysis of the samples at -195 °C, giving the N_2 adsorption data. The surface area data was obtained in the relative pressure, P/P_0 range 0.05 - 0.30 and the pore volume data was obtained at the relative pressure P/P_0 of 0.995. The pore size distributions were evaluated from the desorption branches of the N_2 isotherms obtained using the Barrett−Joyner−Halenda (BJH) method [1].



Figure 3.4: Micromeritics Flow Prep 060 unit (left) and Micromeritics TriSta 3000 instrument (right).

3.2.4. Powder X-ray Diffraction (PXRD)

The determination of the phase composition of the samples was performed by PXRD analysis [2] using the Bruker D2 phaser (Figure 3.5) fitted with a Lynxeye detector, using a Ni-filtered, Cu-Kα radiation at 30 kV and 10 mA. The scan range that was used was $5° < 2\theta < 90°$ in 0.0260° steps. The phases present on the measured PXRD patterns were identified by a comparison with the data stored in databases by using the EVA software package.

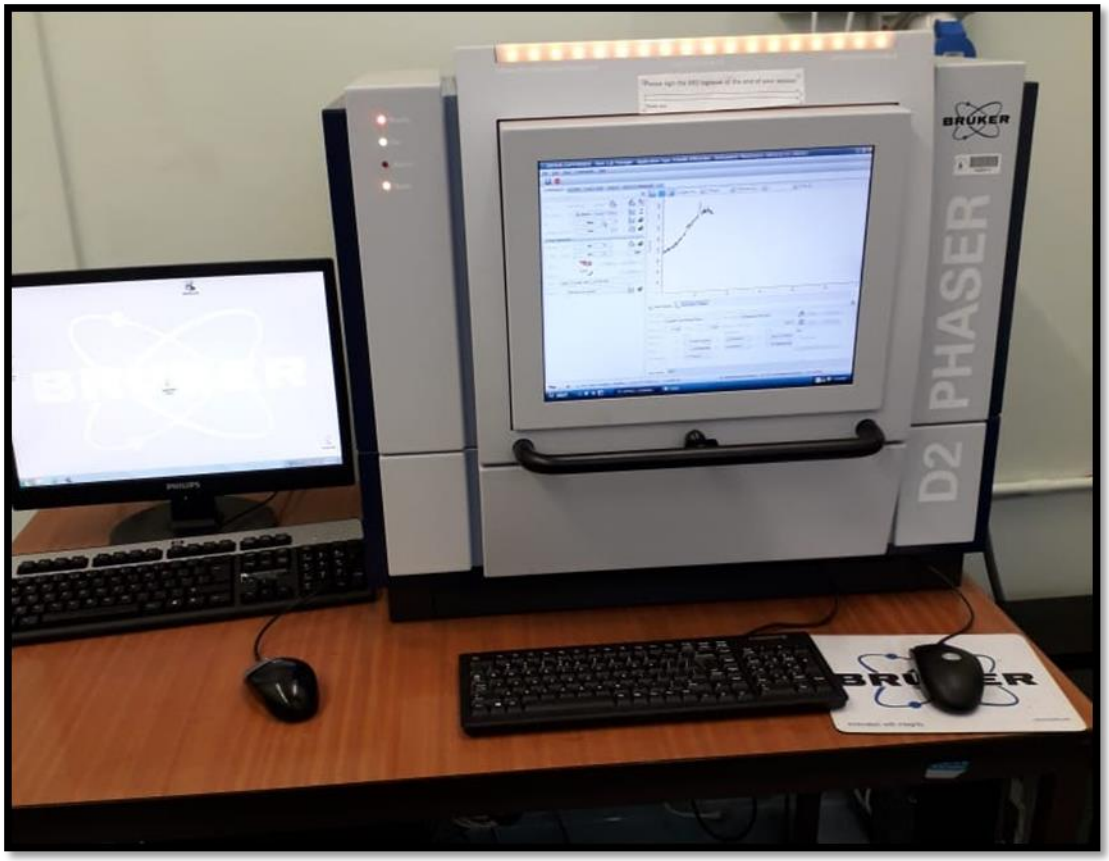


Figure 3.5: Bruker D2 Phaser powder x-ray diffraction benchtop instrument.

In-situ XRD analysis was performed on the catalysts to gain some insight on the reduction behaviour of the catalysts. These reduction studies were carried out in an Anton-Paar XRK900 furnace under flowing H_2 atmosphere (high purity, 1 atm) which enabled the *in situ* monitoring of the reduction behaviour of the catalysts. The XRK900 was attached to a Bruker D8 Advance diffractometer (Figure 3.6) equipped with; a Cu Kα X-ray source (40KV, 40 mA), 0.6 mm fixed divergent slit, 2.5° primary and secondary beam Söller slits, and a VÅNTEC linear position sensitive detector (LPSD) with an effective angular range of 12° 2θ. PXRD data was collected every 20 °C in the temperature range from 30 °C – 350 °C. The crystalline phase identification was performed using DIFFRAC.EVA (Release 2014) using the ICDD PDF2 database (Release 2016). Phase quantification was performed using the Rietveld method as implemented in the Bruker AXS TOPAS software (Version 5, 2014).

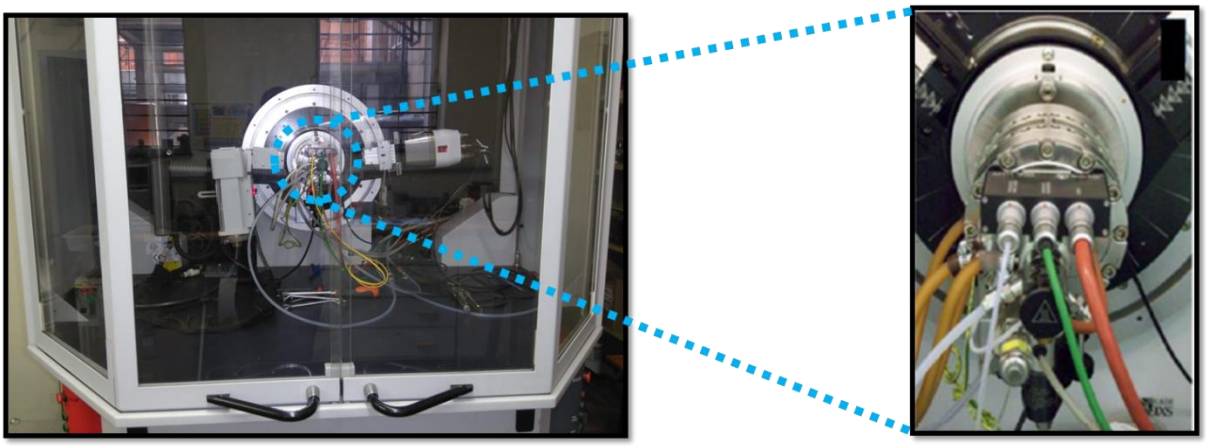


Figure 3.6: Bruker D8 Advance diffractometer fitted with an XRK900.

3.2.5. Thermogravimetric Analysis (TGA)

The determination of the thermal stability and reduction effect of the materials synthesized was carried out using using a PerkinElmer STA6000 analyser (Figure 3.7). The samples were analysed by heating them from 50 to 900 °C at a heating rate of 20 °C/min in an oxidizing atmosphere maintained by flowing air (20 mL/min). The TGA data provided a plot of the loss in sample weight as various components of the sample decomposed as a function of temperature and from the residual weight loss percentages of metal loadings were determined [3].



Figure 3.7: PerkinElmer STA6000 analyser.

3.2.6. Raman Spectroscopy

The structure of the carbon materials was studied using Raman spectroscopy. The data obtained allowed for evaluation of the sp^2 and sp^3 carbon content of the carbon materials contained, from the analysis of the D and G band intensities [4]. Sample analysis was carried out using a Bruker Senterra Raman spectrometer (Figure 3.8).

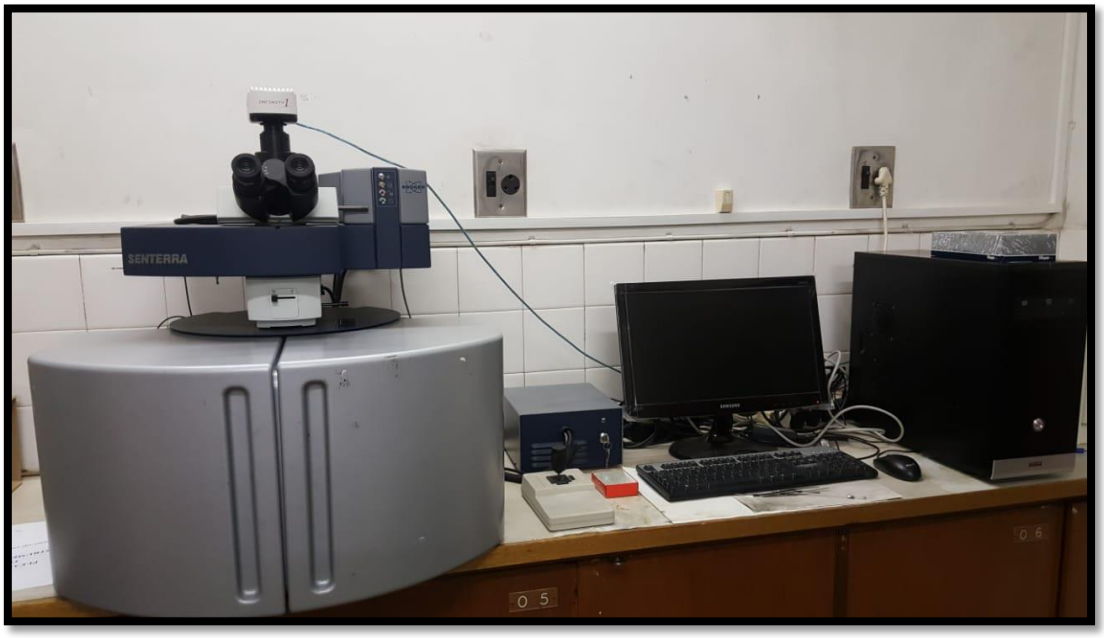


Figure 3.8: Bruker Senterra Raman spectrometer.

3.2.7. Temperature-programmed reduction (TPR)

A Micromeritics AutoChem II instrument (Figure 3.9) fitted with a thermal conductivity detector (TCD) and three Brooks mass-flow controllers was used to generate the TPR profiles. Prior to analysis, 50 mg of the sample to be analysed was outgassed under the flow of He at 150 °C for an hour. Analysis took place, subsequently, by flowing 5%H_2/Ar (20 ml/min) through the sample and at temperatures between 50 and 900 °C (heating rate of 10 °C/min). The TPR profiles provide information on the temperature at which the reducing species begin to be activated to produce a phase transformation [5].



Figure 3.9: Micromeritics AutoChem II instrument.

3.3. Catalyst evaluation (Fischer-Tropsch process)

3.3.1. Gases

All gases used were supplied by African Oxygen (AFROX) Ltd. Certificates containing information on the composition and percentage purity as well as the expiry dates accompanied all the gas cylinders used. All gases were of an ultra-high purity (UHP) grade. Hydrogen, nitrogen, argon, syngas (a mixture of 30% carbon monoxide, 10% nitrogen, balanced with hydrogen), a six gas mixture (a mixture of CH_4 (2.5%), C_2H_4 (0.2%), C_2H_6 (0.5%), CO (10.0%), CO_2 (5.0%) balanced with argon) were used, all with (>99.9%) purity. Hydrogen was used for the reduction/activation of the catalyst prior to FT testing. Nitrogen was used as an internal standard to ensure an accurate mass balance. Argon was used as a carrier gas for the gas chromatographs (GC): flame ionisation detector (FID) and thermal conductivity detector (TCD).

3.3.2. FT rig and catalytic reactor setup

Schematic representations of the FT rig and reactor used for FT testing in this study are shown in Figure 3.10 (a, b). Pressure indicator controllers/regulators were installed in the system to monitor the set pressure of the gases flowing to the GCs and the catalytic reactor. The flow rate of the gases flowing through the reactor was measured using a flow bubble meter. The gas lines were made up of stainless steel and Swagelok fittings were used. The catalytic reactor used is a stainless steel fixed bed reactor which had a wall thickness of 15 mm and contained a frit inside that makes up the catalyst bed. Below the reactor were two knockout pots, the hot trap (kept at 150 °C) from which wax products were collected and the cold trap (ambient temperature) from which liquid products (oil and water) were collected. The gaseous products were collected on-line and are known from the data generated by the TCD and FID.

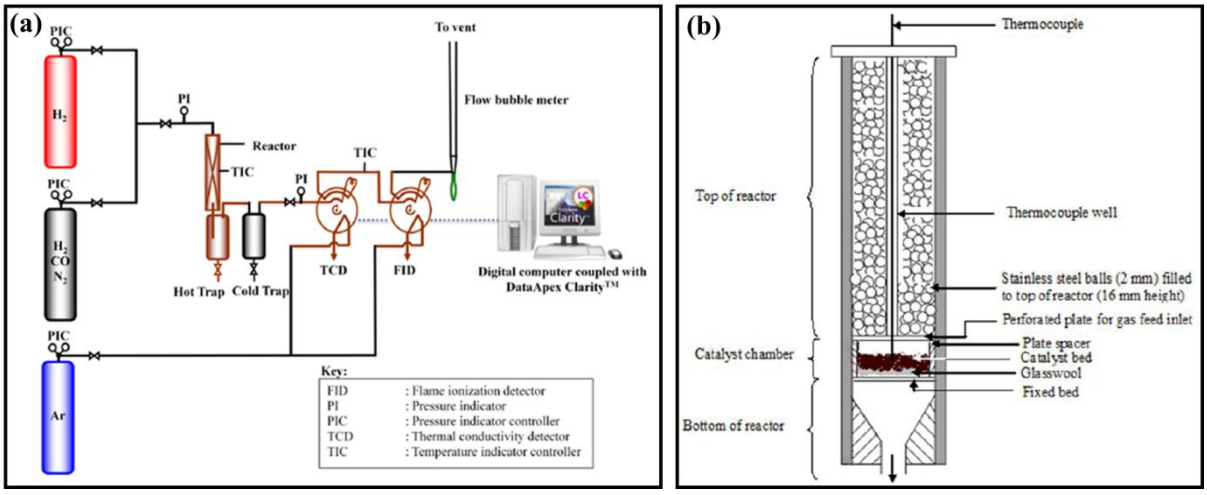


Figure 3.10: Schematic representation of the (a) rig and (b) catalytic reactor.

3.3.3. Experimental setup

A layer of quartz wool was placed on the frit inside the reactor and the catalyst (0.5 g) was added on top of it and another layer quartz wool was placed on top of the catalyst. Steel balls were then placed on the catalyst bed to distribute the feed evenly, and a thermocouple was also placed on the catalyst bed for the regulation of temperature. The catalyst was then reduced/activated *in-situ* under a flow of pure hydrogen (flow rate of 45 ml/min at a pressure of 4 bar), at 350 °C for 16 h, to give the catalyst sufficient time to undergo reduction to its metallic active phase, prior to the FT reaction. For the FT reaction, syngas (flow rate of 20 ml/min) was the gas used, and it was gradually introduced until a pressure of 10 bar was reached. The reaction took place at temperatures of 220 °C and 240 °C for 50 h each.

3.3.4. Calibration of the gas chromatographs and product analysis

Two gases were used for the calibration of the gas chromatographs, namely; syngas and a six gas mixture. Figure 3.11 and Figure 3.12 show the typical GC traces recorded from the TCD and FID during calibration of the gases. The conditions used when operating the GC's are outlined in Table 3.1. The gaseous products were analysed online using the TCD and FID. DataApex Clarity^{TM} software was used to collect the chromatograms from the TCD and the FID.

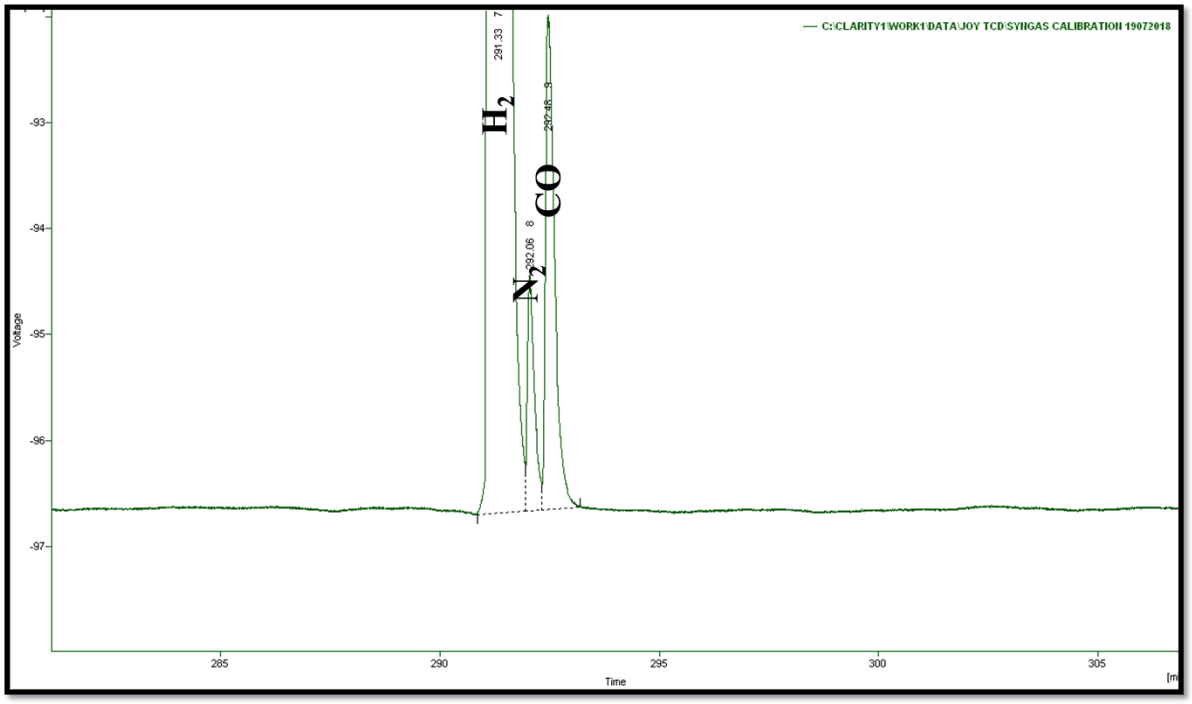


Figure 3.11: TCD-GC trace of syngas.

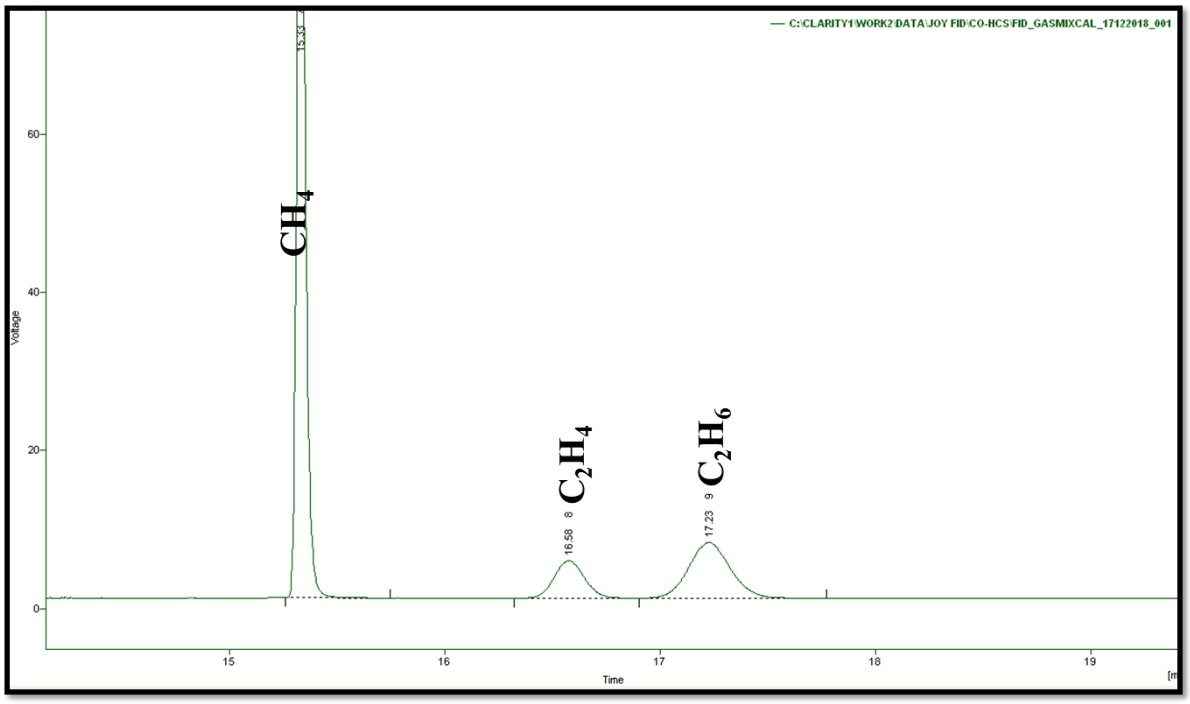


Figure 3.12: FID-GC trace of the calibration gas (six gas mixture).

Table 3.1: A summary of the operating conditions used for the GC's.

Gas Chromatograph (online)	**PYE Unicam (Series 204)**
Detector	TCD, T = 220 °C
Column type	Packed, stainless steel, 2m x 2.2mm, O.D = 1/8"
Stationary phase	Carbosieve S-II, 60-80 mesh
Sample valve temperature	150 °C
Carrier gas	Argon
Flow rate	20 ml (NTP)/min
Oven temperature	250 °C (isothermal)
Product analysis	H_2, N_2, CO,CH_4, CO_2
Gas Chromatograph (online)	**Hewlett Packard 5890**
Detector	FID, T = 220 °C
Column type	Packed, stainless steel, 1.5 m x 2.2 mm, O.D = 1/8"
Stationary phase	ZB-5, 80/100 mesh
Sample valve temperature	150 °C
Carrier gas	Argon
Flow rate	20 ml (NTP)/min
Oven temperature	250 °C (isothermal)
Product analysis	C_1 - C_8
Gas Chromatograph (offline)	**Varian 3700**
Detector	FID, T = 350 °C
Column type	30 m x 5 µFT, O.D.= 0.53 mm
Stationary phase	ZB-1
Sample valve temperature	250 °C
Carrier gas	Air
Flow rate	30 ml (NTP)/min
Oven temperature:	
Oil	Heat to 300 °C at 12.5 °C/min, hold at 300 °C for 30 min
Wax	Heat to 300 °C at 10 °C /min, hold at 300 °C for 240 min
Product analysis	C_5 – C_{35}

3.3.5. Data Analysis: Mass balance calculations

The mass balance calculations used were similar to those used by Nijs *et al.* [6], Everson *et al.* [7], Snavely *et al.* [8], Bahome [9], and Phadi [10]. These calculations were performed on the catalysts under steady state conditions. Table 3.2 outlines all the calculations performed. Table 3.3 contains descriptions of all the symbols used.

Table 3.2: Equations used in product analysis.

Equations	Description of equation
$\%\ CO = \left[\frac{N_{CO,in} - N_{CO,out} \times \text{Gas contraction}}{N_{CO,in}}\right] \times 100$	% CO conversion equation.
$F_{in} = \text{Gas contraction} \times F_{out}$	The feed inlet flow rate to the reactor.
$N_{C,in} = F_{in}.t.X_{CO,in}$	Number of moles of carbon in the feed stream.
$N_{C,out} = \left[\frac{A_c}{A_{c,cal}}\right].X_{c,cal}.F_{out}.t$	Number of moles of product for each of the components present in the gas phase.
$X_{HC,i} = \left[\frac{RF_i.A_{HC,i}}{A_{C_2,cal}}\right].A_{C_2,cal}$	Hydrocarbon mole fractions, hydrocarbon product areas were corrected relative to C_2H_4 (olefins) and C_2H_6 (paraffins).
$S_i = \left[\frac{N_i}{r_{CO}.t}\right] \times 100$	Product selectivity
$r_{FTS} = r_{CO} - r_{CO_2}$	Rate of reaction for FTS
$r_{WGS} = r_{CO_2}$	Rate of reaction for water gas shift WGS
$Olefin\ to\ paraffin\ ratio\ i = \frac{N_i^=}{N_i^= + N^-}$	Olefin to paraffin ratio
$Activity = \frac{r_{FTS}}{m_{Co}}$	FT activity

Table 3.3: Descriptions of all the symbols used.

Symbols	Description of the symbols
$N_{CO,in}$	mole fraction of CO in the inlet stream
$N_{CO,out}$	mole fraction of CO in the outlet stream
Gas contraction	N_{in}/N_{out} (where N_{in} = the moles of nitrogen from bypass and N_{out} = moles of nitrogen during reaction)
F_{in}	the total feed flow rate in mol/s
F_{out}	the reactor exit stream flow rate in mol/s
$N_{C,in}$	moles of carbon in the feed
t	the total mass balance time
$X_{CO,in}$	mole fraction of CO in the feed gas
A_c	the integrated peak area for component c
$A_{c,cal}$	the peak area for the component c in the calibration gas
$X_{c,cal}$	the mole fraction of component c in the calibration gas
RF_i	response factor for carbon number i
$A_{HC,i}$	integrated peak area for a hydrocarbon with carbon number i
$A_{C_2,cal}$	peak area of the C_2 hydrocarbon in the calibration gas
$X_{C_2,cal}$	mole fraction of the C_2 hydrocarbon in the calibration gas
S_i	product selectivity for hydrocarbons
N_i	moles of hydrocarbon containing *i* carbon atoms
r_{CO}	rate of CO conversion
r_{CO_2}	rate of carbon dioxide formation
$N_i^=$	moles of olefin containing *i* carbon atoms
N^-	moles of paraffin containing *i* carbon atoms

3.4. References

[1] E.P. Barrett, L.G. Joyner, P.P. Halenda, The determination of pore volume and area distributions in porous substances. I. Computations from nitrogen isotherms, Journal of the American Chemical society 73 (1951) 373-380.

[2] R.E. Dinnebier, S.J. Billinge, Powder diffraction: theory and practice, Royal Society of Chemistry, 2008.

[3] P. Gabbott, Principles and applications of thermal analysis, John Wiley & Sons, 2008.

[4] A.C. Ferrari, J. Robertson, Interpretation of Raman spectra of disordered and amorphous carbon, Physical review B 61 (2000) 14095.

[5] J.W. Niemantsverdriet, Spectroscopy in catalysis, John Wiley & Sons, 2007.

[6] H. Nijs, P. Jacobs, On-line single run analysis of effluents from a Fischer-Tropsch reactor, Journal of Chromatographic Science 19 (1981) 40-45.

[7] R. Everson, E. Woodburn, A. Kirk, Fischer-Tropsch reaction studies with supported ruthenium catalysts: I. Product distributions at moderate pressures and catalyst deactivation, Journal of Catalysis 53 (1978) 186-197.

[8] K. Snavely, B. Subramaniam, On-Line Gas Chromatographic Analysis of Fischer−Tropsch Synthesis Products Formed in a Supercritical Reaction Medium, Industrial & engineering chemistry research 36 (1997) 4413-4420.

[9] M.C. Bahome, Synthesis and use of carbon nanotubes as a support for the Fischer-Tropsch Synthesis, (2008).

[10] T.T. Phadi, Titanium dioxide-carbon spheres composites for use as supports in cobalt Fischer-Tropsch synthesis, 2013.

Chapter 4: Synthesis of hollow carbon spheres and the use of their void space for encapsulation of metal nanoparticles

4.1. Introduction

Hollow carbon spheres (HCSs) have garnered great research interest owing to their properties such as high surface area, encapsulation ability, and thermal stability. They have been utilized in a wide range of applications including fuel cells [1, 2], catalyst supports [3-5], and lithium-ion batteries [6, 7]. The most widely reported synthesis method of HCSs involves the use of a sacrificial template. Typically, a core-shell spherical structure is synthesized by depositing a layer of carbon on a solid spherical template followed by removal of the core to obtain the HCSs. The hard templating method allows for better control of the spherical morphology and of size of the HCSs, and provides an opportunity to tune the porosity of the carbon shell as opposed to using the soft templating method [3].

Silica as a template for the synthesis of HCSs has received great research attention [8-10]; however, its removal involves the use of harsh reagents such as concentrated acids or bases, after carbonization. Therefore, the use of polymeric materials has been explored, such as polystyrene, which can be removed by thermal decomposition during carbonization. Polystyrene, at 440 °C has completely decomposed [11]. White *et al.* [12] used polystyrene latex as a template and biomass as a carbon source. The polystyrene latex was removed during the carbonization step at a temperature > 500 °C. Tang *et al.* [13] also used polystyrene latex as a template for their HCSs synthesis which was removed during the carbonization of their carbon precursor, glucose.

The carbon source used plays a pivotal role on the physical and chemical properties of the resulting HCSs carbon framework [3, 14, 15]. A uniform carbon coating and carbon yield are of particular importance when it comes to the templating synthesis and they are controlled by several experimental parameters [16]. Su *et al.* [17] reported on the synthesis of HCSs *via* the chemical vapour deposition (CVD) method using benzene as the carbon source and their results showed that the morphology of their HCSs relied on the CVD temperature and

reaction duration. The graphitic nature of the HCSs improved with an increase in the CVD temperature, and a short CVD time resulted in a thin shell. Fang *et al.* [16] synthesized HCSs using resorcinol-formaldehyde (RF) resins. The use of RF resins as a carbon precursor is of particular interest due to the high carbon yield obtained from them [18]. Resorcinol-formaldehyde derived carbons have attracted considerable attention due to their properties such as high surface area, high porosity and, great mechanical and thermal stability [19, 20]. Their synthesis has been reported in the literature [18, 21] to be similar to the Stöber method used to synthesize silica spheres. This can be attributed to the structural similarities between the RF precursor and the silica precursor, which *via* the sol-gel process, can form 3D networks (Figure 4.1) [22] as a result of their tetrahedral coordinate geometry [23].

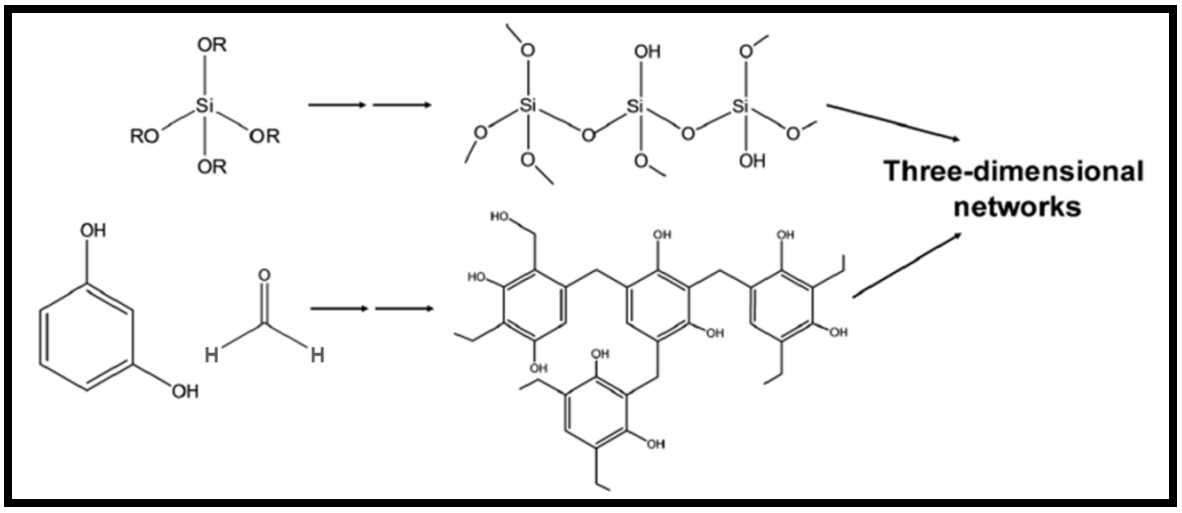


Figure 4.1: The 3D networks formed from the hydrolysis of silica precursors and RF [22].

In addition, silica and RF resins are both synthesized in the presence of a catalyst, either acidic or basic, which initiates the polymerization reaction involved in their synthesis [20]. The synthesis of RF resins, typically, under basic conditions, involves an addition reaction (Figure 4.2) between resorcinol and formaldehyde to form hydroxymethyl derivatives (–CH_2OH) which then undergo a condensation reaction to form methylene (–CH_2–)- and methylene ether (–CH_2–O–CH_2–)-bridged compounds, resulting in a crosslinked structure (Figure 4.3) [19, 24].

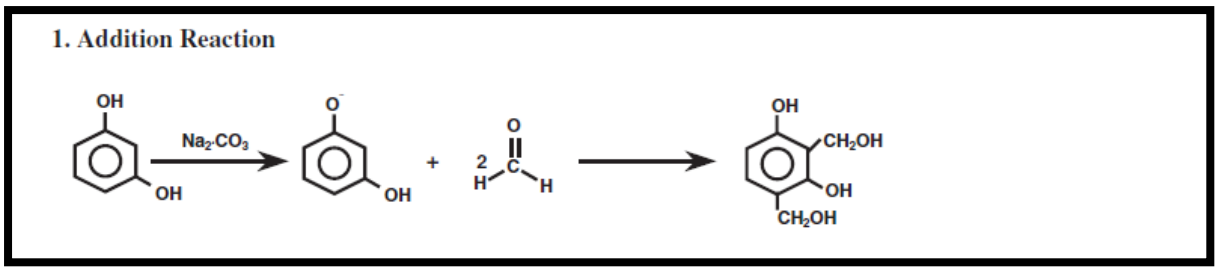


Figure 4.2: Addition reaction between resorcinol and formaldehyde [19].

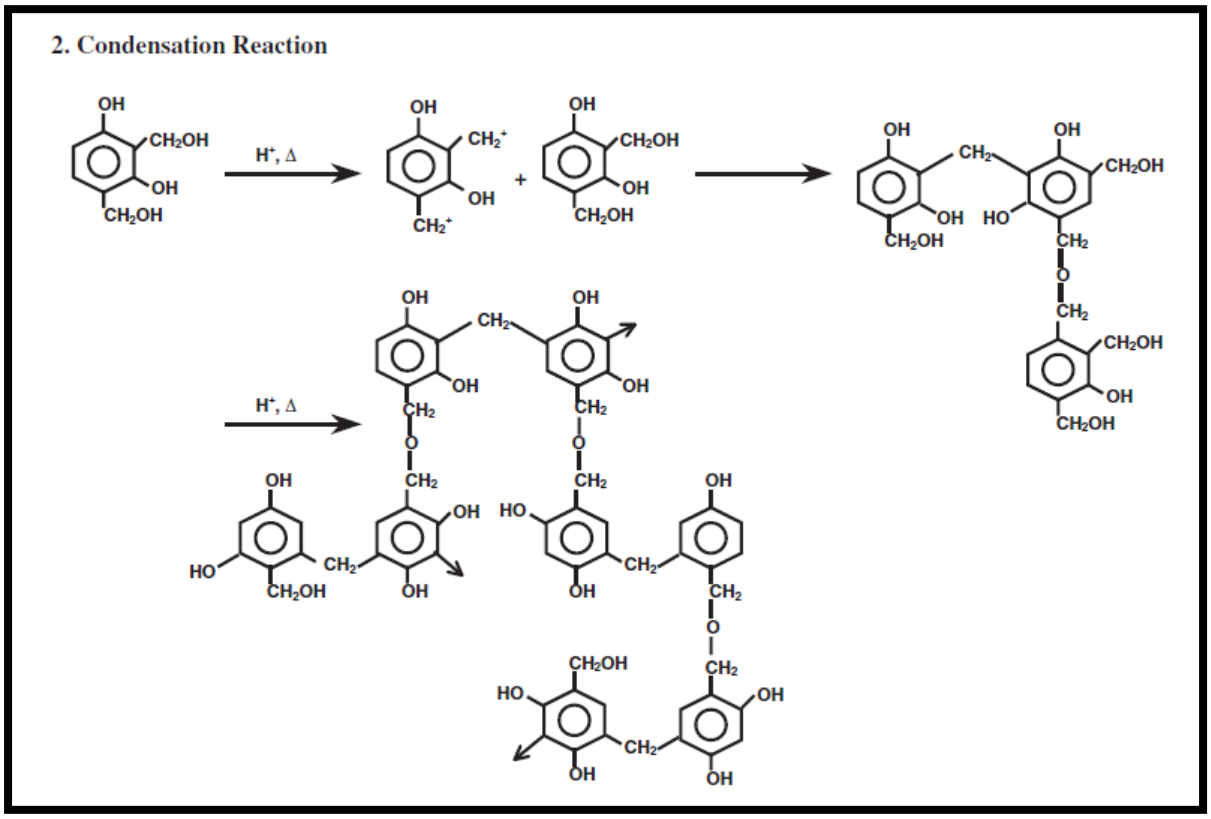


Figure 4.3: Condensation reaction to form a crosslinked structure [19].

The encapsulation of nanomaterials inside hollow spherical nano-structures has attracted great research interest [3, 25-27]. They are usually described as core/yolk-shell or rattle-type nanoarchitectures [28, 29]. The choice of the core and shell is influenced by the desired application. For instance, if it is for drug delivery applications, the core could be magnetic and the shell must be porous [30]. Meanwhile, in catalysis they are particularly advantageous in that they can stabilize the metal nanoparticles (active component) against sintering [27]. Sintering is reported to occur through two main mechanisms: (1) migration, induced by high temperature, which results in the agglomeration of the metal nanoparticles, and (2) Ostwald ripening which involves the growth of nanoparticles [31, 32]. The rate of sintering, for the first mechanism, depends on the rate of migration of the nanoparticles, while that of the

second mechanism depends on the surface properties of the nanoparticles such as their shape, or surface energy. Sintering leads to a reduction in the active sites of the nanoparticles and subsequent overall reduction in the catalytic activity [33].

Consequently, these nanoarchitectures have been applied as nanoreactors [16], particularly when the shell is porous, allowing the diffusion of reactants and products through the shell. For instance, Harada *et al.* [34] encapsulated Pd nanoparticles inside hollow mesoporous carbon spheres (Pd@hmC) to prevent aggregation or coalescence between neighbouring nanoparticles in different spheres. They exploited the void space of the hollow mesoporous carbon spheres for the alcohol oxidation reaction on the Pd nanoparticles' surface sites, which exhibited good catalytic activity. Wang *et al.* [5] used the void space of hollow carbon spheres to encapsulate Pt-Co nanoparticles, PtCo@HCS, for the purpose of stabilizing the nanoparticles against aggregation and for the hydrogenolysis of 5-hydroxymethylfurfural (HMF) to 2,5-dimethylfuran (DMF). The catalyst showed excellent catalytic activity and selectivity towards the desired product, DMF.

Many studies to encapsulate metal nanoparticles inside HCSs have been performed with silica spheres as the template, i.e. depositing metal nanoparticles on the silica spheres before carbonization. For instance, Nongwe *et al.* [35] and Phaahlamohlaka *et al.* [4] encapsulated Pt and Ru nanoparticles, respectively, inside HCSs by depositing the metal nanoparticles on the silica template before carbonization. After carbonization, the removal of the silica template was carried out by using hydrofluoric acid (HF) to obtain the HCSs with the metal nanoparticles encapsulated. However, some metals such as Co may be leached out in the presence of solubilizing acids such as HF during the silica template removal.

Therefore, in this study we have used polystyrene spheres (PSs) as an interesting alternative to silica spheres, as the template, which can be easily removed by thermal decomposition. We have also demonstrated the synthesis of HCSs using RF as a carbon source by coating it on PSs. In earlier studies the coating of RF on spherical materials has mainly been carried out on silica spheres [16, 22, 36]. Indeed many studies to vary the shell thickness of HCSs have been performed with silica spheres as the template. Herein, we report on the use of PSs as a template to study the effect of varying the RF amount and alcohol solvent on the formation of HCSs with different shell thicknesses, and their use for the encapsulation of Co nanoparticles.

4.2. Experimental section

4.2.1. Sources of chemicals and gases

All chemicals used were of analytical grade. Styrene (Aldrich), polyvinylpyrollidone (PVP, MW 40 000, Aldrich), cobalt nitrate hexahydrate (Aldrich), ethylene glycol (Aldrich), ammonia solution (25%, Fluka), potassium persulfate (KPS, Eimer and Amend), hexadecyltrimethylammonium bromide (CTAB, Aldrich), chloroplatinic acid hydrate (Aldrich), hydrazine (50%, Aldrich), ethanol (99%, Merck), 2 – butanol (99%, Merck), isopropanol (99%, Merck). All the chemicals were used the way they were received. Deionised water was used in all the experiments. Ultra high purity (UHP) nitrogen (Afrox) was used for carbonization in the horizontal furnace.

4.2.2. Synthesis of template (polystyrene spheres)

Polystyrene spheres (PSs) were synthesized by adding ethanol (50 ml) and water (200 ml) into a 500 ml round-bottom flask fitted with a condenser and a magnetic stirrer placed inside the flask. A styrene monomer (16 ml) and PVP (0.2 g) were added into the flask and the mixture was allowed to stir for 10 min. To the resulting solution, 0.3 g of potassium persulfate (KPS), dissolved in 20 ml of water, was then added and the solution was stirred for another 10 min. The mixture was then heated in an oil bath to 80 °C and kept at that temperature for 24 h. The resulting product was separated by centrifugation at 18000 rpm for 15 min, washed with ethanol several times, and then dried at 40 °C in an oven overnight. Once dry, it was ground to fine powder.

4.2.3. Synthesis of HCSs

PSs (3 g) were dispersed by sonication in ammonia solution (25%; 2 ml), ethanol (150 ml) and water (50 ml) for 30 min. A mixture of resorcinol (1.13 g), formaldehyde solution (37%; 2 ml), CTAB (1.5 g) and ethanol (50 ml) was sonicated separately, and then added to the PSs. The resulting mixture was then stirred at room temperature for 24 h and then heated to 80 °C in an oil bath for 24 h to polymerize the resorcinol-formaldehyde (RF) polymer on the PSs. The resulting composite, PSs@RF, was then filtered and washed several times with water, followed by drying at 60 °C for 12 h. The removal of PSs and carbonization of RF were performed in a one-step procedure using a horizontal tube furnace. The PSs@RF was placed in a quartz boat inside a quartz tube reactor which was then heated inside the furnace under a N_2 flow (50 ml/min) at 350 °C for 1 h and subsequently at 600 °C for 2 h at a heating rate of 5 °C/min (Figure 4.4). This then resulted in the formation of the HCSs.

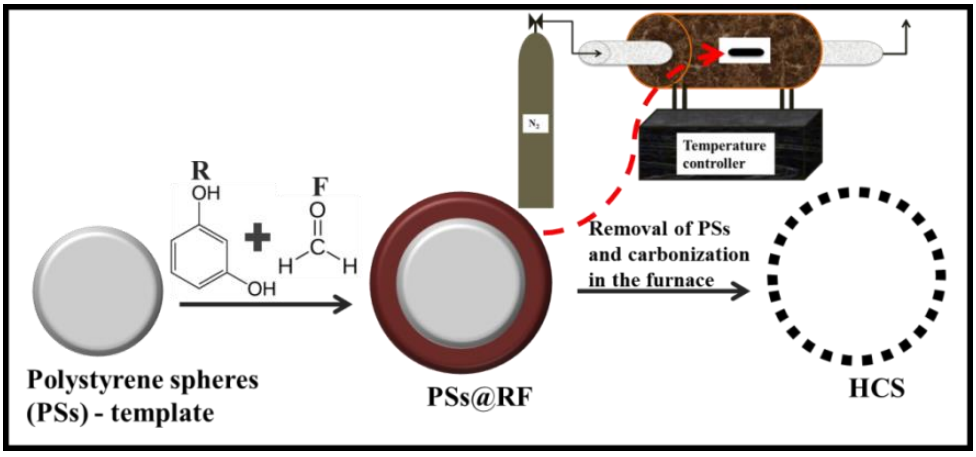


Figure 4.4: Schematic illustration of the synthesis of the HCSs.

4.2.4. Synthesis of HCSs with different shell thicknesses

The RF resins have controllable structural parameters which allows for the tailoring of the shell thickness of the RF and subsequent carbon shell [16]. The synthesis parameters used to tune the shell thicknesses of the HCSs are included in Table 4.1. They were synthesized using the method described in section 4.2.3 but this time by adjusting the amount of RF used. Li *et al.* [37] reported on varying the shell thickness of the HCSs by using RF as the carbon source and silica as the template. They observed that by simply varying the RF amount, shell thicknesses from 5 – 45 nm could be achieved. The R to F ratio was maintained at 2. Similarly, in our method, using the PSs synthesized using the method described in section 4.2.2 as the template, the amount of RF coated on them was increased while maintaining the RF ratio as 2 (Table 4.1). This is the ratio commonly used in the literature [19, 24]. Additionally, in place of ethanol; isopropanol and 2-butanol were used to see their effect on the size of the HCSs.

Table 4.1: Synthesis parameters for HCSs with different shell thicknesses.

Sample	PSs (g)	NH_3 (ml)	C_2H_5OH (ml)	H_2O (ml)	CTAB (g)	Resorcinol (g)	Formaldehyde (ml)
HCS-A	3	2	150	50	1.5	1.13	2.28
HCS-B	3	2	150	50	1.5	2.10	4.20
HCS-C	3	2	150	50	1.5	3.90	7.80

4.2.5. Synthesis of Co@HCS

The various steps followed in synthesizing Co-encapsulated HCSs (Co@HCS) are outlined in this section.

4.2.5.1. Loading of 10% Co on PSs (Co/PSs)

PSs (3 g) were dispersed by sonication for 30 min in a water-ethanol solution, (75 and 25 ml, respectively). To this, cobalt nitrate hexahydrate (0.445 g) was added, resulting in a pink milky solution. Reduction of Co nanoparticles was then performed by slow addition of a solution of hydrazine (10 ml, 2 M) resulting in a blue milky solution. The solution was then left to stir for 12 h to allow for complete reduction of Co and deposition onto the PSs. The resulting Co/PSs were collected by filtration and washed several times with water. The Co/PSs composite was then placed in an oven to dry for 12 h at 40 °C.

4.2.5.2. Synthesis of Co@HCS

Co/PSs (3 g) were dispersed by sonication in ammonia solution (25%; 2 ml), ethanol (150 ml) and water (50 ml) for 30 min. A mixture of resorcinol (1.13 g), formaldehyde solution (37%; 2 ml), CTAB (1.5 g) and ethanol (50 ml) was sonicated separately, and then added to the Co/PSs. The resulting mixture was then stirred at room temperature for 24 h and then heated to 80 °C in an oil bath for 24 h to polymerize the resorcinol-formaldehyde (RF) polymer on Co/PSs. The resulting composite, Co/PSs@RF, was then filtered and washed several times with water, followed by drying at 60 °C for 12 h. The removal of PSs and carbonization of RF were performed in a one-step procedure using a horizontal tube furnace. The Co/PSs@RF was placed in a quartz boat inside a quartz tube reactor which was then heated inside the furnace under a N_2 flow (50 ml/min) at 350 °C for 1 h and subsequently at 600 °C for 2 h at a heating rate of 5 °C/min. This then resulted in the formation of Co@HCS.

4.2.5.3. Synthesis of Co@HCS with different shell thicknesses

The Co@HCS with different shell thicknesses, i.e. 50 and 80 nm were synthesized following the method outlined in section 4.2.4. However, the amount of RF was varied following the synthesis parameters outlined in table 4.2, below.

Table 4.2: A summary of the synthesis parameters used for the Co@HCS samples with different shell thicknesses.

Sample	Co/PSs (g)	NH_3 (ml)	C_2H_5OH (ml)	H_2O (ml)	CTAB (g)	Resorcinol (g)	Formaldehyde (ml)
Co@HCS-50	3	2	150	50	1.5	2.10	4.20
Co@HCS-80	3	2	150	50	1.5	4.52	9.04

4.2.5.4. Synthesis of Co@HCS using different alcohols

A similar synthetic procedure to that outlined in section 4.2.5.2 was followed. In place of ethanol as the alcohol in the alcohol-water solvent used for the synthesis of RF resins, isopropanol and 2-butanol were used.

4.2.6. Results and discussion

In this section, the material characterization techniques outlined in chapter 3 which were used and the results obtained thereof, will be discussed.

4.2.6.1. Characterization of the template, polystyrene spheres (PSs)

The PSs were characterized using SEM and TEM analysis (shown in Figure 4.5 a and b, respectively) to confirm their morphology. The SEM and TEM images show that the PSs were spherical in morphology with a uniform distribution and had a smooth surface. The particle size distribution was from 400 – 480 nm with an average particle size of 445 nm (shown in Figure 4.5 c). The thermal analysis of the PSs was performed using TGA and from the TG/DTG profile (shown in Figure 4.6) it can be observed that the PSs decompose at 400 °C.

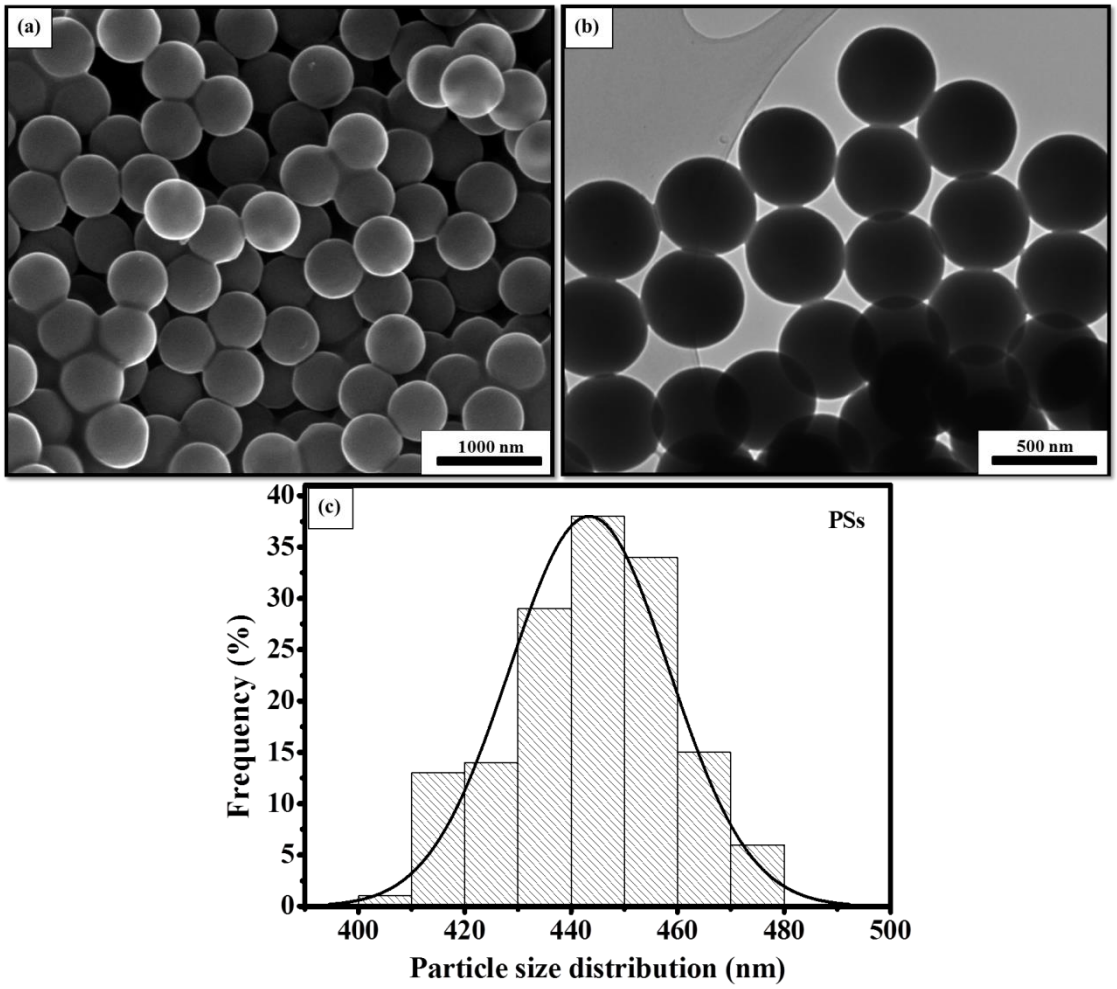


Figure 4.5: a) SEM image b) TEM image and c) particle size distribution for PSs.

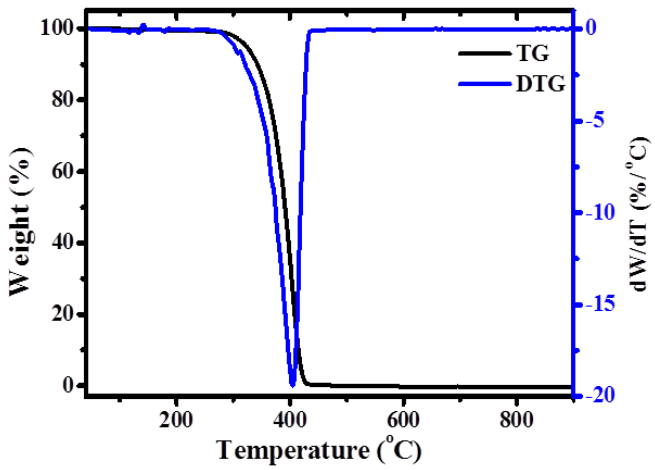


Figure 4.6: TG/DTG profile for PSs.

4.2.6.2. Characterization of HCSs

The uniform size and monodispersed polystyrene spheres (PSs), (Figure 4.5) synthesized were coated with a carbon precursor, resorcinol-formaldehyde (RF). The use of the RF polymer as a carbon precursor to coat a template has been reported, especially using silica as a template [16, 37]. The ease with which RF is coated onto the template can be attributed to the addition of a cationic surfactant, CTAB. Most of the templates used such as silica and polystyrene have negative surface charges which results in a lack of nucleation of the negatively charged RF polymer onto their surfaces, due to a repulsive force between the surface charges [37].

Therefore, by adding the cationic CTAB, the template surface becomes less negatively charged which then promotes the nucleation of RF on the template of the surface. A study on this was conducted by Li *et al.* [37] who used zeta-potential measurements to confirm that the charge of the SiO_2 template becomes less negative as CTAB is added to it and when the concentration of CTAB is increased, the charge becomes more positive. They then showed the effect of the increase in the concentration of CTAB on the core-shell RF-coated SiO_2 (SiO_2@RF). The graph eventually plateaus meaning that a complete and uniform coating of the silica with RF was achieved. In addition, CTAB also has the ability to create pores [38].

To obtain the HCSs the core was removed. This was achieved during the carbonization of the core-shell composite when RF was coated onto the PSs template (PSs@RF), first at 350 °C for 1 h to begin the removal of the PSs then at 600 °C for 2 h, for the carbonization of the RF polymer. The cross-linked nature of the RF polymer allows for its carbonization with ease. The resulting HCSs were characterized using SEM and TEM to confirm their spherical and hollow morphology (Figure 4.7). The SEM image shows some broken spheres exposing the hollow morphology (Figure 4.7 a). The broken spheres can be attributed to a pressure buildup inside the spheres when the template decomposes during carbonization [12, 39]. The SEM image (Figure 4.7 a) also shows that the surface of the HCSs is rough and not smooth like that of PSs (Figure 4.5 a). This can be attributed to the resulting porous carbon from the carbonization of RF.

The TEM image (Figure 4.7 b) also shows the spherical morphology and hollow core of the HCSs which shows that the template (PSs) was removed. The HCSs consist of a uniform carbon layer ~30 nm. The particle size distribution (Figure 4.7 c) of the HCSs is between 340 – 440 nm with an average particle size of 385 nm. This is less than that of the template, PSs,

due to a shrinkage that occurs during carbonization [39]. This can be ascribed to the dehydration of the crosslinked carbon precursor that occurs during carbonization [36, 40]. HCSs with a BET surface area of 416 m^2/g, pore volume of 0.39 cm^3/g, and pore size of 3.8 nm. The TG curves (Figure 4.8) show that the thermal stability of the HCSs is higher (550 °C) than that of the PSs (400 °C) after carbonization, which shows that the PSs were removed. The TGA data also gave information on the carbon structure of the HCSs. The onset decomposition temperature of the HCSs was at ca. 400 °C which is associated with non-graphitized carbon typical of the carbon structures produced from RF-derived carbon [41].

The PXRD pattern (Figure 4.9 a) for the HCSs shows two weak and broad peaks that correspond to the (002) and (100) diffraction modes at $2\theta = 22.0^{o}$ and 43.4^{o} which are characteristic of a non-graphitized, amorphous carbon structure [13, 42]. Figure 4.9 b shows the Raman spectrum of the HCSs. The two peaks at 1339 cm^{-1} and 1589 cm^{-1} represent the D band and G band of carbon, respectively. The presence of the D and G bands shows that the carbon material consists of sp^2 carbon atoms [43]. The D band represents the defects in the crystal structure of carbon while the G band represents the hexagonal graphitic structure of carbon [42]. The I_D/I_G ratio was 1.4 which confirmed that the carbon material was highly defective [43, 44].

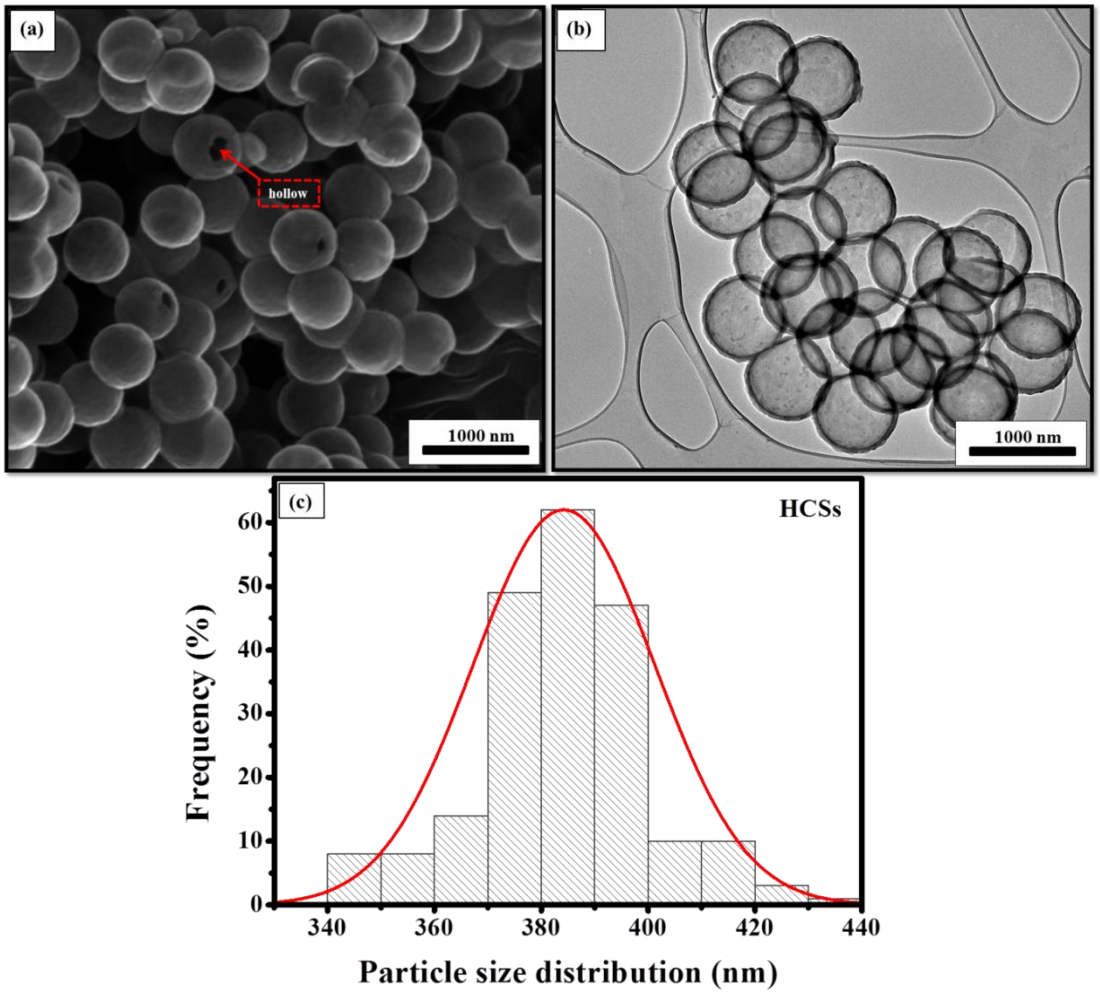


Figure 4.7: a) SEM image, b) TEM image and c) particle size distribution for HCSs.

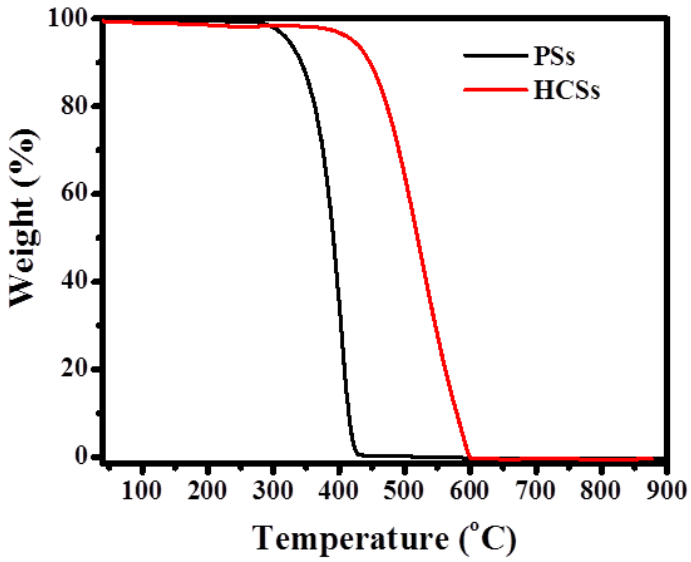


Figure 4.8: TG curves of PSs and HCSs.

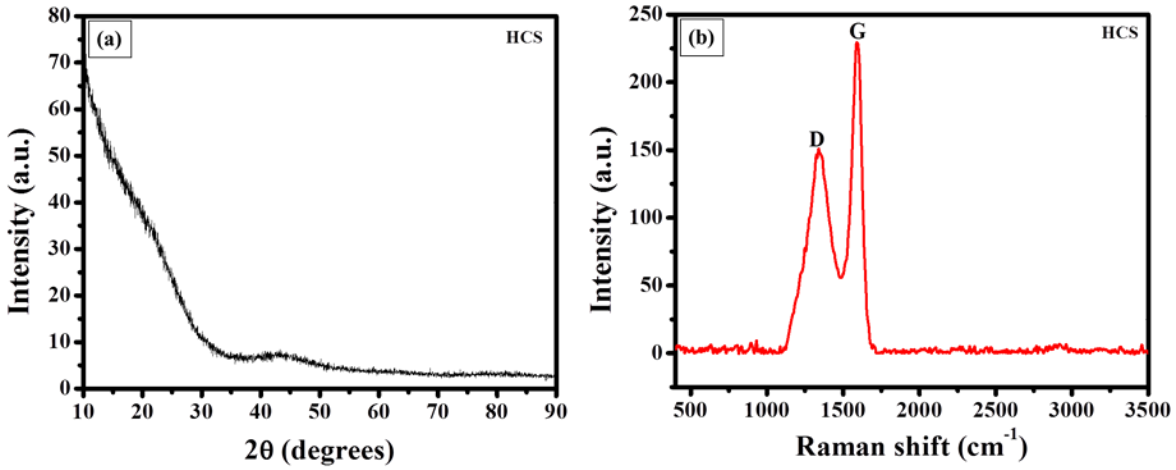


Figure 4.9: a) PXRD pattern, and b) Raman spectrum for the HCSs.

4.2.6.3. Characterization of HCSs with different shell thicknesses

The ability to tailor the RF shell thickness and subsequent carbon shell, by varying the synthetic parameters, was demonstrated by Fang *et al.* [16], who like Li *et al.* [37] (reported in section 4.2.4), were able to tailor the shell thickness from 3 – 40 nm by varying the amount of RF while keeping other synthetic parameters the same. The shell thickness, in a similar manner, was varied by varying the RF amount while keeping other synthetic parameters the same (Table 4.1). TEM images shown in Figure 4.10 display HCSs with different shell thicknesses following the synthesis parameters outlined in Table 4.1. The TEM images (Figure 4.10) show the spherical and hollow morphology of the HCSs as well as the differences in the shell thickness. The size of the shell thickness is included in Table 4.3. For HCS-A (Figure 4.10 a) the shell thickness is ~30 nm, for HCS-B (Figure 4.10 b) the shell thickness is ~50 nm and for HCS-C the shell thickness is ~70 nm. These shell thicknesses were achieved by doubling the RF amount while keeping the R to F ratio as 2.

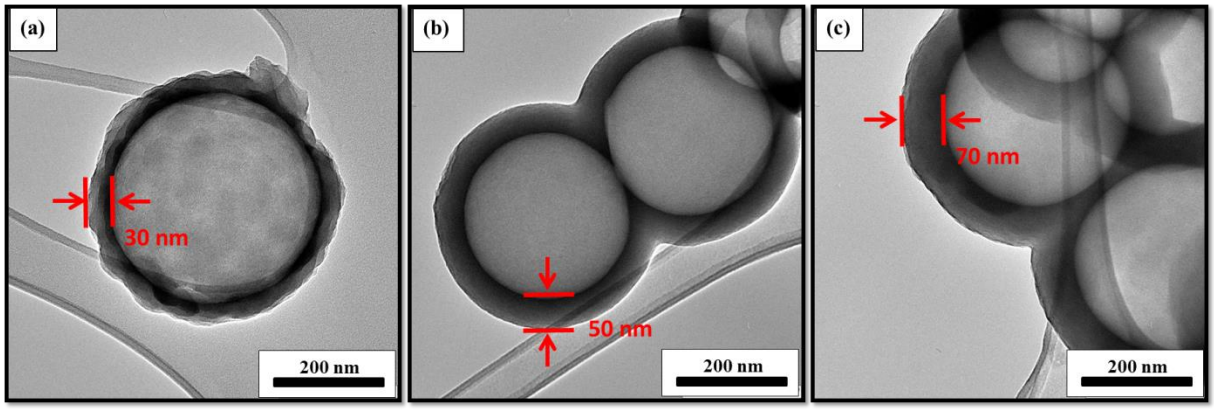


Figure 4.10: TEM images of (a) HCS-A, (b) HCS-B, and (c) HCS-C.

Table 4.3: Shell thickness and textural properties of the HCSs with different shell thicknesses.

Sample	Shell thickness (nm)	BET surface area m^2/g	Microporous surface area m^2/g	Pore volume cm^3/g	Pore size /nm
HCS – A	~30	416	274	0.39	3.8
HCS – B	~50	472	362	0.33	2.8
HCS – C	~70	476	385	0.31	2.6

Table 4.2 also shows a summary of the BET surface area, pore volume and pore sizes of the HCSs. There was an increase in the BET surface area as the shell thickness increased. The values of the pore sizes show that the HCSs had some mesopores, since according to the IUPAC definition of mesopores, any material with pore sizes 2 – 50 nm are considered mesoporous. As the carbon shell grew, the pore volume and size slightly decreased due to some blocking of the pore channels as the carbon content increases.

The nitrogen adsorption-desorption isotherms of the HCSs are similar and are of type I/IV isotherms (Figure 4.11), which reveals their microporous and mesoporous nature, but predominantly the microporous nature. The high specific surface areas (416 – 476 m^2/g) are due to the microporous areas which account for more than half of the total surface areas of the HCSs (Table 4.2). To further confirm the microporosity of the HCSs, pore size

distribution graphs (Figure 4.11) were plotted used which displayed that the highest nitrogen adsorption was at pore sizes less than 2 nm. These can be attributed to the decomposition of RF and loss of small molecules during carbonization [42].

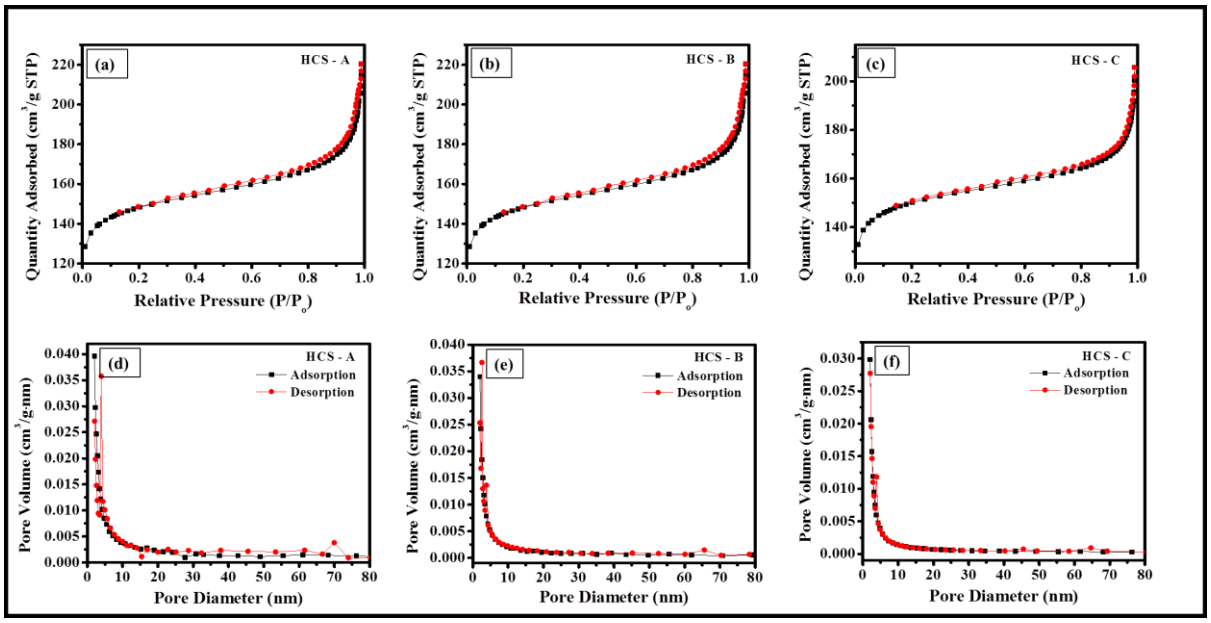


Figure 4.11: (a, b, c) Nitrogen adsorption-desorption isotherms and (d, e, f) pore size distribution graphs of HCS-A, HCS-B, and HCS-C.

Additionally, the shell thickness of the HCSs was varied by changing the alcohol used in the reaction. In place of ethanol; isopropanol and 2-butanol were used. Liu *et al.* [18] synthesized solid carbon spheres of different sizes by changing the alcohol in the alcohol/water mixture used to synthesize RF resins. They found that the particle size of the carbon spheres increased with an increase in the alkyl chain of the alcohol. They reported data on methanol, ethanol, and isopropanol. Figure 4.12 (a, b, c), below, shows the TEM images of HCS synthesized using ethanol (HCS – ethanol), isopropanol (HCS – isopropanol) and 2-butanol (HCS – 2-butanol), respectively. Similar results to those reported by Liu *et al.* [18] were observed. The shell thickness increased with an increase in the alkyl chain of the alcohol. HCS – ethanol had a shell thickness of ~30 nm, HCS – isopropanol ~40 nm and HCS – 2-butanol ~60 nm. When using 2-butanol in the alcohol-water mixture, the resulting carbon shell, although thicker, was not uniformly spherical (Figure 4.12 c, inset), and there were also aggregates formed (Figure 4.12 c).

A study was also conducted by Yoo and Stein [45] on the effect of the alcoholic solvent on the SiO_2 spheres using ethanol, isopropanol and butanol. They observed that after the

hydrothermal treatment of the SiO_2 spheres, the SiO_2 spheres made using ethanol had a smooth surface while those made using isopropanol and butanol had rough surfaces. The effect of the alcoholic solvent on the final morphology of the spheres obtained was attributed to its effect on the extent of the SiO_2 condensation. A study on the influence of the alcohol used on the condensation rates and the size of the spheres was carried out by Stöber and co-workers [46]. They discovered that the condensation rates were fastest when using methanol and slowest when using n-butanol, and there was an inverse relationship between the rates and the sizes of the spheres. As mentioned earlier, the method used for RF resin synthesis is similar to the Stöber method used in the synthesis of SiO_2 spheres [18, 21] and what is observed to influence the size of the SiO_2 spheres also influences the size of the RF resins and the corresponding carbon sphere or carbon shell in the case of HCSs synthesis.

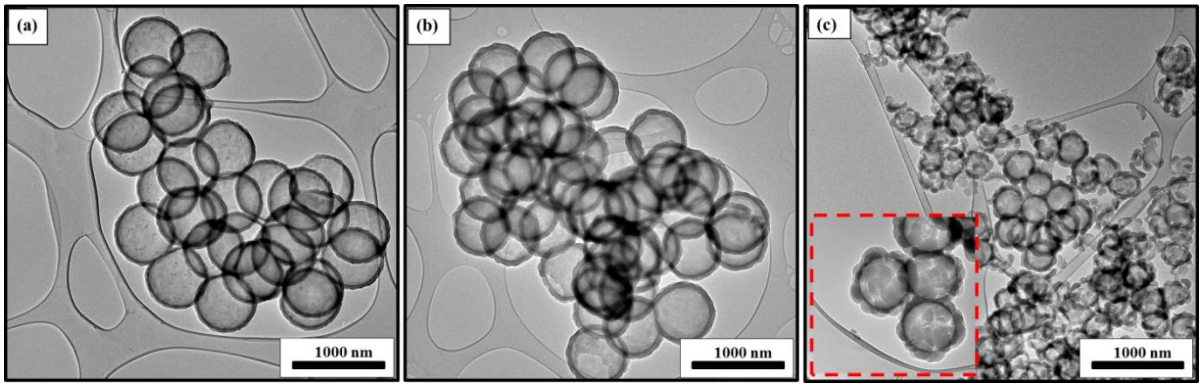


Figure 4.12: TEM images of (a) HCS – ethanol, (b) HCS – isopropanol, and (c) HCS – 2-butanol.

4.2.6.4 Characterization of Co@HCS

The Co nanoparticles encapsulated inside the HCSs (Co@HCS) were observed from TEM studies. Figure 4.13 (a) shows that initially, there was sintering of the Co nanoparticles when a heating rate of 10 °C/min was used during the template removal and subsequent carbonization of the Co/PSs@RF composite. The Co dispersion and size were improved when the heating rate was reduced to 5 °C/min (Figure 4.13 b). The average size of the Co nanoparticles determined by TEM was 16.9 $\pm$ 6.9 nm for Co@HCS formed using a heating rate of 10 °C/min during the carbonization step (Figure 4.14 a) and 5.5 $\pm$1.0 nm for Co@HCS formed using a heating rate of 5 °C/min during the carbonization step (Figure 4.14 b). The shell thickness of the Co@HCS was 30 nm which was in agreement with the shell thickness of the HCSs reported in section 4.2.6.2 since the same method of producing the carbon shell was followed. The Co@HCS sample formed using the slower heating rate of 5

°C/min was further studied using PXRD and TGA, and was used to compare with other samples in the next sections.

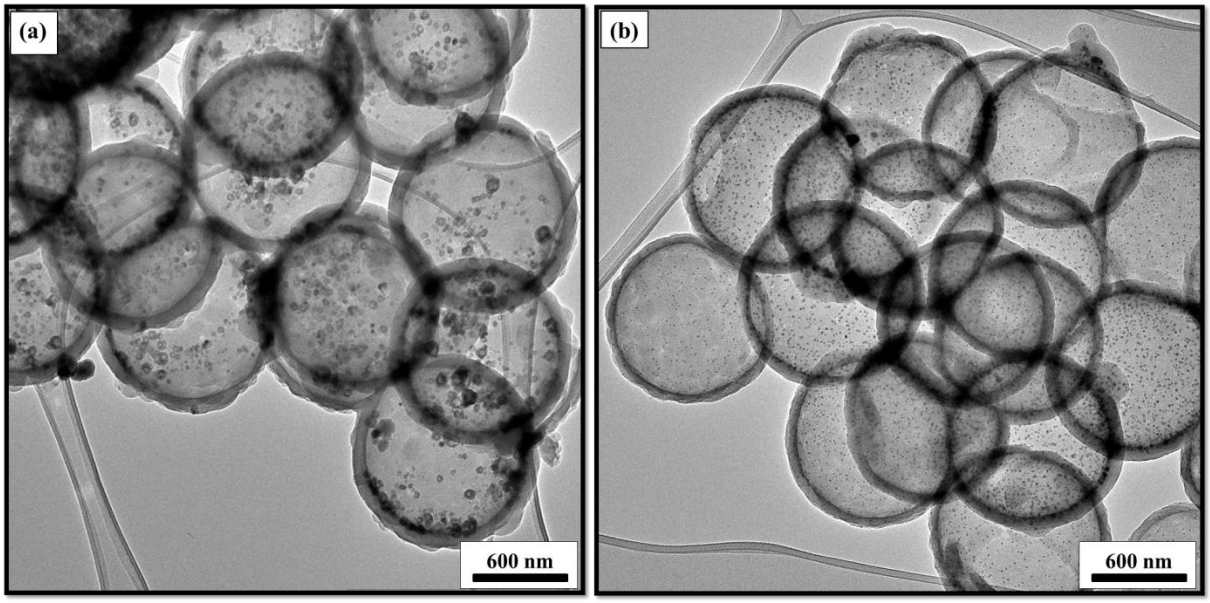


Figure 4.13: (a) Sintered Co nanoparticles in Co@HCS, (b) dispersed Co nanoparticles in Co@HCS.

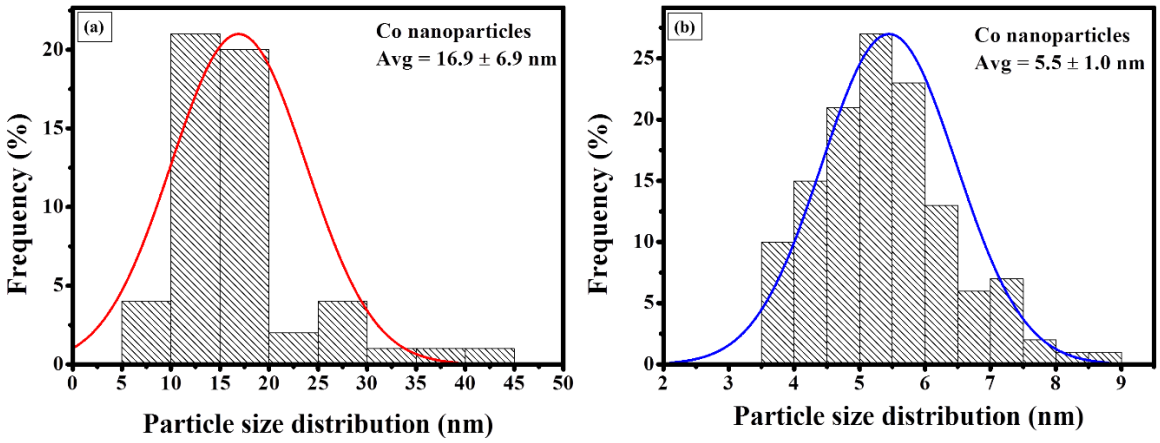


Figure 4.14: Particle size distribution for (a) Sintered Co nanoparticles in Co@HCS, (b) dispersed Co nanoparticles in Co@HCS.

The PXRD pattern for Co@HCS, below, (Figure 4.15 a) shows a weak and broad hump that corresponds to the (002) diffraction at 2θ = 22.5° because of the defective, non-graphitic nature of the carbon material synthesized. The distinct peak showing at 2θ = 52° corresponded to the Co_3O_4 phase of the encapsulated nanoparticles which is due to the oxidation of Co nanoparticles during the carbonization step and from storage of the Co@HCS

material. The TGA profiles (Figure 4.15 b) show the HCSs without the metal nanoparticles, and the Co encapsulated HCSs (Co@HCS). The decomposition of the HCSs was discussed in section 4.2.6.2 to be that of non-graphitic carbon with an onset decomposition temperature of 500 °C, however when the Co nanoparticles are loaded inside of the HCSs the onset decomposition temperature is even lower at 300°C. The decrease in the thermal stability of carbon in the presence of Co nanoparticles results from the ability of the metal nanoparticles to catalyze the oxidation of carbon [47, 48]. The HCS had no residual weight but the Co@HCS did, which allowed for the estimation of the percentage loading of Co_3O_4 found to be 10%. This was the targeted percentage loading.

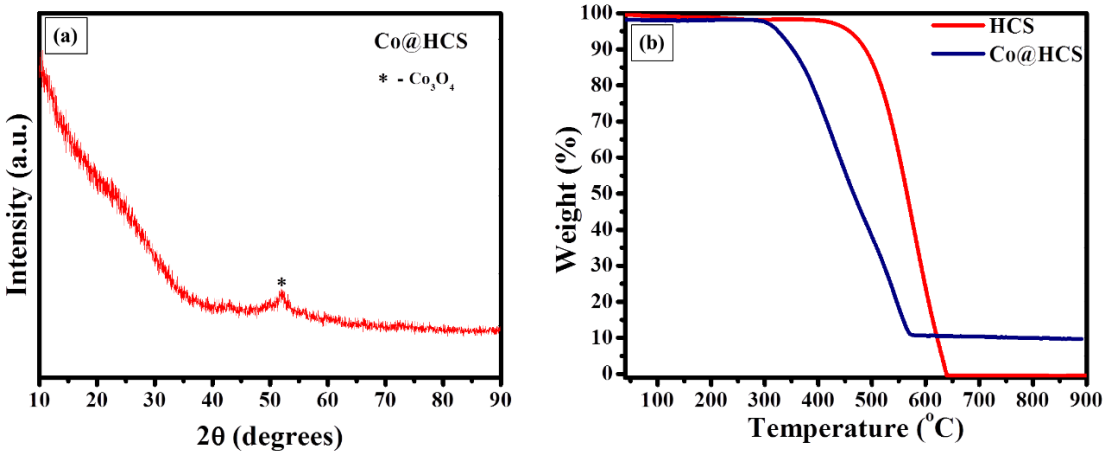


Figure 4.15: (a) PXRD pattern for Co@HCS and (b) TGA profiles of HCS and Co@HCS.

4.2.6.5. Characterization of Co@HCS with different shell thicknesses

The Co@HCS samples were synthesized with different shell thicknesses; 50 nm (Co@HCS-50), and 70 nm (Co@HCS-70). The samples were characterized using TEM. Figure 4.16 (a and b) shows the TEM images of Co@HCS-50 at different magnifications. The carbon shell had a thickness of ~50 nm and the Co nanoparticles were well dispersed with an average particle size of 7.0 ± 1.3 nm. This was greater than the average particle size reported for Co@HCS with a shell thickness of ~30 nm, reported in section 4.2.6.4.

The TEM image for Co@HCS-80 (Figure 4.17 a) displays the thick carbon shell which is ~80 nm and the Co nanoparticles with an average particle size of 19.1 ± 3.6 nm (Figure 4.17 b), which are even larger. The increase in the size of the encapsulated metal nanoparticles with an increase in the RF amount and the corresponding carbon shell was as a result of the growth mechanism of the RF shell with an increase in the amount of RF. The nanoparticles

increased in size with increased amounts of RF; this will require further investigation. In addition, formation of a carbon nanotube (CNT) was observed in the Co@HCS-80 sample which is encircled on the inset (Figure 4.17 a). Co nanoparticles have been widely used for the formation of CNTs. Their use can be attributed to their ability to decompose gaseous carbonaceous molecules and their high carbon solubility [49].

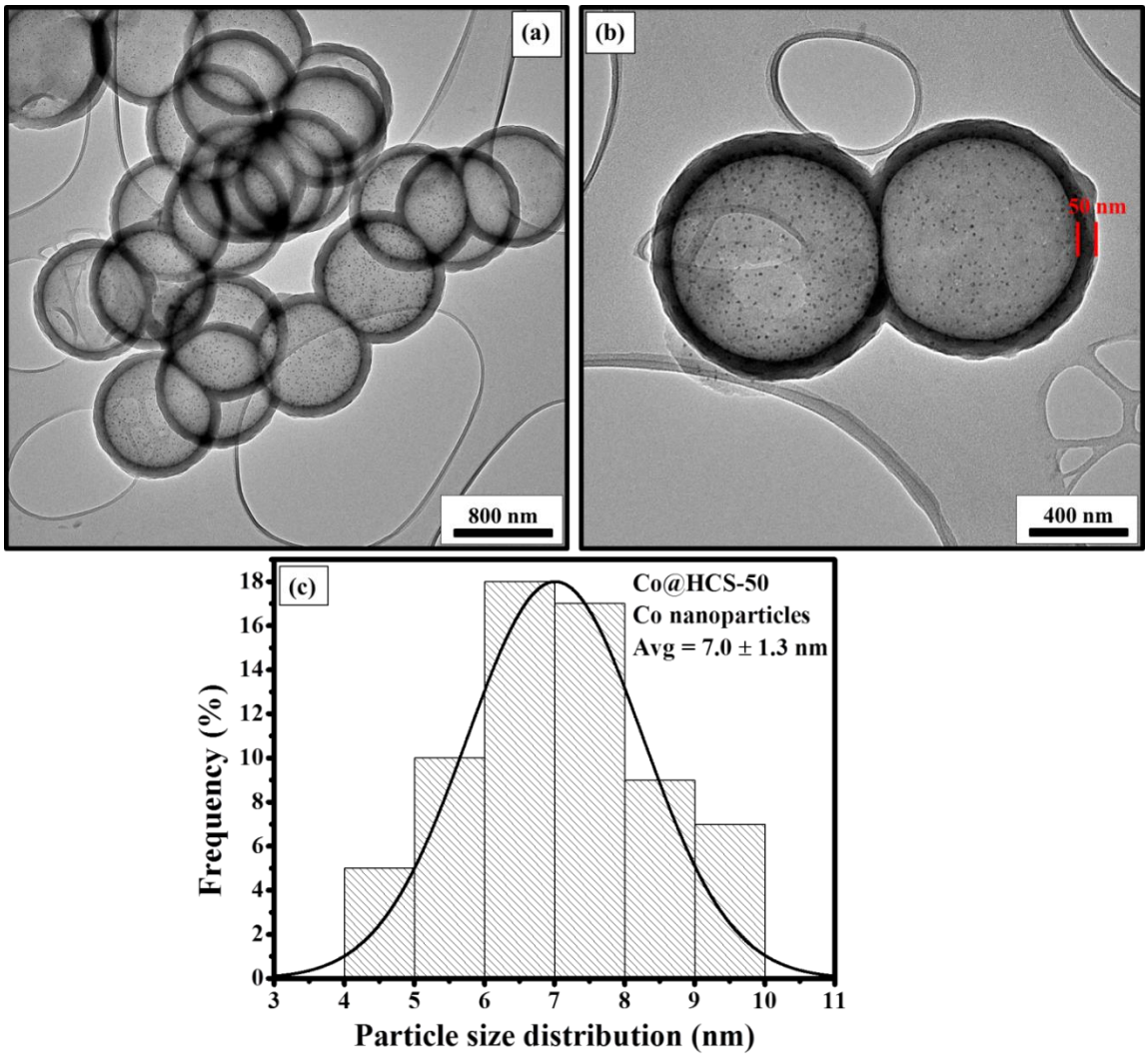


Figure 4.16: (a, b) TEM images at different magnifications, and (c) particle size distribution of Co@HCS-50.

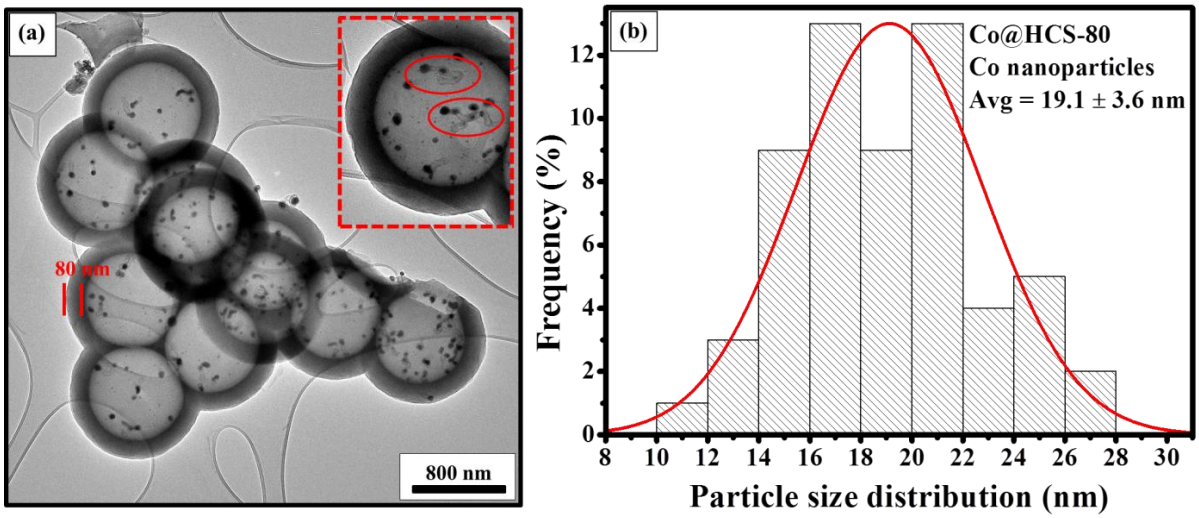


Figure 4.17: (a) TEM image and (b) particle size distribution of Co@HCS-80.

4.2.6.6. Characterization of Co@HCS using different alcohols

The Co@HCS samples were synthesized using ethanol (EtOH), isopropanol (iPROH), and 2-butanol (2-BuOH). The TEM images (Figure 4.18) revealed the morphologies of the Co@HCS samples, while Co@HCS-EtOH had a spherical and smooth shell which was ~30 nm in thickness, Co@HCS-iPROH and Co@HCS-2-BuOH had shells with rough surfaces which were ~40 nm and ~60 nm, respectively, in thickness. It was again observed that 2-BuOH used as a co-solvent in the synthesis of HCSs does not form HCSs with uniform shells as was observed in section 4.2.6.3. The encapsulated Co nanoparticles had narrow particle size distributions with average particle sizes of 5.5±1.0 nm for Co@HCS-EtOH, 5.3 ± 0.7 nm for Co@HCS-iPrOH and 5.9 ± 0.7 nm for Co@HCS-2-BuOH.

The textural properties of the samples are outlined in Table 4.4, below. The pore sizes of all three samples, Co@HCS-EtOH, Co@HCS-iPrOH, and Co@HCS-2-BuOH show that all samples had mesopores. The BET specific surface area for Co@HCS-EtOH and Co@HCS-2-BuOH were high, but the pore volume of Co@HCS-2-BuOH was much lower which could be attributed to its thicker and non-uniform shell. Co@HCS-iPrOH, however, had a significantly lower surface area and pore volume, likely resulting from the solvent effect. This was observed by Yoo and Stein [45] on their SiO_2 spheres synthesized using these solvents, after their hydrothermal treatment.

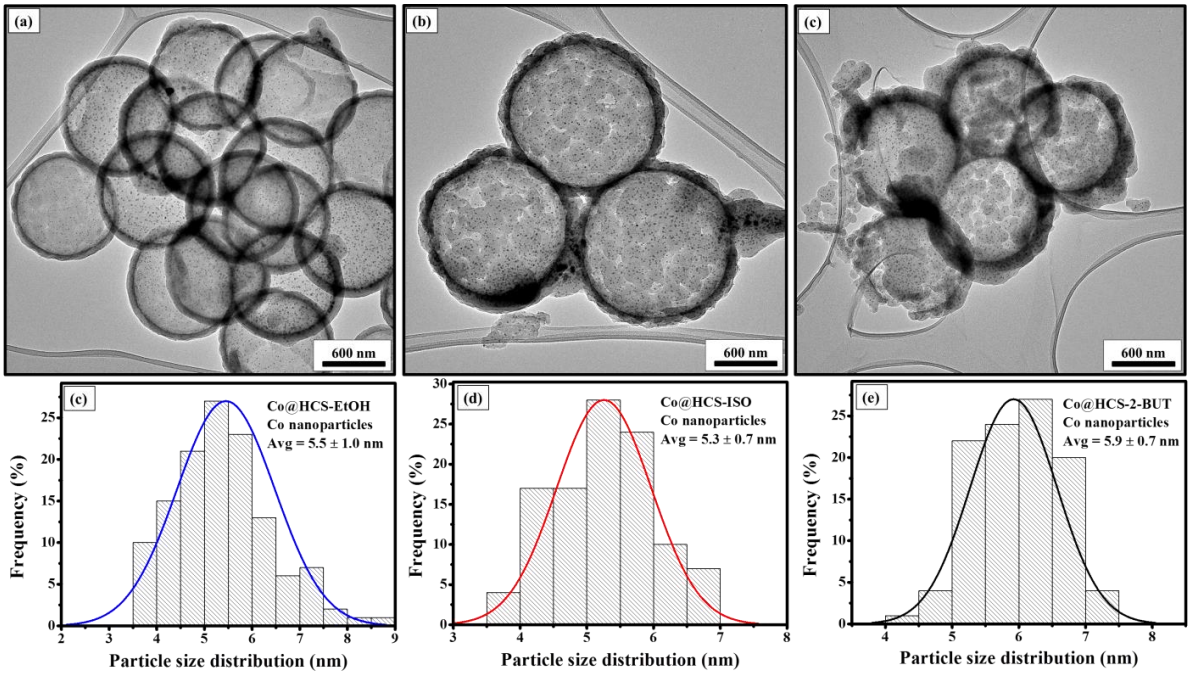


Figure 4.18: TEM image and particle size distribution graph of (a, c) Co@HCS-EtOH, (b. d) Co@HCS-iPrOH, and (c, e) Co@HCS-2-BuOH, respectively.

Table 4.4: Textural properties of the Co@HCS samples synthesized using different alcohols.

Sample	BET surface area m^2/g	Pore volume cm^3/g	Pore size /nm
Co@HCS-EtOH	486	0.47	4.0
Co@HCS-iPrOH	249	0.19	3.0
Co@HCS-2-BuOH	434	0.27	2.5

Furthermore, TGA was used to study the thermal stability of the samples by monitoing the temperature at which the carbon support present in all the samples gets oxidised to CO_2 in air. The onset decomposition temperatures (Figure 4.19) of Co@HCS-2-BuOH and Co@HCS-iPrOH were at 282 °C while that of Co@HCS-EtOH was at 300 °C. The overall decomposition of Co@HCS-EtOH was higher than that of the other samples, making it the most thermally stable of the three samples. The residual weight percentages observed on the TGA profiles can be attributed to the presence of Co in the samples. Although the same amount of the Co precursor was used to achieve a metal loading of 10%, this was achieved

with the Co@HCS-EtOH sample. The Co@HCS-iPrOH sample had an even higher residual weight percent of 16% and the Co@HCS-2-BuOH had the lowest residual weight percent of 7%. The differences may be as a result of the influence on the metal-to-carbon ratio possibly influenced by the carbon content present in each sample and pore volume of the carbon support.

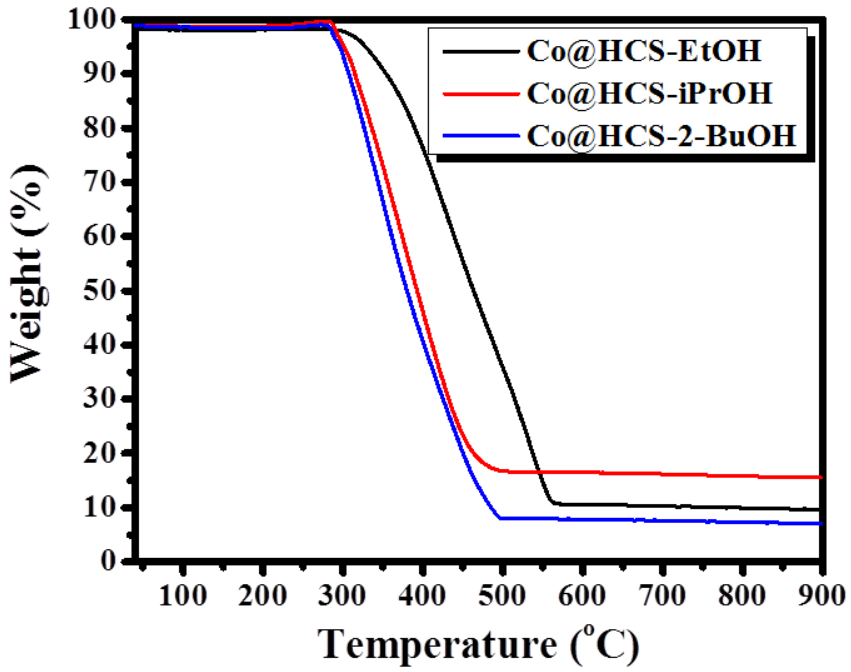


Figure 4.19: TGA profiles of Co@HCS-EtOH, Co@HCS-iPrOH and Co@HCS-2-BuOH.

4.3. Conclusion

The synthesis of the HCSs, demonstrating the effective use of PSs as a template and RF as a carbon precursor, was carried out successfully. No harsh reagents such as HF or concentrated NaOH were used for template-removal as would have been the case if silica was used. Template-removal, i.e. decomposition of the polystyrene spheres which occurs at ca. 400 °C as confirmed by the TG/DTG profile, occurred during the carbonization step in which a temperature of 600 °C was used. The spherical morphology of the sacrificial template, PSs, and the spherical and hollow morphology of the desired HCSs were achieved and revealed using SEM and TEM techniques. The nature of the carbon shell which made the HCSs was confirmed to be non-graphitic by TGA, XRD and Raman techniques. The shell thickness of the HCSs was successfully varied. This was achieved by manipulating the carbon precursor, RF. It was shown that by increasing the amount of RF, the RF shell increased which in turn

resulted in an increased carbon shell, after it was carbonized. Another way to increase the shell thickness that was demonstrated, was by changing the alcohol in the alcohol-water mixture used in the RF resin synthesis. The longer the carbon chain length of the alcohol, the thicker the resulting shell thickness of the HCSs. This was observed for the short chain alcohols using ethanol, isopropanol and 2-butanol. The longer the alkyl chain length of the alcohol, the less polar the alcohol and the less miscible it becomes with water, resulting in RF resins that are non-spherical, non-uniform and aggregated. This was observed with 2-butanol. TEM images of the HCS – 2-butanol sample did show that the shell was thicker.

In addition, the encapsulation ability of the HCSs was demonstrated by loading Co nanoparticles inside the HCSs. The advantage of using PSs as a template for Co nanoparticles encapsulation inside HCSs was demonstrated in that there was no dissolution of Co expected as would be the case if SiO_2 was used and had to be removed using HF. The Co nanoparticles were loaded inside the HCSs with good dispersion which involved slow deposition of the nanoparticles on the template and a slow heating rate (5 °C/min) and a slow flow rate of gas (50 ml/min) during template removal and carbonization to avoid agglomeration of the encapsulated nanoparticles. The effect of the thickness of the carbon shell by increasing the amount of RF used and the effect of the resulting carbon material by using different alcoholic solvents on the Co nanoparticles encapsulated inside the HCSs was investigated.

The size of the Co nanoparticles increased with an increase in the carbon shell. The Co@HCS sample with the thickest shell (~80 nm), had agglomerated Co nanoparticles encapsulated inside, some of which formed some carbon nanotubes. However, the alcoholic solvent used during the synthesis of the carbon shell encapsulating the Co nanoparticles did not have such a significant effect on the size of the Co nanoparticles but rather had an effect on the thermal stability and the Co percentage loading of the samples as observed from the TGA profiles of the samples. The Co@HCS-EtOH sample was the most thermally stable and Co@HCS-iPrOH had the highest Co percentage. The Co@HCS-EtOH did however have the targeted Co percentage loading of 10%. This sample was used as a catalyst and the studies undertaken will be described in the next chapter.

4.4 References

[1] Z. Wen, Q. Wang, Q. Zhang, J. Li, Hollow carbon spheres with wide size distribution as anode catalyst support for direct methanol fuel cells, Electrochemistry communications 9 (2007) 1867-1872.

[2] F.P. Hu, Z. Wang, Y. Li, C. Li, X. Zhang, P.K. Shen, Improved performance of Pd electrocatalyst supported on ultrahigh surface area hollow carbon spheres for direct alcohol fuel cells, Journal of Power Sources 177 (2008) 61-66.

[3] R. Liu, S.M. Mahurin, C. Li, R.R. Unocic, J.C. Idrobo, H. Gao, S.J. Pennycook, S. Dai, Dopamine as a carbon source: the controlled synthesis of hollow carbon spheres and yolk-structured carbon nanocomposites, Angewandte Chemie International Edition 50 (2011) 6799-6802.

[4] T.N. Phaahlamohlaka, D.O. Kumi, M.W. Dlamini, L.L. Jewell, N.J. Coville, Ruthenium nanoparticles encapsulated inside porous hollow carbon spheres: A novel catalyst for Fischer–Tropsch synthesis, Catalysis Today 275 (2016) 76-83.

[5] G.-H. Wang, J. Hilgert, F.H. Richter, F. Wang, H.-J. Bongard, B. Spliethoff, C. Weidenthaler, F. Schüth, Platinum–cobalt bimetallic nanoparticles in hollow carbon nanospheres for hydrogenolysis of 5-hydroxymethylfurfural, Nature materials 13 (2014) 293.

[6] W.M. Zhang, J.S. Hu, Y.G. Guo, S.F. Zheng, L.S. Zhong, W.G. Song, L.J. Wan, Tin-nanoparticles encapsulated in elastic hollow carbon spheres for high-performance anode material in lithium-Ion batteries, Advanced Materials 20 (2008) 1160-1165.

[7] S. Yang, X. Feng, L. Zhi, Q. Cao, J. Maier, K. Müllen, Nanographene-constructed hollow carbon spheres and their favorable electroactivity with respect to lithium storage, Advanced Materials 22 (2010) 838-842.

[8] S.B. Yoon, K. Sohn, J.Y. Kim, C.H. Shin, J.S. Yu, T. Hyeon, Fabrication of carbon capsules with hollow macroporous core/mesoporous shell structures, Advanced Materials 14 (2002) 19-21.

[9] Y. Xia, Z. Yang, R. Mokaya, Mesostructured hollow spheres of graphitic N-doped carbon nanocast from spherical mesoporous silica, The Journal of Physical Chemistry B 108 (2004) 19293-19298.

[10] Y. Xia, R. Mokaya, Ordered mesoporous carbon hollow spheres nanocast using mesoporous silica *via* chemical vapor deposition, Advanced materials 16 (2004) 886-891.

[11] E.-C. Chen, Y.-W. Lin, T.-M. Wu, Fabrication, morphology and thermal degradation behaviors of conductive polyaniline coated monodispersed polystyrene particles, Polymer Degradation and Stability 94 (2009) 550-557.

[12] R.J. White, K. Tauer, M. Antonietti, M.-M. Titirici, Functional hollow carbon nanospheres by latex templating, Journal of the American Chemical Society 132 (2010) 17360-17363.

[13] K. Tang, L. Fu, R.J. White, L. Yu, M.M. Titirici, M. Antonietti, J. Maier, Hollow carbon nanospheres with superior rate capability for sodium-based batteries, Advanced Energy Materials 2 (2012) 873-877.

[14] M. Kruk, B. Dufour, E.B. Celer, T. Kowalewski, M. Jaroniec, K. Matyjaszewski, Synthesis of mesoporous carbons using ordered and disordered mesoporous silica templates and polyacrylonitrile as carbon precursor, The Journal of Physical Chemistry B 109 (2005) 9216-9225.

[15] Y. Zhai, Y. Dou, D. Zhao, P.F. Fulvio, R.T. Mayes, S. Dai, Carbon materials for chemical capacitive energy storage, Advanced materials 23 (2011) 4828-4850.

[16] X. Fang, S. Liu, J. Zang, C. Xu, M.-S. Zheng, Q.-F. Dong, D. Sun, N. Zheng, Precisely controlled resorcinol–formaldehyde resin coating for fabricating core–shell, hollow, and yolk–shell carbon nanostructures, Nanoscale 5 (2013) 6908-6916.

[17] F. Su, X. Zhao, Y. Wang, L. Wang, J.Y. Lee, Hollow carbon spheres with a controllable shell structure, Journal of materials chemistry 16 (2006) 4413-4419.

[18] J. Liu, S.Z. Qiao, H. Liu, J. Chen, A. Orpe, D. Zhao, G.Q. Lu, Extension of the Stöber method to the preparation of monodisperse resorcinol–formaldehyde resin polymer and carbon spheres, Angewandte Chemie 123 (2011) 6069-6073.

[19] S.A. Al-Muhtaseb, J.A. Ritter, Preparation and properties of resorcinol–formaldehyde organic and carbon gels, Advanced materials 15 (2003) 101-114.

[20] A.M. ElKhatat, S.A. Al-Muhtaseb, Advances in tailoring resorcinol-formaldehyde organic and carbon gels, Advanced materials 23 (2011) 2887-2903.

[21] C.J. Brinker, G.W. Scherer, Sol-gel science: the physics and chemistry of sol-gel processing, Academic press, 2013.

[22] X. Li, S. Bai, Z. Zhu, J. Sun, X. Jin, X. Wu, J. Liu, Hollow carbon spheres with abundant micropores for enhanced CO2 adsorption, Langmuir 33 (2017) 1248-1255.

[23] V.G. Pol, L.K. Shrestha, K. Ariga, Tunable, functional carbon spheres derived from rapid synthesis of resorcinol-formaldehyde resins, ACS applied materials & interfaces 6 (2014) 10649-10655.

[24] R. Pekala, Organic aerogels from the polycondensation of resorcinol with formaldehyde, Journal of materials science 24 (1989) 3221-3227.

[25] J. Lee, J.C. Park, H. Song, A nanoreactor framework of a Au@ SiO2 yolk/shell structure for catalytic reduction of p-nitrophenol, Advanced Materials 20 (2008) 1523-1528.

[26] I. Lee, J.B. Joo, Y. Yin, F. Zaera, A yolk@ shell nanoarchitecture for Au/TiO2 catalysts, Angewandte Chemie International Edition 50 (2011) 10208-10211.

[27] P.M. Arnal, M. Comotti, F. Schüth, High-temperature-stable catalysts by hollow sphere encapsulation, Angewandte Chemie International Edition 45 (2006) 8224-8227.

[28] K. Kamata, Y. Lu, Y. Xia, Synthesis and characterization of monodispersed core− shell spherical colloids with movable cores, Journal of the American Chemical Society 125 (2003) 2384-2385.

[29] M. Kim, K. Sohn, H.B. Na, T. Hyeon, Synthesis of nanorattles composed of gold nanoparticles encapsulated in mesoporous carbon and polymer shells, Nano Letters 2 (2002) 1383-1387.

[30] J. Liu, S.Z. Qiao, J.S. Chen, X.W.D. Lou, X. Xing, G.Q.M. Lu, Yolk/shell nanoparticles: new platforms for nanoreactors, drug delivery and lithium-ion batteries, Chemical Communications 47 (2011) 12578-12591.

[31] Z. Li, Z. Wang, S. Kawi, Sintering and Coke Resistant Core/Yolk Shell Catalyst for Hydrocarbon Reforming, ChemCatChem (2019).

[32] E.D. Goodman, J.A. Schwalbe, M. Cargnello, Mechanistic understanding and the rational design of sinter-resistant heterogeneous catalysts, ACS Catalysis 7 (2017) 7156-7173.

[33] J. Lu, B. Fu, M.C. Kung, G. Xiao, J.W. Elam, H.H. Kung, P.C. Stair, Coking-and sintering-resistant palladium catalysts achieved through atomic layer deposition, Science 335 (2012) 1205-1208.

[34] T. Harada, S. Ikeda, F. Hashimoto, T. Sakata, K. Ikeue, T. Torimoto, M. Matsumura, Catalytic activity and regeneration property of a Pd nanoparticle encapsulated in a hollow porous carbon sphere for aerobic alcohol oxidation, Langmuir 26 (2010) 17720-17725.

[35] I. Nongwe, V. Ravat, R. Meijboom, N.J. Coville, Pt supported nitrogen doped hollow carbon spheres for the catalysed reduction of cinnamaldehyde, Applied Catalysis A: General 517 (2016) 30-38.

[36] X. Fang, J. Zang, X. Wang, M.-S. Zheng, N. Zheng, A multiple coating route to hollow carbon spheres with foam-like shells and their applications in supercapacitor and confined catalysis, Journal of Materials Chemistry A 2 (2014) 6191-6197.

[37] N. Li, Q. Zhang, J. Liu, J. Joo, A. Lee, Y. Gan, Y. Yin, Sol–gel coating of inorganic nanostructures with resorcinol–formaldehyde resin, Chemical Communications 49 (2013) 5135-5137.

[38] D. Li, C. Feng, H. kun Liu, Z. Guo, Hollow carbon spheres with encapsulated germanium as an anode material for lithium ion batteries, Journal of Materials Chemistry A 3 (2015) 978-981.

[39] S. Li, A. Pasc, V. Fierro, A. Celzard, Hollow carbon spheres, synthesis and applications–a review, Journal of Materials Chemistry A 4 (2016) 12686-12713.

[40] M. Zheng, J. Cao, X. Chang, J. Wang, J. Liu, X. Ma, Preparation of oxide hollow spheres by colloidal carbon spheres, Materials Letters 60 (2006) 2991-2993.

[41] W. Kukułka, K. Wenelska, M. Baca, X. Chen, E. Mijowska, From Hollow to Solid Carbon Spheres: Time-Dependent Facile Synthesis, Nanomaterials 8 (2018) 861.

[42] X. Ma, L. Gan, M. Liu, P.K. Tripathi, Y. Zhao, Z. Xu, D. Zhu, L. Chen, Mesoporous size controllable carbon microspheres and their electrochemical performances for supercapacitor electrodes, Journal of Materials Chemistry A 2 (2014) 8407-8415.

[43] A. Ferrari, J. Robertson, Resonant Raman spectroscopy of disordered, amorphous, and diamondlike carbon, Physical Review B 64 (2001) 075414.

[44] A.C. Ferrari, J. Robertson, Interpretation of Raman spectra of disordered and amorphous carbon, Physical review B 61 (2000) 14095.

[45] W.C. Yoo, A. Stein, Solvent effects on morphologies of mesoporous silica spheres prepared by pseudomorphic transformations, Chemistry of Materials 23 (2011) 1761-1767.

[46] W. Stöber, A. Fink, E. Bohn, Controlled growth of monodisperse silica spheres in the micron size range, Journal of colloid and interface science 26 (1968) 62-69.

[47] M.W. Dlamini, D.O. Kumi, T.N. Phaahlamohlaka, A.S. Lyadov, D.G. Billing, L.L. Jewell, N.J. Coville, Carbon spheres prepared by hydrothermal synthesis—a support for bimetallic iron cobalt Fischer–Tropsch catalysts, ChemCatChem 7 (2015) 3000-3011.

[48] M. Moyo, M.A. Motchelaho, H. Xiong, L.L. Jewell, N.J. Coville, Promotion of Co/carbon sphere Fischer–Tropsch catalysts by residual K and Mn from carbon oxidation by KMnO4, Applied Catalysis A: General 413 (2012) 223-229.

[49] A. Moisala, A.G. Nasibulin, E.I. Kauppinen, The role of metal nanoparticles in the catalytic production of single-walled carbon nanotubes—a review, Journal of Physics: condensed matter 15 (2003) S3011.

Chapter 5: Hydrogen spillover studies and the effect of spillover on the FT process

5.1 Introduction

The Fischer-Tropsch (FT) process is the catalytic conversion of synthesis gas (syngas, a mixture of carbon monoxide and hydrogen) to fuels and a wide range of chemicals [1-6]. It continues to be an important process studied in academia and industry since its development in the 1920s by Franz Fischer and Hans Tropsch [7, 8]. It is viewed as a promising alternative method to produce cleaner (low sulphur and aromatics content) fuels at a more economically friendly cost, in comparison to those derived from crude oil [8, 9]. Co and Fe catalysts have been utilized since FT was developed and have been used industrially. In comparison to Co catalysts, Fe catalysts are more flexible in terms of temperatures and pressures used in FT synthesis. They exhibit lower methane selectivity, and unlike Co catalysts Fe catalysts exhibit a higher activity towards the water-gas-shift (WGS) reaction and therefore they operate at low H_2/CO ratios for the syngas (derived from coal or biomass) conversion [9]. However, Fe catalysts are not as resistant to deactivation as Co catalysts [1, 9]. In addition, even though Co catalysts are more expensive than Fe catalysts, they generally have a high activity, a high selectivity to long chain hydrocarbons and a low WGS activity [3, 10].

The FT performance (i.e. activity/selectivity) of supported Co catalysts is influenced by the number of the Co active sites available. Therefore, understanding the structural parameters of the catalyst is of paramount importance [11]. One of these parameters is the support on which the Co catalyst is dispersed, whose properties such as pore size, pore volume and surface area, affect the Co dispersion and reducibility. For instance, it has been widely reported that the number of active sites can be improved by supporting the Co particles on a high surface area support such as Al_2O_3 or SiO_2 [11, 12]. However, the limitation of using these supports is that they exhibit strong metal support interactions with the Co species supported on them, resulting in the formation of difficult to reduce compounds which impede the reduction of Co oxide [6, 13, 14]. To circumvent this, carbon supports have been used and have garnered great research interest as Co supports. This in part is due to their relative chemical inertness

which allows for the study of the intrinsic properties of the metal nanoparticles supported on them [1, 6]. For instance, activated carbon (AC) was amongst the first carbon materials to be used as a Co FT catalyst support. It has properties such as high thermal stability, and resistance to corrosion by acidic or basic media [15]. However, because of its microporous structure, there were reactant and product transport limitations, and this led to a selectivity to short chain hydrocarbons [16]. Therefore, a mesoporous carbon support is more ideal for use as a Co FT catalyst support due to the reduced mass transport limitations and enhanced long hydrocarbon selectivity [1]. As a result, carbon supports with tuneable porosity such as carbon nanotubes (CNTs) [17], carbon nanofibers (CNFs) [6], carbon spheres (CSs) [18] and more recently hollow carbon spheres (HCSs) [19] have been used as Co FT catalyst supports.

Another parameter that contributes towards an improvement in the Co FT catalyst performance is the incorporation of a promoter. Generally, noble metal promoters are added to Co catalysts supported on Al_2O_3 or SiO_2 to facilitate Co reduction at lower temperatures [8, 20-22]. In spite of the strong metal support interactions, the dispersion of the Co nanoparticles improves the number of the Co active sites available for the FT reaction [9]. Usually, only a small amount of the promoter is added which usually does not affect the mechanical properties of the Co catalyst.

Schanke *et al.* [23], observed, a significant enhancement in the reduction of Co oxide after co-impregnation of SiO_2 and Al_2O_3 with $Co(NO_3)_2{\cdot}6H_2O$ and $Pt(NH_3)_4(NO_3)_2$. This in turn had an effect on the Co FT catalytic performance by causing an increase in the CO conversions at steady state conditions. They [23] reported CO conversions that were 3 – 5 times greater for their Co-supported catalysts in the presence of Pt as a promoter. In other studies, Chu *et al.* [22] reported CO conversions that were 8 times greater using a Pt promoter.

The noble metal promoters have been reported to catalyse the reduction of Co oxide such that it occurs at lower temperatures *via* a hydrogen spillover mechanism. These promoters are able to catalyse the reduction of cobalt oxide because they become reduced to their metallic state at lower temperatures than Co oxide reduction [21, 24]. In their metallic state, promoters are able to dissociatively adsorb H_2. The highly mobile H atoms formed then subsequently spill over either directly to the Co oxide when they are in intimate contact, or spill over onto the support, migrate through the surface of the support and eventually spill over to the Co oxide. Water is produced in both cases when the Co oxide, (Co_3O_4 or CoO) is reduced to Co^0

by H_2 [24] (Figure 5.1). When the noble metal is in direct contact with the Co oxide, the process is referred to as the primary hydrogen spillover mechanism and when they are separated by the support, it is referred to as the secondary hydrogen spillover mechanism. Hilmen at al., using Re as a promoter for Co/Al_2O_3 [21], and Nabaho *et al.* [25] using Pt as a promoter for Co/Al_2O_3 demonstrated that the noble metal and the Co oxide do not necessarily have to be in contact for the noble metal to promote the reduction of Co oxide. Phahaamohlaka *et al.* [19] also demonstrated this, however, using a different kind of support, hollow carbon spheres (HCSs) for the Co catalyst and Ru as the noble metal promoter. They were able to separate the noble metal promoter, Ru and the Co oxide using the shell of the (HCSs). Ru was loaded inside the HCSs and the Co oxide was loaded outside the HCSs.

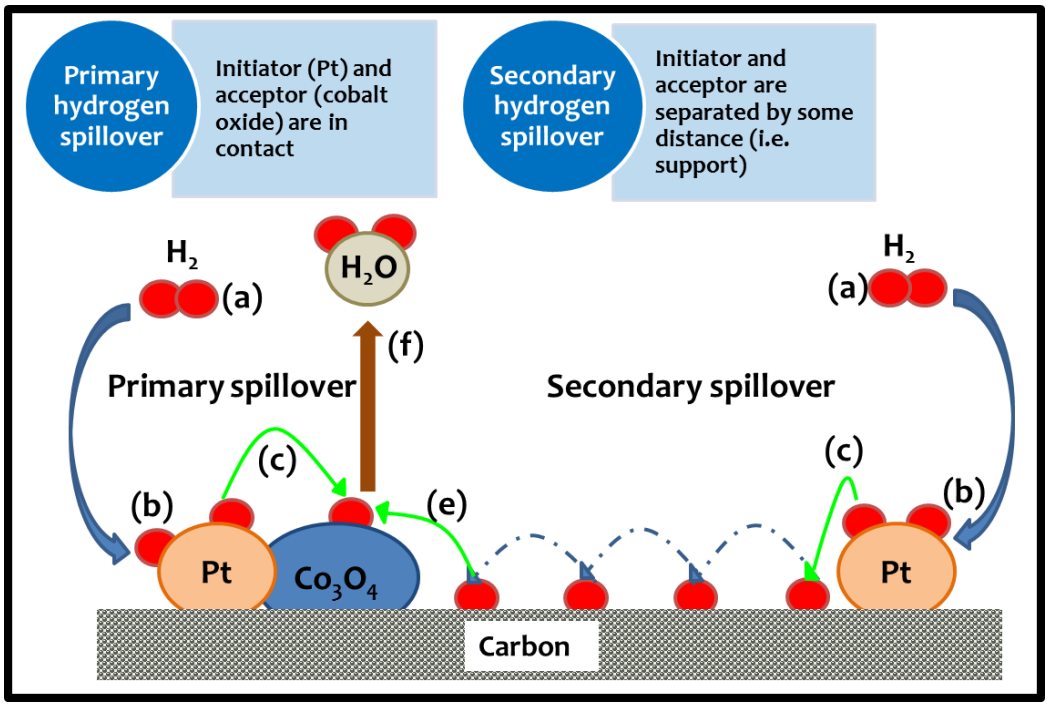


Figure 5.1: Hydrogen spillover pathways: primary (left) and secondary (right), where; (a), molecular hydrogen; (b), dissociative adsorbtion onto the noble metal, Pt; (c), spillover of H atoms; (d), surface migration; (e) spillover; and (f) reduction and water removal. Adapted from [19].

Herein, we report the study of the hydrogen spillover effect between Co and noble metal promoter, Pt, using HCSs as the support. Moreover, in this particular study, in order to have Co and Pt in intimate contact, a Pt – Co bimetallic catalyst was formed inside the HCSs. Separation of the Co was achieved by encapsulating Co inside the HCSs while Pt was loaded outside the HCSs. The encapsulation ability of the HCSs can be exploited while studying the

hydrogen spillover mechanism. The influence of spillover effects on the FT performance of the catalysts was hence studied.

5.2. Experimental

In this section, the materials used and the synthetic procedure followed to obtain Co-encapsulated, CoPt-encapsulated and loading of Pt nanoparticles outside the HCSs will be described in detail.

5.2.1. Sources of chemicals and gases

Styrene (Aldrich), polyvinylpyrollidone (PVP, MW 40 000, Aldrich), cobalt nitrate hexahydrate (Aldrich), hexachloroplatinic acid hexahydrate (Merck), ammonia solution (25%; Fluka), potassium persulfate (Eimer and Amend), hexadecyltrimethylammonium bromide (CTAB; Aldrich), chloroplatinic acid hydrate (Aldrich), hydrazine (50%, Aldrich), ethanol (99%; Merck), ethylene glycol (Aldrich). All the chemicals were used the way they were received. Deionized water was used in all the experiments. For FT studies, the gases used were: hydrogen, nitrogen, argon, syngas (a mixture of 30% carbon monoxide, 10% nitrogen, balanced with hydrogen), six gas mixture (a mixture of CH_4 (2.5%), C_2H_4 (0.2%), C_2H_6 (0.5%), CO (10.0%), CO_2 (5.0%) balanced with argon) all with (>99.9%) purity and obtained from Afrox.

5.2.2. Polystyrene spheres (PSs) – template synthesis

Polystyrene spheres (PSs) were synthesized by adding ethanol (50 ml) and water (200 ml) into a 500 ml round-bottom flask fitted with a condenser and a magnetic stirrer placed inside the flask. A styrene monomer (16 ml) and PVP (0.2 g) were added into the flask and the mixture was allowed to stir for 10 min. To the resulting solution, 0.3 g of potassium persulfate (KPS), dissolved in 20 ml of water, was then added and the solution was stirred for another 10 min. The mixture was then heated in an oil bath to 80 °C and kept at that temperature for 24 h. The resulting product was separated by centrifugation at 18000 rpm for 15 min, washed with ethanol several times, and then dried at 40 °C in an oven overnight. Once dry, it was ground to fine powder.

5.2.3. Loading of Co or CoPt on PSs

PSs (6 g) were dispersed by sonication for 30 min in a water-ethanol solution, (150, and 50 ml, respectively). To this solution, cobalt nitrate hexahydrate (0.89 g) was added, resulting in the formation of a pink milky solution. Reduction of Co nanoparticles was then performed by

slow addition of a solution of hydrazine (10 ml, 2 M) resulting in a blue milky solution of Co/PSs. The solution was then left to stir for 12 h to allow for complete reduction of Co onto the PSs. The resulting Co/PSs was collected by filtration and washed several times with water. The Co/PSs composite was then placed in an oven to dry for 12 h at 40 °C. To obtain the bimetallic CoPt/PSs composite, a similar procedure was followed, but instead of using just the cobalt nitrate hexahydrate (0.89g), the hexachloroplatinic acid hexahydrate (0.05 M, 2 ml) was also added, resulting in the formation of a brown milky solution which eventually gave CoPt/PSs.

5.2.4. Synthesis of Co and CoPt inside HCSs (Co@HCS and CoPt@HCS)

Co/PSs or CoPt/PSs (6 g) were dispersed by sonication in a mixture of ammonia solution (25%; 4 ml), ethanol (300 ml) and water (100 ml) for 30 min. A mixture of resorcinol (2.26 g), formaldehyde solution (37%; 4 ml), CTAB (3 g) and ethanol (100 ml) was sonicated separately, and then added to the Co/PSs or CoPt/PSs. The resulting mixture was then stirred at room temperature for 24 h and then heated to 80 °C in an oil bath for 24 h to polymerize the resorcinol-formaldehyde (RF) polymer on Co/PSs. The resulting composite, Co/PSs@RF or CoPt/PSs@RF, was then filtered and washed several times with water, followed by drying at 60 °C for 12 h. The removal of PSs and carbonization of RF were performed in a one-step procedure using a horizontal tube furnace. The Co/PSs@RF or CoPt/PSs@RF was placed in a quartz boat inside a quartz tube which was then heated inside the furnace under a N_2 flow (50 ml/min) at 350 °C for 1 h and subsequently at 600 °C for 2 h at a heating rate of 5 °C/min. This then resulted in the formation of Co@HCS or CoPt@HCS (Figure 5.2).

5.2.5. Loading of Pt outside Co@HCS (Co@HCS@Pt)

Co@HCS (0.1 g) was dispersed in 40 ml of ethylene glycol by ultrasonication in a 250 ml round-bottom flask. Hexachloroplatinic acid hexahydrate (0.05 M, 1.5 ml) and ascorbic acid (50 mg) were then added to the mixture, and the mixture was sonicated for 15 min. The mixture inside the 250 ml round-bottom flask fitted with a condenser and a magnetic stirrer placed inside the flask was then heated for 4 h at 70 °C in an oil bath. The resulting Co@HCS@Pt sample was collected by vacuum filtration and washed several times with ethanol and water. The resulting composite was then dried overnight in an oven at 120 °C (Figure 5.2).

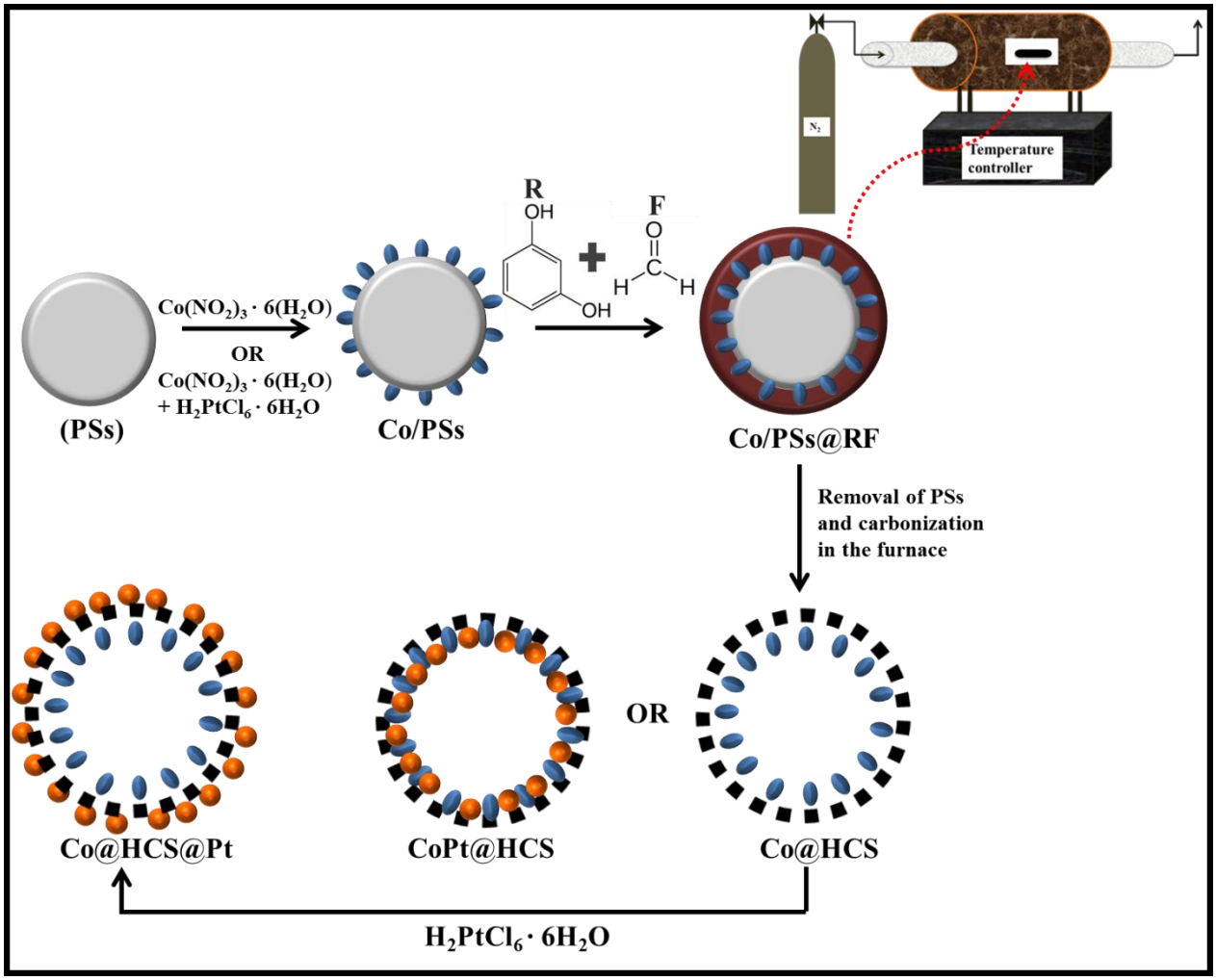


Figure 5.2: Schematic representation of the synthetic procedure for the metal-loaded HCSs.

5.3. Results and discussion

5.3.1. Catalyst characterization

The catalysts were synthesized using the hard templating method [26-28]. The polystyrene spheres (PSs), were used as the sacrificial template [29] and were synthesized according to the method outlined in section 5.2.2. The results of the characterization of PSs were shown in chapter 4 (section 4.2.5.1). Furthermore, to encapsulate the metal nanoparticles inside the hollow carbon spheres (HCSs), the metal precursors were added to the template before adding the carbon precursor [30]. Therefore, the PSs were coated with the Co precursor or a mixture of Co and Pt precursors. The resulting composites were then coated with the carbon source, resorcinol-formaldehyde (RF), which was then carbonized, during which the PSs decomposed, to produce Co@HCS and CoPt@HCS. The catalysts were characterized using TEM. The TEM images (Figure 5.3) revealed the spherical, metal nanoparticles-decorated

core morphology of the Co@HCS (Figure 5.3 a) and CoPt@HCS (Figure 5.3 b). The metal nanoparticles were encapsulated with good dispersion, which involved slow deposition of the metal nanoparticles on the template, a slow flow rate of N_2 gas and a slow heating rate of the furnace during carbonization to avoid agglomeration/sintering of the metal nanoparticles. Pt nanoparticles were loaded onto Co@HCS to obtain Co@HCS@Pt (Figure 5.3 c). Here, the Co and Pt nanoparticles were separated by the carbon shell. The small Pt nanoparticles are encircled in the inset in Figure 5.3 c. The Pt nanoparticles were also loaded on the HCSs with no other metal nanoparticles, which allowed for easier determination of the average Pt particle size. The average particle sizes of the metal nanoparticles (Co, CoPt, and Pt) were determined using the TEM images and the ImageJ software. The metal nanoparticles all had a narrow particle size distribution. The Co nanoparticles were 5.5 ± 1.0 nm (Figure 5.4 a), the CoPt nanoparticles were 5.3 ± 1.0 nm (Figure 5.4 b) and the Pt nanoparticles were 2.3 ± 0.5 nm (Figure 5.4 c).

The monometallic catalyst Co@HCS and the bimetallic CoPt@HCS have similar average particle sizes. Therefore, Pt did not have a significant effect on the size of the Co nanoparticles. It has been reported in the literature that the size of the cobalt nanoparticles is influenced by the conditions used for the deposition of the nanoparticles and the porosity of the support [31]. For instance, Chu *et al.* [22] observed no significant effect of Pt on the size of Co_3O_4 nanoparticles supported on an alumina support and attributed the size of the Co_3O_4 nanoparticles to the pore diameter of the support. Zhang *et al.* [32] also did not observe a significant effect of the Pt promoter on the size of their Co catalyst supported on carbon nanotubes and attributed the size rather to a chemical interaction between the Co oxide nanoparticles and the support resulting from the decomposition of the Co precursor on the support.

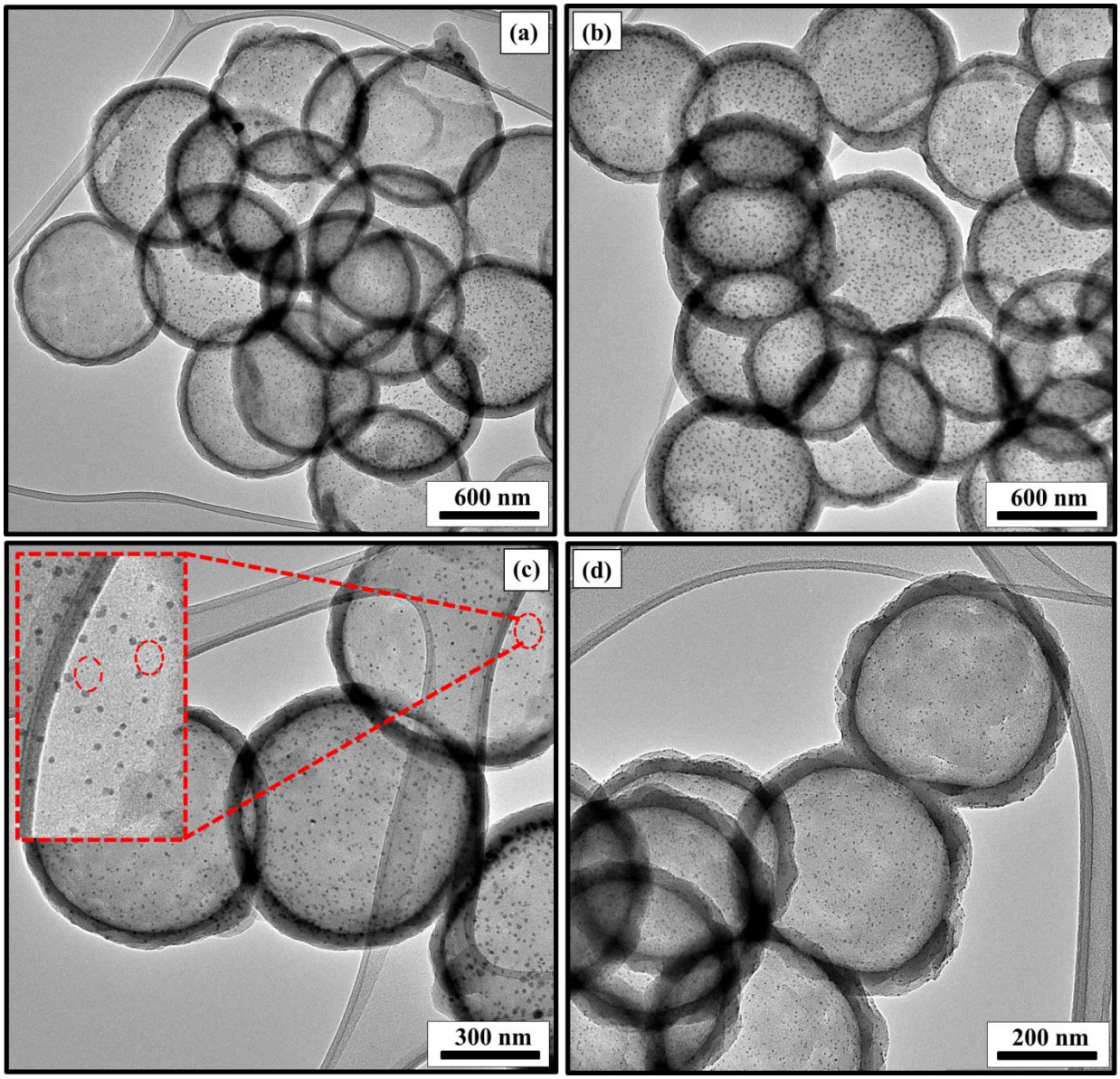


Figure 5.3: TEM images of (a) Co@HCS, (b) CoPt@HCS, (c) Co@HCS@Pt, and (d) Pt/HCS.

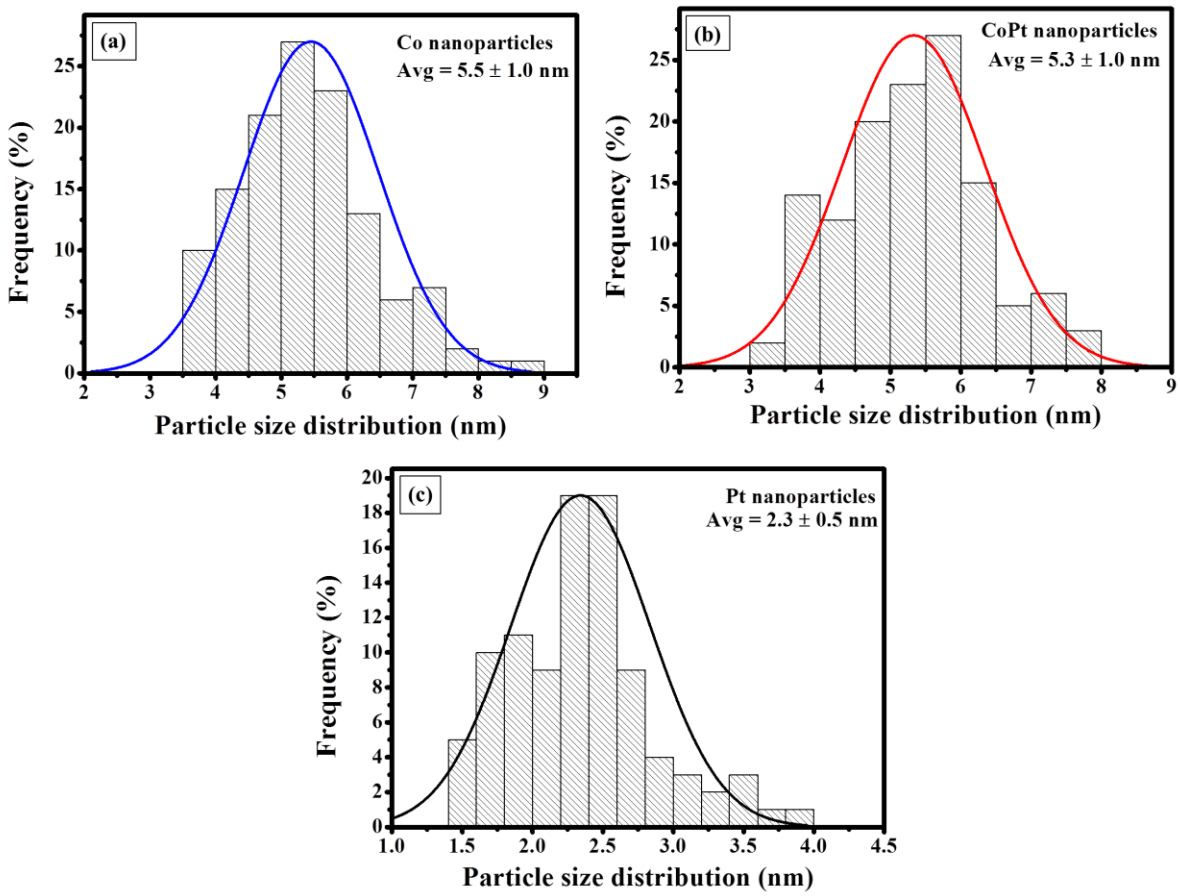


Figure 5.4: Particle size distribution of (a) Co@HCS, (b) CoPt@HCS, and (c) Pt/HCS.

EDX analysis was conducted during SEM analysis to confirm the presence of the Co and Pt nanoparticles in the catalysts. The EDX spectra were obtained from the regions where the HCSs were broken, since the metal nanoparticles were encapsulated inside. Figure 5.5 and Figure 5.6 show the SEM images displaying the hollow regions from which the EDX spectra were obtained of Co@HCS and CoPt@HCS, respectively. Figure 5.5 b confirms the presence of Co in Co@HCS and Figure 5.6 b confirms the presence of both Co and Pt in CoPt@HCS.

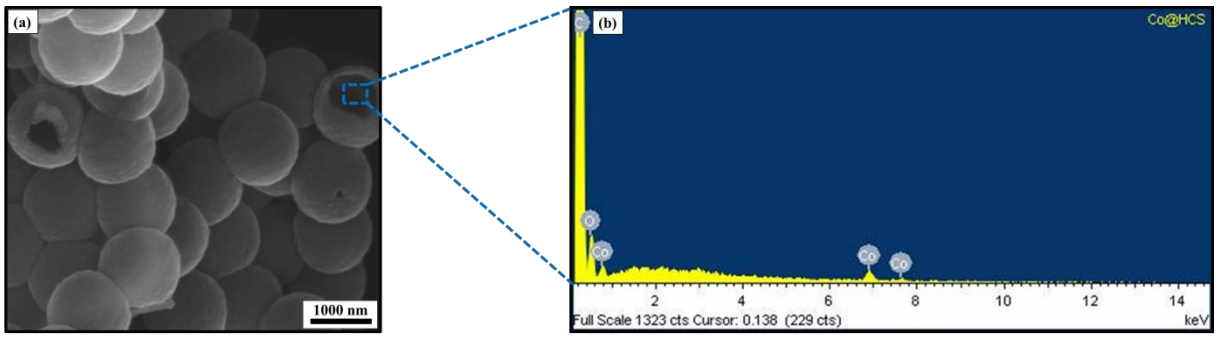


Figure 5.5: (a) SEM image and (b) EDX spectrum of Co@HCS.

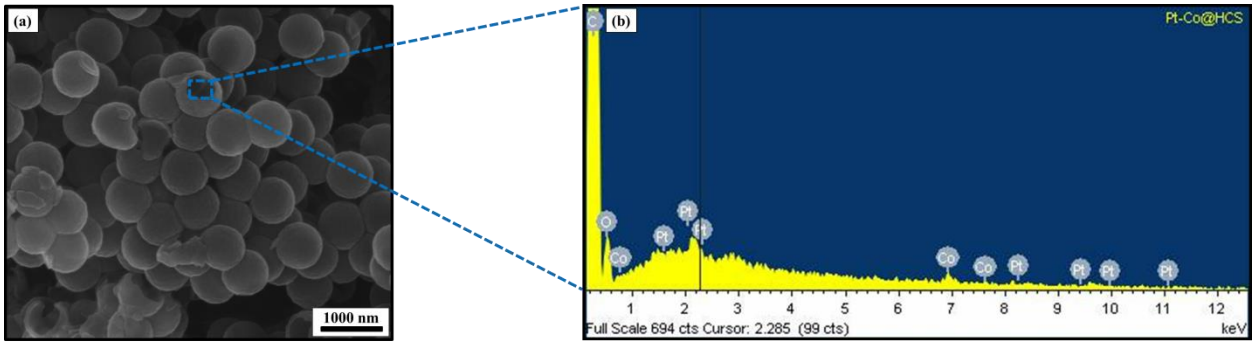


Figure 5.6: (a) SEM image and (b) EDX spectrum of CoPt@HCS.

TGA analysis was carried out on the catalysts to study their thermal stability and the differences in their residual weight percent. The data revealed that all the catalysts had similar TGA profiles. Generally, RF-derived carbon materials have onset decomposition temperatures of 500 °C, typical of non-graphitized carbon [33] which was evident in the HCS support with no metals (Figure 5.7). However, the addition of metals to the support altered the thermal stability and a decrease in the onset decomposition to ca. 350 °C was observed. This can be attributed to the catalytic effect of metal nanoparticles on the decomposition of the carbon support. The residual weight percent of the catalysts was 10 – 12 % and was due to the Co and Pt oxides.

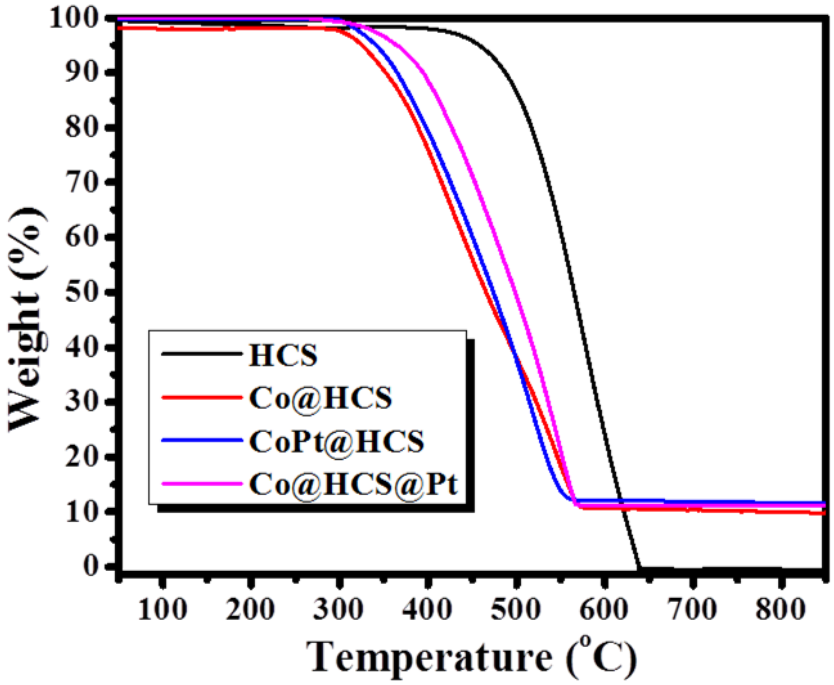


Figure 5.7: TGA profiles for the catalysts.

Table 5.1 shows a summary of the nitrogen physisorption data obtained of the support and the supported catalysts synthesized. All of them had large BET surface areas. There was, generally, an increase in the BET surface area with addition of metal nanoparticles. The pore sizes were greater than 2 nm which shows that they all had mesopores. However, a reduced surface area was observed for CoPt@HCS which can be attributed to some pore blockage by the metal nanoparticles in the pores which can be further confirmed by the high pore volume and pore size.

Table 5.1: A summary of the nitrogen physisorption data.

Sample	BET surface area (m^2/g)	Pore volume (cm^3/g)	Pore size (nm)
HCS	416	0.39	3.8
Co@HCS	486	0.47	4.0
CoPt@HCS	355	0.43	4.9
Co@HCS@Pt	426	0.26	2.4

5.3.2. Reducibility of the catalysts

The reduction of Co oxide to the metallic Co^0 (FT active phase of Co) generally occurs in two steps: (1) Co_3O_4 to CoO and (2) CoO to Co^0 [24, 34]. The TPR profiles (Figure 5.8) show the temperature at which these Co oxide reduction steps occur in the Co@HCS, CoPt@HCS and Co@HCS@Pt catalysts. It is important to note that prior to the TPR analyses, the catalysts were calcined in 5%O_2/He at 210 °C for 2h, to obtain the Co oxide phase. The calcination was performed under these low temperature conditions to ensure that the catalyst support is not oxidized during calcination which would lead to the loss of the support since the HCSs had a low thermal stability due to the catalytic effect of the metal nanoparticles supported on them (Figure 5.6).

The unpromoted, monometallic Co@HCS had three distinct hydrogen consumption peaks. The small peak at 198 °C, according to the literature, can possibly be attributed to the reductive decomposition of residual cobalt nitrate $(CoNO_3)_2$ from the cobalt precursor [32, 35] or the reduction of CoOOH [36]. However, this peak disappeared when Pt was added because of its ability to improve the decomposition of the cobalt precursor [9]. The peaks at 310 and 430 °C were assigned to the reduction of Co_3O_4 to CoO and CoO to Co^0,

respectively. The addition of Pt had an effect on both these reduction steps, causing a shift in the peaks assigned to them, to lower temperatures. This is in agreement with reports in the literature on the effect of Pt on Co reducibility [32]. This was observed for the CoPt@HCS catalyst, wherein the Co_3O_4 to Co reduction peak shifted to 290 °C. This corresponds to both the reduction of Co_3O_4 to CoO and CoO to Co^0. This downward shift in the Co reduction peaks can be attributed to a primary hydrogen spillover effect. Dissociatively adsorbed H_2 on Pt is converted to highly active H atoms that then spill over to the neighbouring Co_3O_4 and causes its reduction [11]. A small reduction peak was also observed at 402 °C. It is believed that this peak could be due to some Co not in contact with Pt. Nevertheless, a high hydrogen uptake is usually observed for samples in which Co oxide is in intimate contact with a promoter.

For Co@HCS@Pt, where the Co oxide and Pt are separated by the carbon shell (~30 nm in thickness), a reduction peak is observed at 280 °C wherein hydrogen uptake was much less. The downward shift to lower temperatures of the peak indicates that hydrogen spillover took place and that a secondary hydrogen spillover effect was in operation due to the separation between Co oxide and Pt, with Pt being outside and Co oxide being inside the HCSs. The apparent decrease in the amount of hydrogen uptake suggests the occurrence of diffusion limitations of the H atoms when the Co oxide is separated from Pt [37]. The secondary hydrogen spillover effect was also observed, from a literature survey, in a hybrid Pt-Co [25] and hybrid Rh-Co [21] where the promoters, Pt and Rh were separated from Co oxide by some distance using alumina supports. The secondary hydrogen spillover effect was also observed for the Ru@MHCS@Co sample, where Ru and Co were separated by the carbon shell, with Ru being inside and Co oxide outside [19].

The peaks present in all the catalysts at a temperature greater than 600 °C are due to the gasification of the carbon support to CH_4 [18]. Peaks above 600 °C for catalysts supported on carbon materials are usually assigned to the gasification of the carbon support and were observed by by Bahome *et al.* [38] when using CNTs and by Dlamini *et al.* when using solid carbon spheres [18].

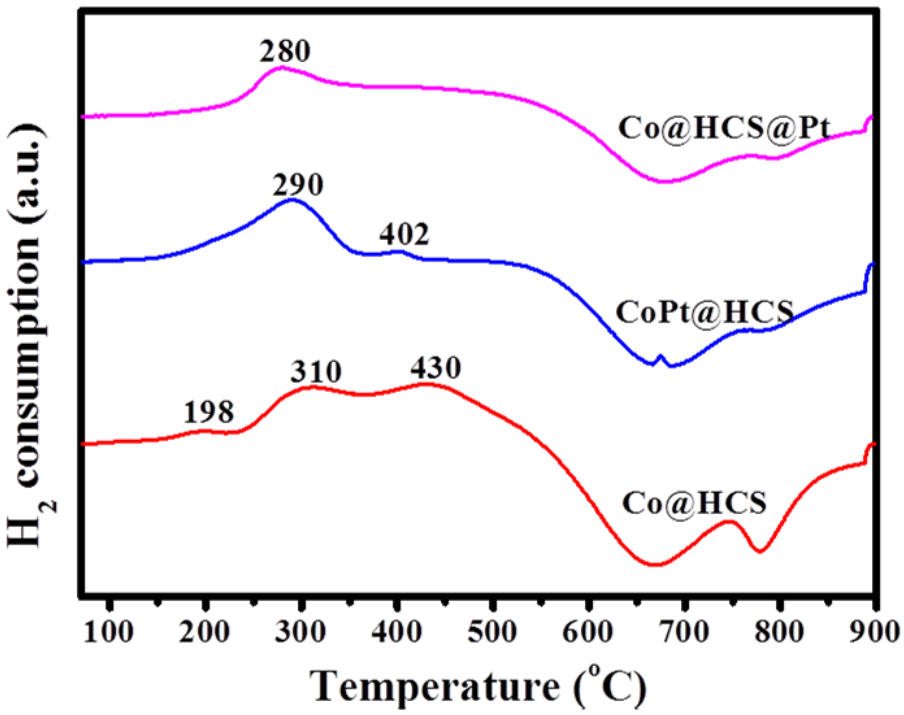


Figure 5.8: TPR profiles of the catalysts.

An in situ XRD analysis was performed on the samples to monitor their reduction behaviour. The data was collected in the temperature region 30 – 350 °C every 20 °C (not shown here since a Cu Kα X-ray source was used for lack of the Co source, which produced data with high fluorescence). When the temperature of 350 °C was reached, an additional 2 h reduction at that temperature was performed. This resulted in the diffractograms that were used qualitatively (Figure 5.9) to study the reaction.

The Co_3O_4 spinel phase was not present in any of the samples. It has been reported in the literature that it undergoes reduction very easily to CoO [25]. The CoO phase was present in all three of the samples which shows that they did not undergo 100 % reduction to metallic Co. Metallic Co exists in two phases namely Co (fcc) and Co (hcp) [39]. Co (fcc) was observed in all three catalysts. The Co (fcc) phase was the dominant metallic Co phase in the unpromoted Co@HCS catalyst and the Co@HCS@Pt catalyst in which Co and Pt were not in contact. Co (hcp) was the dominant metallic Co phase in the CoPt@HCS catalyst in which Co and Pt were in contact. The Co (hcp) phase has been reported in the literature to be the more FT catalytically active phase of metallic Co, and due to the hydrogen spillover effect, noble metal promoters such as Pt can facilitate the formation of Co (hcp). Low reduction

temperatures usually lead to the formation of Co (hcp) while high reduction temperatures lead to Co (fcc) formation [40]. The Co (hcp) to Co (fcc) ratios followed the pattern: CoPt@HCS (1.2) > Co@HCS@Pt (0.68) > Co@HCS (0.53). This data suggests that both the primary and secondary hydrogen spillover effects can be invoked in describing the role Pt plays in the enhancement of Co reducibility and formation of the highly active Co (hcp) phase for the FT process. The primary hydrogen spillover effect seems to be more favoured than the secondary hydrogen spillover effect as there was a clear distinction between the data obtained for the CoPt@HCS and Co@HCS samples, than for the Co@HCS@Pt and Co@HCS samples. This again suggests that when Co oxide and Pt are separated there may be diffusion limited migration of the H atoms [37] and that their intimacy allows better migration of the H atoms.

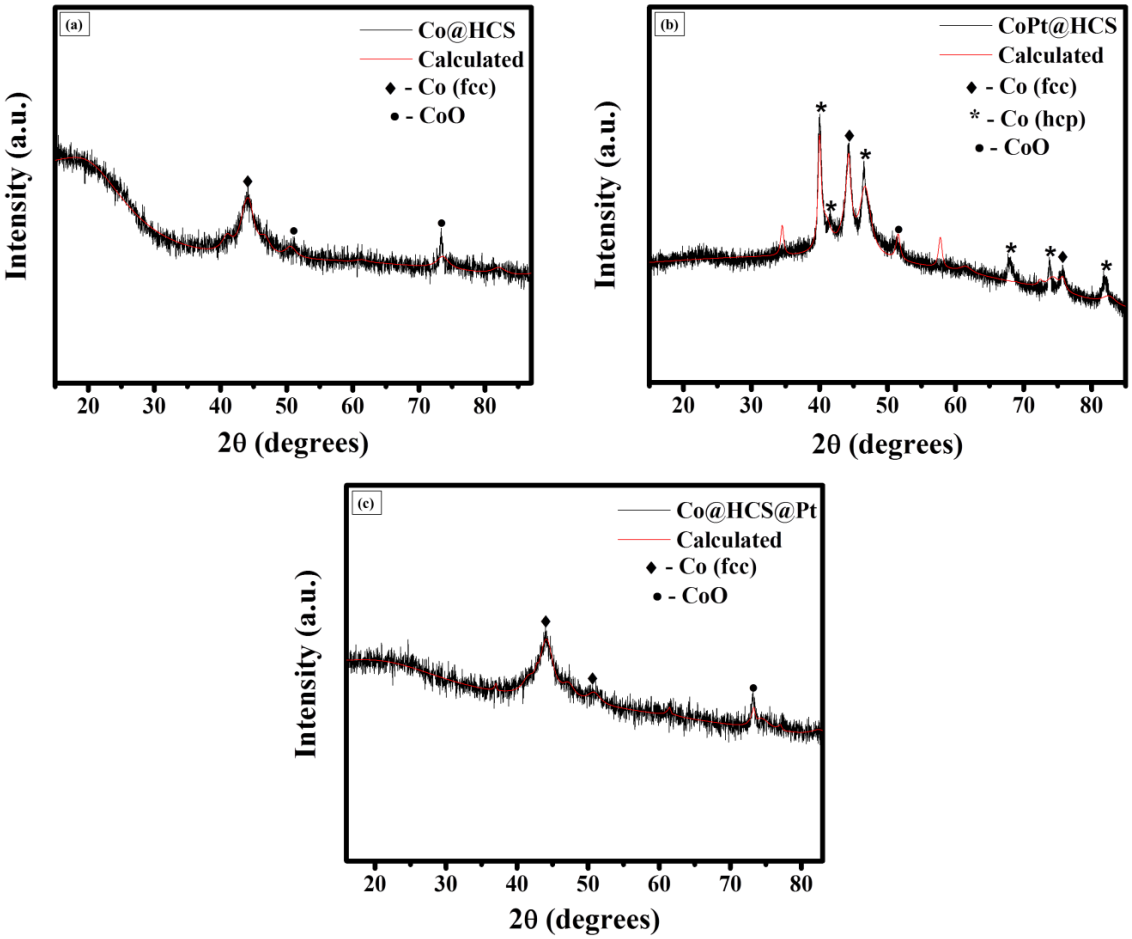


Figure 5.9: Diffractograms of (a) Co@HCS, (b) CoPt@HCS , and (c) Co@HCS@Pt.

5.3.3. Preliminary Fischer-Tropsch (FT) evaluation of the catalysts

The preliminary evaluation of the FT catalytic performance of the catalysts was conducted using a fixed bed reactor under similar reaction conditions (220 °C, 10 bar, $H_2/CO = 2$). The catalysts were first reduced *in-situ* at 350 °C for 18 h under H_2, followed by the FT reaction using syngas at 220 °C [6, 19, 38]. The CoPt@HCS catalyst exhibited the highest degree of CO conversion (Figure 5.10 and Table 5.2, below). Only a small difference in the degree of CO conversion between the Co@HCS@Pt and the unpromoted Co@HCS catalyst was noted. The higher CO conversion observed with CoPt@HCS can be attributed to the direct (primary) hydrogen spillover between the Pt and Co_3O_4 as a result of their intimacy. This resulted in the easier reduction of the Co oxide and subsequent generation of the active Co (hcp) [39]. In essence, the degree of reduction of Co oxide was affected by the hydrogen spillover which had an impact on the available Co active sites. This influenced the FT activity.

The secondary hydrogen spillover effect in Co@HCS@Pt, wherein the Co and Pt were separated by the carbon shell (~30 nm) was not as effective in inducing a high activity in the FT reaction. This could be related to the inability to reduce the Co oxide or to the poor formation of metallic Co (hcp). This may be attributed to the distance the spiltover hydrogen had to travel and some diffusion limitations due to the blockage of some of the pores of the support, resulting in limited diffusion migration of the spiltover H atoms [19, 41].

It is also noteworthy to mention that in addition to the low temperature formation of the Co active phase, as a result of the hydrogen spillover effect, promoters have also been reported to have a ‘cleansing effect’ on the Co surface by removing unreactive species such as carbon from the surface which may enhance the CO conversion [25, 42, 43]. This would be more pronounced when Co and Pt are in contact, in the case of the primary hydrogen spillover process.

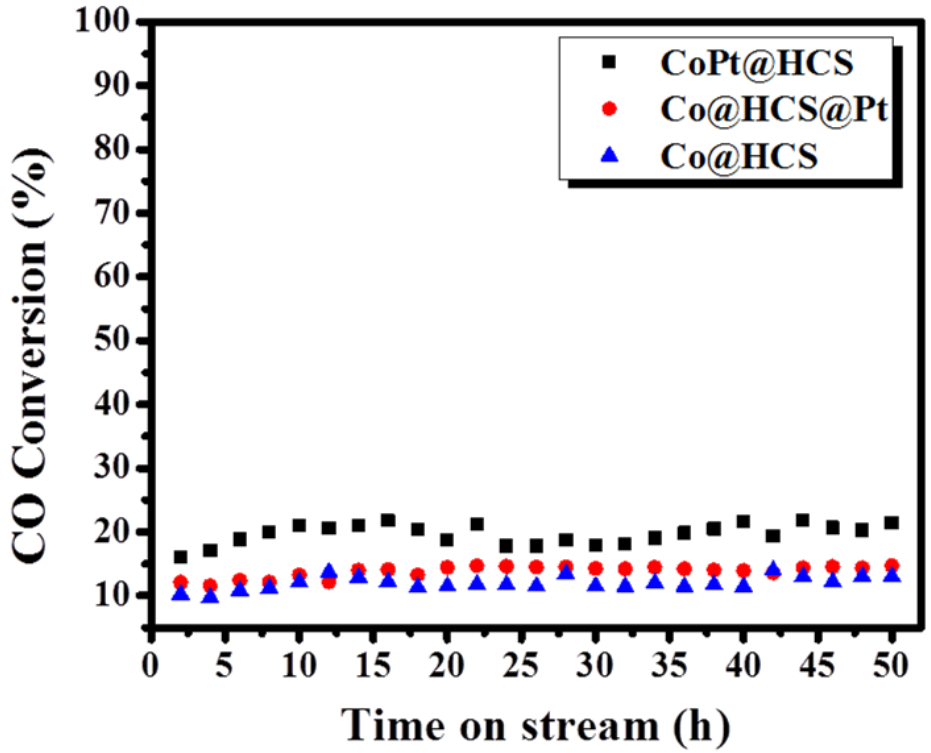


Figure 5.10: CO conversion of the catalysts.

Table 5.2: Summary of the FT performance of the catalysts.

Sample	CO Conversion (%)	Hydrocarbon selectivity (%)		
		C_1	C_2-C_4	C_{5+}
CoPt@HCS	19.1 ± 1.5	32.0	9.7	58.3
Co@HCS@Pt	12.7 ± 0.9	23.4	9.2	67.4
Co@HCS	11.5 ± 1.0	18.3	12.1	69.6

The hydrogen spillover effect was also observed to have an effect on the hydrocarbon selectivity of the catalysts (Table 5.2). The activities were reasonably similar and thus selectivity comparisons were made. The methane selectivity increased with increased contact between Pt and Co: Co@HCS (18.3%) < Co@HCS@Pt (23.4%) < CoPt@HCS (32.0%). The high CH_4 selectivity can be attributed to the high hydrogenation activity of the Pt promoter. This high hydrogenation activity is generally expected in catalysts that have loadings of the promoter being greater than 0.1 % [44]. The promoted catalysts had a Pt loading of 0.5% and the added intimacy in the contact between Co and Pt in the CoPt@HCS catalyst can be linked

to the undesired high methane selectivity observed. Although Co@HCS had lower methane selectivity than that of the Pt containing catalysts, its methane selectivity was still quite high. This can be attributed to the microporosity in the support which limited the diffusion of the high molecular weight hydrocarbons. This high methane selectivity led to lower C_{5+} selectivities of the catalysts.

It appears that intimacy between Pt and Co was important in the hydrogen spillover effect under FT conditions. The diminished Pt promoter effect, due to secondary hydrogen spillover, under Fischer-Tropsch conditions is as a result of the distance between the Pt and Co. This was also observed by Nabaho *et al.* [25] for their catalyst where the Pt and Co were separated by some distance using alumina supports. They attributed the effect to the CO poisoning of the surface of Pt occurring to the detriment of the hydrogenation reaction which is a well-known phenomenon in olefin hydrogenation reactions [45] and PEM fuel cells [46]. During the FT reaction, the CO from the syngas feed may adsorb onto the Pt surface to the detriment of H_2 adsorption and subsequent hydrogen spillover [25].

5.4. Conclusion

In summary, Co catalysts (unpromoted and promoted with Pt) supported on HCSs were successfully synthesized. The Co nanoparticles were encapsulated inside the HCSs to produce the Co@HCS catalyst. A bimetallic catalyst, CoPt@HCS, was produced from the encapsulation of both Co and Pt nanoparticles inside the HCSs. In achievement of our objective to separate the Co and Pt nanoparticles by the carbon shell, Co nanoparticles were encapsulated inside the HCSs while Pt was loaded outside the HCSs to produce the Co@HCS@Pt catalyst. The TEM images showed that the nanoparticles were loaded with good dispersion and the TGA data showed the decomposition of the carbon support which was lower in the presence of metal nanoparticles due to their catalytic effect. The residual weight percent was due to the metals loaded and ranged from 10 – 12 %. EDX spectra also confirmed the presence of the Co and Pt nanoparticles in the catalysts.

It can be concluded the catalysts were successfully utilized in investigating the Pt promoter effect on Co oxide *via* the primary and secondary hydrogen spillover effect. The TPR, *in-situ* XRD and FT performance confirmed that: (i) the presence of Pt, especially when in intimate contact with Co does indeed enhance its reducibility causing Co oxide to get reduced to its metallic active phase Co^0 at lower temperatures, for both Co_3O_4 to CoO and CoO to Co as shown by the TPR profiles, (ii) a high Co (hcp) to Co (fcc) ratio from the reduction of the Co

oxide when Pt and Co were in intimate contact was achieved, and as a result (iii) the highest degree of CO conversion was observed for CoPt@HCS in the FT data and the hydrocarbon selectivity also showed the contribution of the primary hydrogen spillover effect.

The secondary hydrogen spillover effect was also observed although it did not have an effect as significant as that of the primary hydrogen spillover. Its diminished effect, observed in the performance of the Co@HCS@Pt catalyst, where Co and Pt were separated by the carbon shell (~30 nm) can be attributed to the distance between Pt and Co and the possible hydrogen atom surface diffusion limitations. This was observed in the TPR data where a lesser hydrogen uptake was noted despite the downward shift in the reduction peak and in the FT data which was not significantly better than that obtained for the unpromoted Co@HCS catalyst.

5.5. References

[1] T. Fu, Z. Li, Review of recent development in Co-based catalysts supported on carbon materials for Fischer–Tropsch synthesis, Chemical Engineering Science 135 (2015) 3-20.

[2] Q. Zhang, J. Kang, Y. Wang, Development of novel catalysts for Fischer–Tropsch synthesis: tuning the product selectivity, ChemCatChem 2 (2010) 1030-1058.

[3] T. Fu, Y. Jiang, J. Lv, Z. Li, Effect of carbon support on Fischer–Tropsch synthesis activity and product distribution over Co-based catalysts, Fuel processing technology 110 (2013) 141-149.

[4] H. Li, J. Li, H. Ni, D. Song, Studies on cobalt catalyst supported on silica with different pore size for Fischer–Tropsch synthesis, Catalysis letters 110 (2006) 71-76.

[5] J.H. Yang, H.-J. Kim, D.H. Chun, H.-T. Lee, J.-C. Hong, H. Jung, J.-I. Yang, Mass transfer limitations on fixed-bed reactor for Fischer–Tropsch synthesis, Fuel Processing Technology 91 (2010) 285-289.

[6] G.L. Bezemer, J.H. Bitter, H.P. Kuipers, H. Oosterbeek, J.E. Holewijn, X. Xu, F. Kapteijn, A.J. van Dillen, K.P. de Jong, Cobalt particle size effects in the Fischer− Tropsch reaction studied with carbon nanofiber supported catalysts, Journal of the American Chemical Society 128 (2006) 3956-3964.

[7] I. Chorkendorff, J.W. Niemantsverdriet, Concepts of modern catalysis and kinetics, John Wiley & Sons, 2017.

[8] F. Morales, B.M. Weckhuysen, Promotion effects in Co-based Fischer-Tropsch catalysis, Catalysis 19 (2006).

[9] A.Y. Khodakov, W. Chu, P. Fongarland, Advances in the development of novel cobalt Fischer− Tropsch catalysts for synthesis of long-chain hydrocarbons and clean fuels, Chemical reviews 107 (2007) 1692-1744.

[10] Ø. Borg, S. Eri, E.A. Blekkan, S. Storsæter, H. Wigum, E. Rytter, A. Holmen, Fischer–Tropsch synthesis over γ-alumina-supported cobalt catalysts: effect of support variables, Journal of Catalysis 248 (2007) 89-100.

[11] G. Jacobs, T.K. Das, Y. Zhang, J. Li, G. Racoillet, B.H. Davis, Fischer–Tropsch synthesis: support, loading, and promoter effects on the reducibility of cobalt catalysts, Applied Catalysis A: General 233 (2002) 263-281.

[12] A. Saib, M. Claeys, E. Van Steen, Silica supported cobalt Fischer–Tropsch catalysts: effect of pore diameter of support, Catalysis today 71 (2002) 395-402.

[13] M. Trépanier, A. Tavasoli, A.K. Dalai, N. Abatzoglou, Co, Ru and K loadings effects on the activity and selectivity of carbon nanotubes supported cobalt catalyst in Fischer–Tropsch synthesis, Applied Catalysis A: General 353 (2009) 193-202.

[14] A. Tavasoli, R.M.M. Abbaslou, M. Trepanier, A.K. Dalai, Fischer–Tropsch synthesis over cobalt catalyst supported on carbon nanotubes in a slurry reactor, Applied Catalysis A: General 345 (2008) 134-142.

[15] J. Jaramillo, P.M. Álvarez, V. Gómez-Serrano, Oxidation of activated carbon by dry and wet methods: Surface chemistry and textural modifications, Fuel Processing Technology 91 (2010) 1768-1775.

[16] W.-P. Ma, Y.-J. Ding, L.-W. Lin, Fischer− Tropsch Synthesis over Activated-Carbon-Supported Cobalt Catalysts: Effect of Co Loading and Promoters on Catalyst Performance, Industrial & engineering chemistry research 43 (2004) 2391-2398.

[17] A. Tavasoli, K. Sadagiani, F. Khorashe, A. Seifkordi, A. Rohani, A. Nakhaeipour, Cobalt supported on carbon nanotubes—a promising novel Fischer–Tropsch synthesis catalyst, Fuel Processing Technology 89 (2008) 491-498.

[18] M.W. Dlamini, D.O. Kumi, T.N. Phaahlamohlaka, A.S. Lyadov, D.G. Billing, L.L. Jewell, N.J. Coville, Carbon spheres prepared by hydrothermal synthesis—a support for bimetallic iron cobalt Fischer–Tropsch catalysts, ChemCatChem 7 (2015) 3000-3011.

[19] T.N. Phaahlamohlaka, D.O. Kumi, M.W. Dlamini, R. Forbes, L.L. Jewell, D.G. Billing, N.J. Coville, Effects of Co and Ru Intimacy in Fischer–Tropsch Catalysts

Using Hollow Carbon Sphere Supports: Assessment of the Hydrogen Spillover Processes, ACS Catalysis 7 (2017) 1568-1578.

[20] S. Vada, A. Hoff, E. Ådnanes, D. Schanke, A. Holmen, Fischer-Tropsch synthesis on supported cobalt catalysts promoted by platinum and rhenium, Topics in Catalysis 2 (1995) 155-162.

[21] A. Hilmen, D. Schanke, A. Holmen, TPR study of the mechanism of rhenium promotion of alumina-supported cobalt Fischer-Tropsch catalysts, Catalysis letters 38 (1996) 143-147.

[22] W. Chu, P.A. Chernavskii, L. Gengembre, G.A. Pankina, P. Fongarland, A.Y. Khodakov, Cobalt species in promoted cobalt alumina-supported Fischer–Tropsch catalysts, Journal of Catalysis 252 (2007) 215-230.

[23] D. Schanke, S. Vada, E. Blekkan, A. Hilmen, A. Hoff, A. Holmen, Study of Pt-promoted cobalt CO hydrogenation catalysts, Journal of Catalysis 156 (1995) 85-95.

[24] K.M. Cook, S. Poudyal, J.T. Miller, C.H. Bartholomew, W.C. Hecker, Reducibility of alumina-supported cobalt Fischer–Tropsch catalysts: Effects of noble metal type, distribution, retention, chemical state, bonding, and influence on cobalt crystallite size, Applied Catalysis A: General 449 (2012) 69-80.

[25] D. Nabaho, J.H. Niemantsverdriet, M. Claeys, E. van Steen, Hydrogen spillover in the Fischer–Tropsch synthesis: an analysis of platinum as a promoter for cobalt–alumina catalysts, Catalysis Today 261 (2016) 17-27.

[26] F. Su, X. Zhao, Y. Wang, L. Wang, J.Y. Lee, Hollow carbon spheres with a controllable shell structure, Journal of materials chemistry 16 (2006) 4413-4419.

[27] R. Liu, S.M. Mahurin, C. Li, R.R. Unocic, J.C. Idrobo, H. Gao, S.J. Pennycook, S. Dai, Dopamine as a carbon source: the controlled synthesis of hollow carbon spheres and yolk-structured carbon nanocomposites, Angewandte Chemie International Edition 50 (2011) 6799-6802.

[28] S.B. Yoon, K. Sohn, J.Y. Kim, C.H. Shin, J.S. Yu, T. Hyeon, Fabrication of carbon capsules with hollow macroporous core/mesoporous shell structures, Advanced Materials 14 (2002) 19-21.

[29] R.J. White, K. Tauer, M. Antonietti, M.-M. Titirici, Functional hollow carbon nanospheres by latex templating, Journal of the American Chemical Society 132 (2010) 17360-17363.

[30] T.N. Phaahlamohlaka, D.O. Kumi, M.W. Dlamini, L.L. Jewell, N.J. Coville, Ruthenium nanoparticles encapsulated inside porous hollow carbon spheres: A novel catalyst for Fischer–Tropsch synthesis, Catalysis Today 275 (2016) 76-83.

[31] J.-S. Girardon, A.S. Lermontov, L. Gengembre, P.A. Chernavskii, A. Griboval-Constant, A.Y. Khodakov, Effect of cobalt precursor and pretreatment conditions on the structure and catalytic performance of cobalt silica-supported Fischer–Tropsch catalysts, Journal of Catalysis 230 (2005) 339-352.

[32] H. Zhang, W. Chu, C. Zou, Z. Huang, Z. Ye, L. Zhu, Promotion effects of platinum and ruthenium on carbon nanotube supported cobalt catalysts for Fischer–Tropsch synthesis, Catalysis letters 141 (2011) 438-444.

[33] W. Kukułka, K. Wenelska, M. Baca, X. Chen, E. Mijowska, From Hollow to Solid Carbon Spheres: Time-Dependent Facile Synthesis, Nanomaterials 8 (2018) 861.

[34] G. Jacobs, Y. Ji, B.H. Davis, D. Cronauer, A.J. Kropf, C.L. Marshall, Fischer–Tropsch synthesis: temperature programmed EXAFS/XANES investigation of the influence of support type, cobalt loading, and noble metal promoter addition to the reduction behavior of cobalt oxide particles, Applied Catalysis A: General 333 (2007) 177-191.

[35] E. van Steen, G.S. Sewell, R.A. Makhothe, C. Micklethwaite, H. Manstein, M. de Lange, C.T. O'Connor, TPR study on the preparation of impregnated Co/SiO2catalysts, Journal of Catalysis 162 (1996) 220-229.

[36] J. Van de Loosdrecht, S. Barradas, E. Caricato, N. Ngwenya, P. Nkwanyana, M. Rawat, B. Sigwebela, P. Van Berge, J. Visagie, Calcination of Co-based Fischer–Tropsch synthesis catalysts, Topics in catalysis 26 (2003) 121-127.

[37] S.K. Beaumont, S. Alayoglu, C. Specht, N. Kruse, G.A. Somorjai, A nanoscale demonstration of hydrogen atom spillover and surface diffusion across silica using the kinetics of CO2 methanation catalyzed on spatially separate Pt and Co nanoparticles, Nano letters 14 (2014) 4792-4796.

[38] G.L. Bezemer, P. Radstake, U. Falke, H. Oosterbeek, H. Kuipers, A. Van Dillen, K. De Jong, Investigation of promoter effects of manganese oxide on carbon nanofiber-supported cobalt catalysts for Fischer–Tropsch synthesis, Journal of Catalysis 237 (2006) 152-161.

[39] S. Lyu, L. Wang, J. Zhang, C. Liu, J. Sun, B. Peng, Y. Wang, K.G. Rappe, Y. Zhang, J. Li, Role of Active Phase in Fischer–Tropsch Synthesis: Experimental Evidence of

CO Activation over Single-Phase Cobalt Catalysts, ACS Catalysis 8 (2018) 7787-7798.

[40] O. Ducreux, B. Rebours, J. Lynch, M. Roy-Auberger, D. Bazin, Microstructure of supported cobalt Fischer-Tropsch catalysts, Oil & Gas Science and Technology-Revue de l'IFP 64 (2009) 49-62.

[41] I. Nongwe, G. Bepete, A. Shaikjee, V. Ravat, B. Terfassa, R. Meijboom, N.J. Coville, Synthesis of gold encapsulated in spherical carbon capsules with a mesoporous shell structure. A robust catalyst in a nanoreactor, Catalysis Communications 53 (2014) 77-82.

[42] S.K. Beaumont, S. Alayoglu, C. Specht, W.D. Michalak, V.V. Pushkarev, J. Guo, N. Kruse, G.A. Somorjai, Combining in situ NEXAFS spectroscopy and CO2 methanation kinetics to study Pt and Co nanoparticle catalysts reveals key insights into the role of platinum in promoted cobalt catalysis, Journal of the American Chemical Society 136 (2014) 9898-9901.

[43] E. Iglesia, S.L. Soled, R.A. Fiato, G.H. Via, Bimetallic synergy in cobalt ruthenium Fischer-Tropsch synthesis catalysts, Journal of Catalysis 143 (1993) 345-368.

[44] F. Diehl, A.Y. Khodakov, Promotion of cobalt Fischer-Tropsch catalysts with noble metals: a review, Oil & Gas Science and Technology-Revue de l'IFP 64 (2009) 11-24.

[45] K.S. Hwang, M. Yang, J. Zhu, J. Grunes, G.A. Somorjai, The molecular mechanism of the poisoning of platinum and rhodium catalyzed ethylene hydrogenation by carbon monoxide, Journal of Molecular Catalysis A: Chemical 204 (2003) 499-507.

[46] J. Baschuk, X. Li, Carbon monoxide poisoning of proton exchange membrane fuel cells, International Journal of Energy Research 25 (2001) 695-713.

Chapter 6: General conclusions and recommendations

6.1. Conclusions

The aim of the study was to synthesize hollow carbon spheres (HCSs) using polystyrene spheres (PSs) as the template and resorcinol-formaldehyde (RF) as the carbon source and to use the HCSs as a model platinum-promoted cobalt catalyst support for Fischer-Trospch (FT) processes. The hydrogen spillover effect of these catalysts were also investigated. Characterization techniques such as TEM, SEM, BET, Raman, TGA, PXRD, and TPR, were used to draw the following conclusions:

Uniform size and monodisperse PSs were synthesized and used as a template for the deposition of RF. The removal of the PSs by thermal decomposition and the carbonization of RF occurred simultaneously, to form hollow carbon spheres that were also uniform in size and monodispersed.

The effect of the synthesis parameters used for RF deposition on the resulting HCSs was investigated. It was discovered that the shell thickness of the HCSs was tunable by varying the amount of the RF used and by changing the alcoholic solvent used, i.e. using ethanol, isopropanol or butanol. As a result, HCSs with shell thicknesses varying from 30 to 80 nm were obtained. The porosity of the HCSs was observed to be affected by changing the alcoholic solvent.

The encapsulation ability of the HCSs was exploited by loading Co nanoparticles inside the HCSs. To have the Co nanoparticles encapsulated, their precursor was first deposited onto the PSs, followed by RF coating of the Co/PSs composite and finally the removal of the template and carbonization to obtain Co@HCS. No loss of Co nanoparticles occurred as would be the case if silica was used as the template. The use of a 10 °C/min heating rate during the template-removal and carbonization step resulted in bigger Co nanoparticles with a poor dispersion while a slower heating rate of 5 °C/min resulted in smaller, well dispersed Co nanoparticles.

The increase in the RF amount, to increase the HCSs' shell thickness, caused the encapsulated Co nanoparticles to grow in size, with the biggest size and presence of some

carbon nanotubes observed when the HCSs' shell thickness was 80 nm. Changing the alcoholic solvent had no effect on the size of the encapsulated Co nanoparticles.

To investigate the ability of Pt to enhance Co reducibility *via* the hydrogen spillover, Pt and Co were (i) encapsulated inside the HCSs to form the bimetallic CoPt@HCS catalyst and (ii) the Co and Pt were separated by the carbon shell (~30 nm) to form Co@HCS@Pt. A primary hydrogen spillover effect and a secondary spilliover effect were invoked to explain the enhancement in Co reducibility observed with the CoPt@HCS and Co@HCS@Pt catalysts, respectively, in comparison to Co@HCS.

Comparison of the two hydrogen spillover processes revealed that the primary hydrogen spillover process was more effective in enhancing the reduction of Co oxide to metallic Co particularly the highly catalytically active Co (hcp) phase in FT, than the secondary hydrogen process. It was observed that the intimacy between Co and Pt plays an important role in the hydrogen spillover process. Separation of the two may lead to hydrogen atom surface diffusion limitations.

The effect of hydrogen spillover on the FT performance of the catalysts was observed from the preliminary studies undertaken. The highest CO conversion was observed with CoPt@HCS, followed by Co@HCS@Pt and then Co@HCS. This can be due to a greater extent of Co oxide reduction with an increase in Co and Pt contact resulting in more of the catalytically active Co (hcp) metallic phase of Co present during the FT reaction. The CO present in the FT reaction may have played a role in the lower CO conversion observed in the Co@HCS@Pt catalyst compared to the CoPt@HCS catalyst, by decreasing the available sites for the dissociative adsorption of H_2 on the Pt and its subsequent spillover to Co. In addition, an increase in contact between Co and Pt resulted in higher methane selectivity due to the high hydrogenation activity of Pt.

6.2. Recommendations

Further studies could be carried out to show evidence of the hydrogen spillover effect such as *in-situ* magnetic measurements using pure hydrogen to monitor the temperature at which the appearance of metallic cobalt occurs and XANES/EXFAS experiments to monitor the extent of Co oxide reduction. The effect of the hydrogen spillover on FT can then be further investigated.

Loading of Co nanoparticles outside the HCSs could be carried out and optimized such that similar dispersions and particle sizes to those achieved when the Co nanoparticles are encapsulated inside the HCSs, are achieved.

A study should be undertaken to compare the hydrogen spillover effect and the FT performance observed with the Pt-promoted Co-encapsulated (CoPt@HCS) catalysts with those where the Co and Pt are loaded outside the HCSs (CoPt/HCS).

Heteroatoms such as N_2 or O_2 can be introduced into the HCSs as dopants to study the hydrogen spillover effect through these supports. These groups (N, O) will increase the defect concentration on the carbon surface and this will impact on the hydrogen spillover effect. In addition, other promoters can be used such as Ru, Rh or Pd and the spillover effects compared to Pt.

A study can be undertaken on the secondary hydrogen spillover effect in particular, where Co and the promoter are separated, to determine the distance at which the extent of Co reducibility starts to diminish using the HCSs' shell thickness as a means to control the distance of separation. The pore size of the HCSs may also be varied to observe the role of diffusion on the reaction.